Max-Planck-Institut für Kolloid- und Grenzflächenforschung

Abteilung für Biomaterialien

Formation and Alteration of Magnetite Nanoparticles

Dissertation
zur Erlangung des akademischen Grades
"doctor rerum naturalium"
(Dr. rer. nat.)
in der Wissenschaftsdisziplin "Materialwissenschaft"

eingereicht an der
Mathematisch-Naturwissenschaftlichen Fakultät
der Universität Potsdam

von

Marc Widdrat

Potsdam, den 30.09.2014

Acknowledgements

I am very grateful for all the help and support that I received during the last three years at the Max-Planck-Institute of Colloids and Interfaces at the Department of Biomaterials. I would like to thank Dr. Damien Faivre for giving me the chance to work in his group and to work on magnetite nanoparticles during my dissertation. I would like to thank Prof. Peter Fratzl, the head of the department, for many helpful and instructive discussions.

I would like to thank Prof. Peter Strauch for his supervision and the nice atmosphere during all the meetings about this thesis.

Special thanks to the electron microscopy team, Dr. Jürgen Hartmann for teaching me how to use the transmission electron microscope, Rona and Heike for their support during measurements.

Special thanks also to the scientists of the μ-spot beamline at BESSY II, Dr. Chenghao Lee and Dr. Stefan Siegel for their help during many days of measurements.

I also would like to thank the external collaborators, Monika Kumari and Ann M. Hirt for the work they did on the magnetic measurements and Éva Tompa and Mihály Pósfai for tons of TEM images they made.

I want to thank all the current and former group members that made working in the magnetogroup so enjoyable: Thank you André, Antje, Assaf, Carmen, Christophe, Erika, Janet, Gauthier, Julia, Karin, Katharina, Livnat, Maria, Mathieu, Matthew, Michal, Paul, Peter, Sara, Teresa, Tina, Victoria. Special thanks to Jens for his never tiring patience when helping me during the last years.

I also want to thank all the other members of our department, especially Dr. Wouter Habraken, Dr. Luca Bertinetti for their support with the chapter about the activation energy.

Last but most, I want to thank Agata and my family for their love and endless support.

Thank you.

Table of Contents

Abstract

Magnetite is an iron oxide, which is ubiquitous in rocks and is usually deposited as small nanoparticulate matter among other rock material. It differs from most other iron oxides because it contains divalent and trivalent iron. Consequently, it has a special crystal structure and unique magnetic properties. These properties are used for paleoclimatic reconstructions where naturally occurring magnetite helps understanding former geological ages. Further on, magnetic properties are used in bio- and nanotechnological applications – synthetic magnetite serves as a contrast agent in MRI, is exploited in biosensing, hyperthermia or is used in storage media.

Magnetic properties are strongly size-dependent and achieving size control under preferably mild synthesis conditions is of interest in order to obtain particles with required properties. By using a custom-made setup, it was possible to synthesize stable single domain magnetite nanoparticles with the co-precipitation method. Furthermore, it was shown that magnetite formation is temperature-dependent, resulting in larger particles at higher temperatures. However, mechanistic approaches about the details are incomplete.

Formation of magnetite from solution was shown to occur from nanoparticulate matter rather than solvated ions. The theoretical framework of such processes has only started to be described, partly due to the lack of kinetic or thermodynamic data. Synthesis of magnetite nanoparticles at different temperatures was performed and the Arrhenius plot was used determine an activation energy for crystal growth of 28.4 kJ mol^{-1}, which led to the conclusion that nanoparticle diffusion is the rate-determining step.

Furthermore, a study of the alteration of magnetite particles of different sizes as a function of their storage conditions is presented. The magnetic properties depend not only on particle size but also depend on the structure of the oxide, because magnetite oxidizes to maghemite under environmental conditions. The dynamics of this process have not been well described. Smaller nanoparticles are shown to oxidize more rapidly than larger ones and the lower the storage temperature, the lower the measured oxidation. In addition, the

magnetic properties of the altered particles are not decreased dramatically, thus suggesting that this alteration will not impact the use of such nanoparticles as medical carriers.

Finally, the effect of biological additives on magnetite formation was investigated. Magnetotactic bacteria are able to synthesize and align magnetite nanoparticles of well-defined size and morphology due to the involvement of special proteins with specific binding properties. Based on this model of morphology control, phage display experiments were performed to determine peptide sequences that preferably bind to (111)-magnetite faces. The aim was to control the shape of magnetite nanoparticles during the formation. Magnetotactic bacteria are also able to control the intracellular redox potential with proteins called magnetochromes. MamP is such a protein and its oxidizing nature was studied *in vitro* via biomimetic magnetite formation experiments based on ferrous ions. Magnetite and further trivalent oxides were found.

This work helps understanding basic mechanisms of magnetite formation and gives insight into non-classical crystal growth. In addition, it is shown that alteration of magnetite nanoparticles is mainly based on oxidation to maghemite and does not significantly influence the magnetic properties. Finally, biomimetic experiments help understanding the role of MamP within the bacteria and furthermore, a first step was performed to achieve morphology control in magnetite formation via co-precipitation.

Zusammenfassung

Magnetit ist ein Eisenoxid, welches ein häufiger Bestandteil in Mineralen ist und normalerweise als nm-großen Teilchen unter anderem Gesteinsmaterial verteilt ist. Es unterscheidet sich in seiner Zusammensetzung von den meisten anderen Eisenoxiden, da es sowohl divalente als auch trivalente Eisenoxide enthält. Die Folge ist eine besondere Kristallstruktur und somit einzigartige magnetische Eigenschaften. Diese Eigenschaften werden bei paläoklimatologischen Rekonstruktionen genutzt, bei denen natürlich vorkommender Magnetit hilft, die Bedingungen vergangener Zeitalter zu verstehen. Weiterhin werden die magnetischen Eigenschaften in bio- und nanotechnologischen Anwendungen genutzt. Synthetischer Magnetit dient als Kontrastmittel in der MRT, in biologischen Sensorsystemen, bei Hyperthermie-Behandlungen oder als Grundlage für Datenspeichermedien.

Da die magnetischen Eigenschaften im nm-Bereich stark von der Größe der Teilchen abhängen, ist eine möglichst präzise Kontrolle der Größe von enormer Bedeutung. Mit Hilfe eines maßgefertigten Syntheseaufbaus war es möglich durch Mitfällung Teilchen oberhalb des superparamagnetischen Schwellenwerts zu produzieren. Außerdem konnte eine Temperaturabhängigkeit gezeigt werden; höhere Temperaturen während der Magnetit-Bildung resultieren in größeren Teilchen. Der Prozess dahinter ist jedoch noch nicht vollständig geklärt.

Die Bildung von Magnetit in wässriger Lösung erfolgt nicht über Ionen, sondern wird über die zwischenzeitliche Bildung von nm-großen Vorläufern realisiert. Unter Berücksichtigung dieser Vorläufer wurde die Bildung von Magnetit in einen neuen theoretischen Rahmen gesetzt, jedoch mangelt es bisher an kinetischen Daten. Durch die Synthese von Magnetit bei unterschiedlichen Temperaturen konnte mit Hilfe des Arrhenius-Plots eine Aktivierungsenergie für das Kristallwachstum von 28.4 kJ mol^{-1} ermittelt werden. Dieser Wert deutet auf einen diffusionskontrollierten Prozess hin.

Auch die Alterung von Magnetit-Nanopartikeln spielt eine wichtige Rolle, da Magnetit unter Umgebungsbedingungen zu Maghämit oxidiert wird. Deshalb wird hier eine Studie zur Alterung von Magnetit-Nanopartikeln unterschiedlicher Größe unter verschiedenen

Lagerungsbedingungen präsentiert. Kleine Teilchen tendieren zu stärkerer Oxidation im selben Zeitraum und weiterhin oxidieren die Teilchen weniger, je geringer die Temperatur ist. Da Magnetit und Maghämit sich in ihren magnetischen Eigenschaften nur geringfügig unterscheiden, werden diese durch den oxidativen Prozess nur geringfügig beeinflusst.

Als letztes wurde der Einfluss biologischer Zusätze zur Magnetit-Bildung überprüft. Magnetotaktische Bakterien sind in der Lage, Magnetit-Nanopartikel von definierter Größe und Morphologie herzustellen, involviert sind eine Reihe von spezifischen Proteinen mit speziellen Bindungseigenschaften. Darauf basierend wurden, zur Selektion spezifischer Peptidsequenzen, Phagen-Display-Experimente an einer (111)-Magnetitoberfläche durchgeführt. Diese sollten eine Morphologie-Kontrolle während der Magnetit-Synthese ermöglichen. Magnetotaktische Bakterien sind außerdem in der Lage das intrazelluläre Redox-Potential mit Hilfe von Proteinen, den Magnetochromen, zu kontrollieren. MamP ist eines dieser Proteine und sein oxidatives Potential wurde in einer *in vitro*-Magnetit-Synthese überprüft. Der Einsatz von Fe^{II} ergab sowohl Magnetit als auch trivalente Eisenoxide als Produkte.

Diese Arbeit ermöglicht einen Einblick in die grundlegenden Mechanismen der Magnetit-Bildung, welche unter nicht-klassischen Bedingungen abläuft. Die Alterung der Nanopartikel, welche hauptsächlich die Oxidation zu Maghämit beinhaltet, hat nur geringen Einfluss auf die magnetischen Eigenschaften. Biomimetische Experimente halfen die Rolle von MamP innerhalb der Bakterien zu verstehen und zuletzt wurde ein erster Versuch unternommen, die von den Bakterien erreichte Morphologie-Kontrolle auch *in vitro* zu ermöglichen.

1 Introduction

Magnetite (Fe_3O_4) is a naturally occurring magnetic iron oxide mineral, which has numerous bio- and nanotechnological applications [1], [2]. The magnetic properties of magnetite nanoparticles are typically used in magnetic inks, storage media or in biomedical applications like magnetic resonance imaging (MRI), hyperthermia treatment or drug delivery [1], [2]. Magnetic properties of iron oxides in general and of magnetite in particular are in addition used in geo- and paleomagnetism since these minerals preserve the main vectors of the Earth magnetization [3] and are thereby used to reconstruct past continental positioning as well as climates [4], [5]. Furthermore, many living organisms use magnetite to coordinate their movement with the help of the Earth's magnetic field – magnetotaxis in magnetotactic bacteria [6] is one example.

Magnetic properties of magnetite nanoparticles typically depend on their size, morphology and assembly. Particles smaller than about 20 – 30 nm are so-called superparamagnetic (SP) [7], i.e. they only have a measurable magnetic signal when placed in an external magnetic field. Larger nanoparticles have stable domains with intrinsic and permanent magnetic moments. Particles with isometric shapes from 20 – 30 nm to about 80 – 100 nm fall within the stable single domain (SSD) size. Larger particles are in the multi domain size range, in which several magnetic domains coexist, thereby reducing the magnetostatic energy [8]. The effect of size and morphology have already been studied in the past [9], [10] and here synthesis of SSD particles at different temperatures, the effect of size on alteration as well as results on magnetite synthesis with additives are presented.

In natural rock, magnetite is usually formed via anaerobic oxidation of ferrous hydroxides, for instance occurring in cooling magma [3]. Synthetic paths to synthesize magnetite nanoparticles are sol-gel reactions, hydrothermal reactions or synthesis by co-precipitation [1]. Co-precipitation is a very simple and efficient way to synthesize magnetite, the high yield and ambient temperatures make it very interesting for industry. However, formation of magnetite nanoparticles via co-precipitation method is accompanied by poor size control and broad size distribution.

Processes behind crystal formation and growth are of interest since a long time and have been investigated experimentally [11]–[13] as well as computationally [14]–[16]. However, the mechanisms associated with the crystallization processes have often remained unclear, specifically in the case of aqueous processes. The classical nucleation theory [17] considers crystals being formed from single ions or molecules and was successfully utilized to describe crystallization pathways for many years. Recent studies, predominantly on non- or poorly soluble salts showed however strong evidences for alternative nucleation routes. These include the aggregation of ion-association complexes (calcium phosphate [18]), clusters (calcium carbonate [19]) or primary particles (iron oxides [20]). The classical nucleation theory has thus been amended to take into account the presence of this nanoparticulate matter in the pre-nucleation stage.

The growth of crystals at equilibrium conditions is usually described by the process of Ostwald ripening [21], which assumes a growth of larger particles at the expense of smaller ones. Similar to classical nucleation theory it was considered for a long time that crystals grow through the attachment of ion-like species. Theories for crystal growth based on surface energy, diffusion or dislocations in the crystal surface were discussed extensively [17]. A kinetic model was developed by Lifshitz, Slyozov [22] and Wagner [23] to describe crystal growth at equilibrium. But recently it was shown that in some systems growth follows more complex mechanisms, especially in nonequilibrium systems investigated in this thesis. Oriented attachment plays a role in many systems [24]–[26] where nanoparticles are assembled from small nanoparticles of a few nm in size. Modifications of the LSW kinetics are applied and especially in case of magnetite formation and growth from solution, it was proposed that the process is reaction-limited [20].

After the synthesis of particles of controlled size and properties it is important to keep the properties stable or to study possible changes. In case of magnetite nanoparticles the interests focus on the magnetic properties. Oxidative processes typically result in structural changes and thus influence these properties. Hence, in order to define storage conditions to e.g. keep drugs in a functional state and to better understand the mechanism of rock magnetization acquisition and evolution by environmental magnetite nanoparticles, it is necessary to understand how magnetite nanocrystals evolve when exposed to atmospheric oxygen. Such a process indeed reflects diagenetic processes observed on Earth's surface or

when nanoparticles are stored in aqueous solutions where maghemite (γ-Fe_2O_3) is the natural weathering product of magnetite, when oxygen causes the oxidation of the mixed Fe^{II}/Fe^{III} oxide to the pure Fe^{III} oxide [3]. Several techniques have been used to study structural as well as magnetic properties of the magnetite/maghemite mixtures. X-ray absorption spectroscopy (XAS) was used to quantify the oxidation states of iron in minerals or to study the local order around the iron sites [27]–[29]. Furthermore the stoichiometric ratio has been studied via acidic dissolution, Mössbauer spectroscopy [30] or X-ray magnetic circular dichroism (XMCD) [31]. In this thesis the compostition of the magnetite/maghemite mixture was studied with high-resolution X-ray diffraction and magnetometric measurements.

In nature, Magnetotactic bacteria (MTB) show the ability to perfectly control size and morphology of particles and to obtain narrow size distributions to produce magnetite particles with required properties. MTB are able to synthesize MNP in the SSD range, arrange them in chains and use them as a compass needle to orientate in the Earth's magnetic field [6]. The whole process, iron uptake, formation of magnetite, arrangement in chains is controlled with the help of MTB-specific proteins, so-called Mam or Mms proteins. There are proteins involved that enable precise control of size and morphology during the formation of magnetite. Another important process is the redox control within the cell. MamP, a cytochrome-like protein, is supposed to play an important role in the iron-related redox-processes [32].

1.1 Objectives and Scope of Work

The general aim of this work was a better understanding of the formation of magnetite nanoparticles by co-precipitation. Magnetic properties, for example, strongly depend on the particle size, the size distribution or morphology of the particles. Particles beyond the superparamagnetic size range can be synthesized within a temperature range of 5 – 25 °C [33].

However, the process behind magnetite formation is still poorly understood. First mechanistic insights were given, where the formation was based on a precursor step with primary particles. In this work magnetite nanoparticle growth was studied at different

temperatures to determine growth rates and to further calculate an activation energy of crystal growth. Possible rate-determining steps were discussed based on the mechanism suggested earlier in the group [20] and with the activation energy calculated in this thesis.

Once the particles in the desired size-range were obtained, it is crucial to keep their properties stable. Prevention of structural changes is desirable to avoid a strong decrease of magnetic properties. Particles of different size were studied with high-resolution X-ray diffraction accompanied by magnetometric hysteresis measurements to display possible changes in the magnetic properties. Storage under different conditions was investigated and the observed results were discussed in the light of potential biomedical applications.

Besides purely synthetic experiments, syntheses with biological additives were performed. For example, MamP is a cytochrome-like protein, which is present in all magnetotactic bacteria. In a collaborative effort with the group of D. Pignol (CEA Cadarache, France), the role of MamP and its oxidative potential was demonstrated *in vitro*.

Another outstanding feature is the morphology control during formation of particles within the MTB. Bullet-shaped, flake-like or isotropic particles are formed and one approach is the influence of the MTB-specific proteins that might reach control by special binding properties to different crystal faces of magnetite. Phage display experiments were performed to reveal possible peptide sequences that preferably bind to (111)-faces of magnetite crystals. The peptide sequences obtained did not show any homology to bacterial proteins. In addition, testing the peptides *in vitro* did not reveal any direct and evident conclusion. An outlook is given about how this approach can be developed further to result in morphology-controlled nanoparticle growth.

2 Methods

2.1 Co-Precipitation

2.1.1 Background

The aqueous co-precipitation method is a very simple but efficient technique where magnetite is formed from ferrous and ferric chloride solutions. This process was first mentioned by LeFort in 1852 by [34] and in 1981 Massart described a method of forming magnetite by adding ferric and ferrous chloride solutions to ammonia solution [35].

In my work, magnetite formation is caused by setting the pH to 9, then adding a stoichiometric mixture of Fe^{II}/Fe^{III} chloride and concomitantly keeping the pH constant by further NaOH addition (Equation (2.1)). Inert gas atmosphere is necessary to prevent oxidation of Fe^{II} and enable maghemite formation. This method enables magnetite formation at ambient conditions, which may reflect physiological conditions in magnetite biomineralizing organisms. As described in the introduction, the mechanism behind magnetite formation is still unclear and will be a topic of this thesis.

$$FeCl_2 + 2FeCl_3 + 8NaOH \rightarrow Fe_3O_4 + 4H_2O + 8NaCl \qquad (2.1)$$

2.1.2 Experimental

Materials and Preparation

Aqueous iron solutions were prepared from ferrous chloride tetrahydrate (Sigma-Aldrich, No. 44939-50G) and ferric chloride hexahydrate (Bernd Kraft, No. 15249.1600). Experiments were performed with the stoichiometric ratio of magnetite (Fe^{II}/Fe^{III} = ½) and total iron concentrations of 1 M for experiments without additives and 0.1 M for experiments with additives. For experiments with the additive MamP a 0.1 M solution of Fe^{II} was used. 0.1 M and 1M sodium hydroxide solutions (Merck, No. 1.09141.1000 and No. 1.09137.1000) were used for titration. All solutions were degassed with nitrogen for at least 20 minutes before use and kept under nitrogen atmosphere.

Experimental Setup

The Experiments were performed with two different systems that consist of a titration device (titration of NaOH to control the pH), a dosing device (to dose iron solutions) and a software to control the system (everything from Metrohm AG, Herisau, Switzerland). Details of both are listed below:

Table 2.1: Detailed composition of the two titration systems, the first, "old" system was purchased in 200x and the second, "new" system was purchased in 2012.

first system	second system
titration device: 719S Titrino with a 5 mL exchange unit	titration device: 888 Titrando with a 5 mL exchange unit
dosing device: 776 Dosimat with a 1 mL exchange unit	dosing device: 805 Dosimat with a 1 mL exchange unit
software: tiamo 1.0	software: tiamo 2.3

Experiments were performed with addition rates of1 µL min^{-1}. To enable such low dosing rates commercially available tube endings (d ≈ 2 mm) were exchanged with microloader tips (Eppendorf, Hamburg, Germany, No. 5242 956.003) as inlets to the reactor vessel. Furthermore, it was necessary to modify the 805 Dosimat because of software limitations; the minimum dosing rate that could be set in the software was 10 µL min^{-1}. The problem was solved by simulating a 10 mL exchange unit with a dosing rate of 10 µL min^{-1} with the 1 mL exchange unit, which resulted in a dosing rate of 1 µL min^{-1}. The reactor vessels (50 mL, No. 6.1418.110) were equipped with a thermostat jacket and kept at a constant temperature with the thermostat Julabo F12 (JULABO GmbH, Seelbach, Germany). Solutions were stirred with a mechanical stirrer to avoid interactions between the magnet and the magnetite formation. The pH was controlled with a glass electrode (Biotrode, No. 6.0224.100) which was regularly cleaned with pepsin/HCl and recalibrated with commercially available calibration buffers (pH = 4, 7, 10). Figure A1a, representative for both, shows the "old" system with the thermostat (1), the dosing device (2), the reactor (3), the titration device (4), the computer (5) and the nitrogen supply (6). A schematic side-view of the reactor illustrates

the processes more clearly (Figure A1b). The thermostat sets the temperature (1), iron and NaOH are pumped into the reactor (2, 4), a magnetic stirrer and the electrode control the system (5', 5'') and a constant nitrogen gas stream (6) ensures oxygen-free atmosphere. All components were inserted into the reactor over standard NS14 ground glass joints, (2, 4, 6) with rubber gum septa.

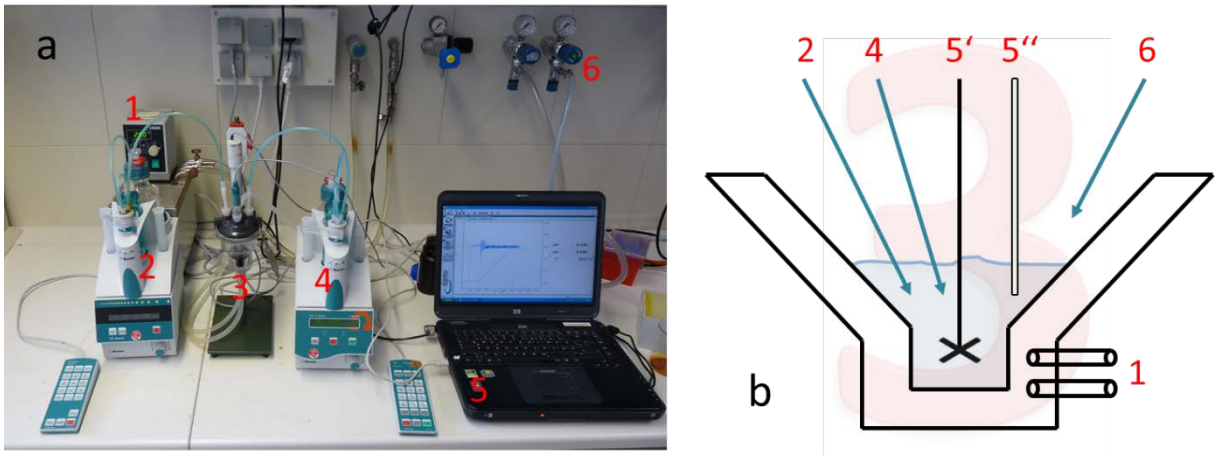

Figure 2.1: (a) The first titration system with the thermostat 1, the dosing device 2, the reacter vessel 3, the titration device 4, the computer 5 and the N_2 supply. (b) scheme of the reactor 3 with the thermostat jacket and the water exchange 1, the dosing device, the titration device, the stirrer 5', the electrode 5'' and the N_2 supply 6.

Formation of Magnetite Nanoparticles without Additives

The reactor was filled with 10 mL of deionized water and degassed with nitrogen for 20 min. The reactor and the solutions in use were kept under nitrogen atmosphere during the synthesis and then the pH was adjusted to 9 by 1 M NaOH titration. The stoichiometric 1 M Fe^{II}/Fe^{III}-chloride solution was added with 1 µ min^{-1} and the pH was kept constant due to further NaOH titration. For time resolved experiments samples of 60 µL were taken every hour and stored in the fridge. After eight hours the synthesis was finished and the residual material was also stored in the freezer and, in the special case of the alteration studies, in the fridge, at ambient temperature and ambient temperature plus argon flush.

Formation of Magnetite Nanoparticles with Additives

The first set of experiments was made with MamP. The reactor was filled with 14 mL of a 1.15 g L^{-1} MamP solution and degassed with nitrogen for 20 minutes. Instead of using a stoichiometric iron solution these experiments were performed by adding 0.1 M ferrous chloride solution with 1 µL min^{-1} and pH control was done with 0.1 M NaOH solution. Sampling was done after 10, 20, 30, 40, 50 and 60 min and at the end. Syntheses lasted 11 hours and control experiments without protein in the reactor were performed as well. To prevent subsequent oxidation the sample was also purged with nitrogen before storage in the fridge.

The second set of experiments (t = 4 h) was realized with peptides found by Phage Display experiments. The peptide concentration was 0.01 g L^{-1} and the stoichiometric 1 M Fe^{II}/Fe^{III}-chloride solution was added with 1 µL min^{-1}. The pH was controlled with 0.1 M NaOH solution. Two different strategies were pursued, the first was to add the peptide before starting the synthesis and the second was to add the peptide after two hours. The idea was to either let the peptide influence the nucleation step (direct adding) or the growth process (delayed adding).

Storage Conditions for Alteration Experiments

A set of four samples of different particle size was subjected to 6 analyses over a time range of 18 months. Directly after the synthesis the particles were kept in original solution and stored:

- in the freezer (-20 °C),
- in the fridge (4 °C),
- at room temperature (a.t.)
- and at room temperature flushed with Argon (a.t. + Ar).

These conditions were chosen to represent common ways of storing goods, not only in science but also in industry, medicine etc. The last – flushed with Argon – was used to reflect storage under inert conditions.

Oxygen Sensing before and during the Synthesis

Preliminary tests with an oxygen probe (NTH-PSt1-L5-TF-NS40/0.8-OIW, PreSens Precision Sensing GmbH, Regensburg) were performed in order to find the right level of nitrogen gas streaming. Tests helped to determine on the one hand how long solutions have to be degassed and on the other hand the appropriate level of pressure of the gas stream during the synthesis. Here it is important to keep nitrogen atmosphere during the entire synthesis, in particular during the sampling process, where the reactor has to be opened for several seconds.

Prior degassing tests show that a 100 mL bottle of iron solution is nearly oxygen free after 5 minutes of gas stream with 100 mbar of nitrogen (Figure 2.2). At synthesis times of eight hours and temperatures near ambient conditions, the evaporation of water can start playing a significant role during the synthesis. Significant volume changes influence the nucleation and growth process and reliable results can only be achieved if constant reaction conditions are guaranteed. To avoid unnecessarily strong gas streams but to ensure oxygen-free atmosphere in the reactor the setup was developed further. Figure 2.3 shows that oxygen enters the system during a synthesis if sampling is included for a nitrogen stream of 50 mbar. A pressure of 100 mbar ensured nitrogen atmosphere during the sampling procedure.

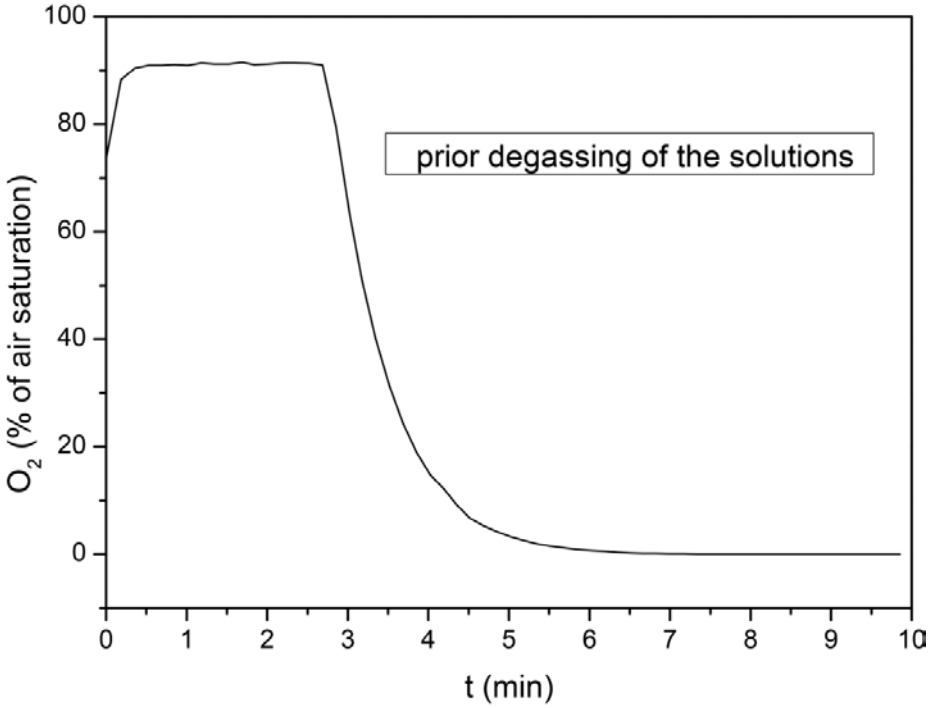

Figure 2.2: A plot of oxygen concentration over time for an open bottle filled with 100 mL iron solution and degased with 0.1 bar N_2 gas stream. The gas streaming was started after three minutes and immediate decrease of O_2 concentration can be seen.

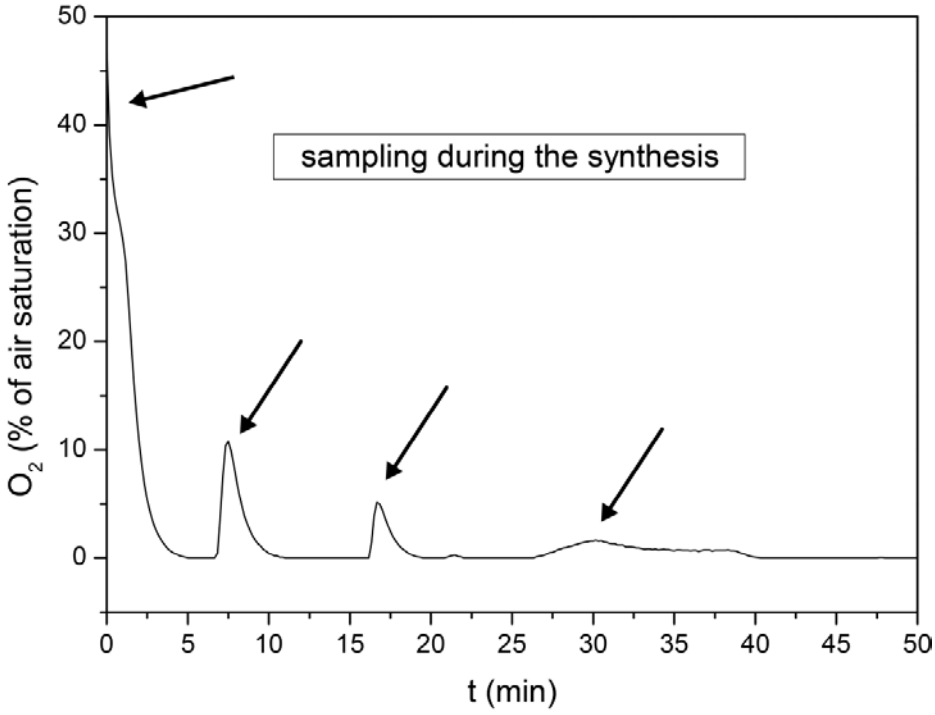

Figure 2.3: A plot of oxygen concentration over time for the reactor vessel filled with 10 mL of water and a nitrogen stream of 50 mbar. (a) The reactor is filled with 10 mL H_2O, kept nearly closed and the oxygen concentration is decreasing to zero within 5 min. (b) By opening the reactor for 30 seconds there is immediate increase of O_2-concentration up to 10%, which drops to zero after closing within 2 minutes. (c) By opening the reactor for 10 seconds there is still increase of O_2-concentration up to 5%. (d) With a nitrogen stream pressure of 10 mbar it not possible to ensure oxygen free atmosphere even with a fully closed reactor.

2.2 X-Ray Diffraction

2.2.1 Background

The wavelength of X-rays is in the range of 10^{-12} – 10^{-8} m, which is comparable to bond lengths in molecules or spacing of atoms in crystals. The elastic, coherent scattering of X-rays by the long-range ordered atoms of a crystal therefore results in a diffraction pattern that is suitable to study the structure of the crystal. When the incoming beam is elastically scattered we can define a scattering vector ***q***, which is the difference of the wave vectors of the scattered beam $\boldsymbol{k_f}$ and the incoming beam $\boldsymbol{k_i}$ [36]:

$$\vec{q} = \overrightarrow{k_f} - \overrightarrow{k_i} \qquad (2.2)$$

The magnitude of the scattering vector is:

$$|\vec{q}| = 2\left|\overrightarrow{k_f}\right| \sin\theta \qquad \text{with} \qquad \left|\overrightarrow{k_f}\right| = \frac{2\pi}{\lambda} \qquad (2.3)$$

In a crystal of nm-size multiple scattering happens due to many atoms being hit by the beam. Due to the translational periodicity of the crystal, constructive and destructive interference leads to a diffraction pattern. The so-called Bragg reflections are characteristic for a crystalline material. It is considered that a crystal is composed of a stack of lattice planes *hkl* with the atoms sitting on these lattice planes (black lines in Figure 2.4).

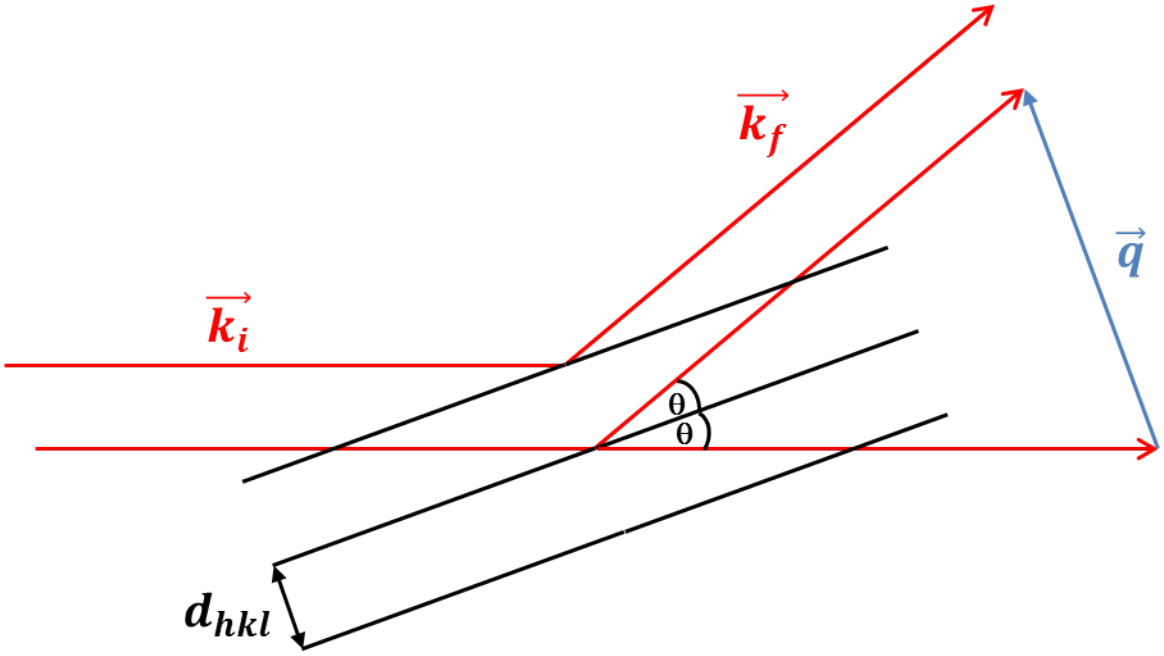

Figure 2.4: Scheme of Bragg reflections. the vector of the incoming beam k_i is reflected by the points on the lattice planes hkl, resulting in the vector of the scattered beam k_f. Characteristic parameters are the diffraction angle θ and the scattering vector q.

Constructive interference can only occur if the difference in path length d_{hkl} between two lattice planes is an integer multiple of the wavelength λ of the X-ray beam. With constant λ and d_{hkl} there is only constructive interference at certain angles θ (Bragg reflections). This relation is described by Bragg's law [37]:

$$2d_{hkl} \sin\theta = n\lambda \qquad (2.4)$$

The magnitude of the q-vector can be calculated with Equation (2.3) and (2.4):

$$|\vec{q}| = \frac{2\pi}{d_{hkl}} \qquad (2.5)$$

and the corresponding values of q_{hkl} for magnetite and maghemite are shown in Table 2.2. After the determination of q_{hkl} it is possible to calculate the lattice parameter a. For a cubic crystal the relation is given by [38]:

$$\frac{1}{d_{hkl}} = \frac{\sqrt{h^2 + k^2 + l^2}}{a} \qquad (2.6)$$

and with (2.5) the lattice parameter can be calculated from the q-vector:

$$a = \frac{2\pi\sqrt{h^2 + k^2 + l^2}}{q_{hkl}} \qquad (2.7)$$

The similar crystal structures of magnetite and maghemite result in similar XRD patterns. Except for a shift to larger q-values for maghemite the peak positions and intensities are very similar for most of the peaks (see Table 2.2 and Figure 2.5). This peak shift will later be used to investigate the alteration of magnetite nanoparticles over time by observing the peak shift.

Table 2.2: The XRD data of magnetite, maghemite and hematite: hkl, intensities and q-values were acquired from [3].

Lattice plane	Magnetite		Maghemite		Lattice plane	Hematite	
hkl_{cub}	I(%)	q_{hkl} (nm^{-1})	I(%)	q_{hkl} (nm^{-1})	hkl_{hex}	I(%)	q_{hkl} (nm^{-1})
111	8	12.9605	6	13.0380	012	30	17.0553
220	30	21.1644	30	21.2909	104	100	23.2711
311	100	24.8175	100	24.9658	110	70	24.2500
222	8	25.9209	-	-	113	20	28.4693
400	15	29.9309	15	30.1099	024	40	34.1366
422	10	36.6578	9	36.8770	116	45	37.0886
511	30	38.8815	20	39.1139	018	10	39.2896
440	40	42.3288	40	42.5818	214	30	42.2854
					300	30	43.2190

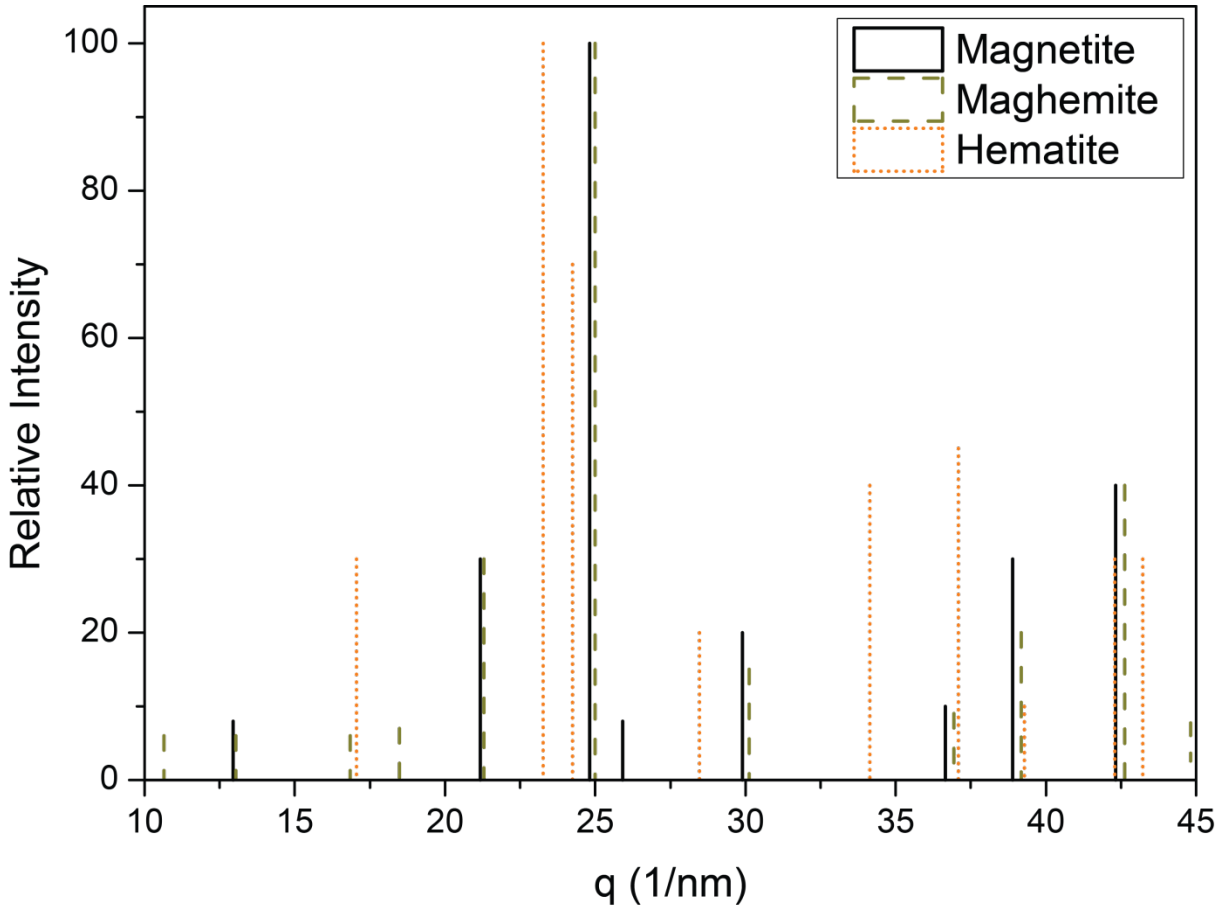

Figure 2.5: Theoretical XRD-patterns of magnetite (black, solid line) and maghemite (dark yellow, dashed line) and hematite (orange, dotted line). The most intensive peaks of each phase are set to 100%.

As a consequence of Bragg's law the peaks or Bragg reflections of an ideal crystal are sharp (as it is indicated for magnetite and maghemite in Figure 2.5) and for perfect samples, in theory one would expect that scattering intensity for any angle θ that does not fulfill Equation (2.4) is eliminated.

In reality peaks are not sharp and their width is specified with the full width at half maximum (FWHM). The entire broadening, which is experimentally determined ($fwhm_{exp}$) is caused by the instrumental setup ($fwhm_{instr}$) due to detector point spread and beam divergence, by microstrains ($fwhm_{micro}$) that can be present in the crystals and/or by the limited size of the crystals ($fwhm_{size}$). The entire peak width is:

$$fwhm_{exp}^2 = fwhm_{instr}^2 + fwhm_{micro}^2 + fwhm_{size}^2 \quad (2.8)$$

Microstrains in the crystals are excluded due to former experiments [39] so that the $fwhm_{size}$ is calculated from:

$$fwhm_{size} = \sqrt{fwhm_{exp}^2 - fwhm_{instr}^2} \quad (2.9)$$

With the Scherrer equation [40] the average crystallite size can be calculated:

$$crystallite\ size = \frac{K\lambda}{fwhm_{size} * \cos\theta} \quad (2.10)$$

where *K* is a dimensionless shape factor. Strictly, it depends on the shape of the particles, on the indices *hkl* of the peak and on the size distribution [41]. For spherical particles it can be set to $K \approx 1$. In case of monocrystalline particles, the crystallite size is equal to the mean particle diameter. A modified version was used in this thesis to calculate the particle size from obtained peak broadening in q-units:

$$MD = \frac{2\pi}{fwhm_{size}} \quad (2.11)$$

where *MD* is the mean particle diameter.

2.2.2 Experimental

X-ray diffraction measurements were taken at the µ-Spot beam line of the BESSY II synchrotron facility of the Helmholtz-Zentrum Berlin. Special custom made sample holder

equipped with Kapton foil (Breitlander GmbH, Hamm, Germany, Cat. No. CH-440) enabled measurements of 45 samples on the same sample holder [42]. For each sample a volume of 2 – 5 µL non-diluted suspension was dried on the Kapton foil and measured in transmission with a 100 µm beam of the wavelength $\lambda = 0.82656\ nm$. 2D-diffraction patterns were recorded with a 3072 × 3072 pixel MarMosaic 225 CCD camera with 73.242 µm pixel size (Mar USA, Evanston, USA). Sample to detector distance was usually around 150 – 170 mm and exposure to the beam was 5 – 60 s per sample and measurement. Fit2D [43] and AutoFit [44] were used to calculate the exact sample-to-detector distance (for alteration experiments), the instrumental peak broadening and the full width at half maximum. All three parameters were determined by fitting the (311)-peak with a pseudo-Voigt function and the crystallite size was determined with the Scherrer equation and the corrected fwhm.

Alteration experiments

For the alteration experiments sample preparation all aliquots were dried together with an α-quartz standard [45] on the Kapton film. This quartz is very stable and peak positions are well known. Thus, the quartz can be used to determine the exact sample to detector distance and by knowing this distance the exact peak position and hence the lattice parameter of magnetite can be calculated.

Furthermore, sample preparation has a special meaning as different storage conditions and their influence on the properties could be biased by changing and keeping the conditions during the sample preparation and measurement. In general we did not differentiate between 4 °C, a.t. and -20 °C, a.t. + Ar. This could lead to a distortion of results especially for the a.t. + Ar, where an additional maghemitization due to the presence of oxygen can be observed. First, all samples at all 6 time points were treated the same, which makes it being similarly relevant for all different conditions and second, the alteration was measured in steps of several months and the time that the sample was exposed to ambient conditions because of preparation was comparatively short (2 days) and thus a post-oxidation effect because of the sample preparation is negligible.

Peak Fitting of X-ray diffraction patterns of mamP mediated syntheses

X-ray diffraction patterns of the material synthesized with mamP showed more complicated structures and overlapping peaks occurred. Cumulative peak analysis was done with Origin. The peaks were fitted with a Pseudovoigt function with multiple fit function and previous baseline subtraction.

2.3 Transmission Electron Microscopy

2.3.1 Background

In this thesis, transmission electron microscopy (TEM) was used to characterize the physical dimensions, the morphologies, structures and compositions of the nanoparticles. In particular, high-resolution transmission electron microscopy (HR-TEM) was used to determine the crystalline phase of one particle and selected area diffraction (SAD) was used to determine the phase of a multi-particle area. The theory behind SAD is similar to that of X-ray diffraction (section 2.2). TEM was performed in Golm (Zeiss 912 Omega) and in collaboration with the group of M. Pósfai, Pannonia University (JEOL 2000FX and Philips CM20).

2.3.2 Experimental

Suspensions were usually measured with original concentration and without washing. A droplet of 10 µL of the nanoparticle suspension was put on a Parafilm slice and on top a carbon film Cu grid. To let the particles adsorb to the carbon surface it was kept there for 15 min and afterwards, the liquid phase was removed with a precision wipe. The TEM images were obtained with:

- JEOL 2000FX (Arizona State University, USA) and Philips CM20 (Institute of Technical Physics and Materials Science, Hungary)
    - Figure 3.1, including HRTEM, section 3.2
    - Figure 5.5, HRTEM, section 5.4.2

- Zeiss 912 Omega (MPIKG, Germany) and JEOL 3010 electron microscope (Institute of Technical Physics and Materials Science)
    - Figure 4.3, section 4.2
    - Figure 5.4, section 5.4.2
    - Figure 6.1, section 6.3.1
    - Figure 6.4, section 6.3.2
    - Figure 6.5, section 6.5.2

2.4 Magnetometry

2.4.1 Background

A material that is brought into a magnetic field *H* experiences a magnetization *M* and the magnetic susceptibility χ_m is a material constant that depends on composition or structure of the material [46].

$$M = \chi_m * H \qquad (2.12)$$

A ferrimagnetic material like magnetite has relatively high magnetic susceptibility and shows open hysteresis loops (Figure 2.6). An external magnetic field is applied to the material and a number of parameters can be determined, which can give information about for instance composition or structure. The saturation magnetization M_S is the maximum magnetization that can be reached while increasing the magnetic field. This is the point where all spins are parallel. By decreasing the field to zero, the curve does not exactly follow the former curve but leads to an intercept with the magnetization axis, which is called the magnetization remanence M_{RS}. This is the magnetization that is still left when the field is zero. Further decrease of *H* leads to saturated magnetization with opposite sign. The magnetic field at which the magnetization turns zero is called the coercivity H_C. After saturation the field can be increased again and the curve will again pass the magnetization remanence and the coercivity until the saturation magnetization is reached again. The coercivity of the remanence H_{CR} is this value of a magnetic field where reduction to zero magnetic field

change would lead to exact zero net remanence. The isothermal remanent magnetization (IRM) is that magnetization limit at which an increase of the magnetic field does not result in increased magnetization anymore.

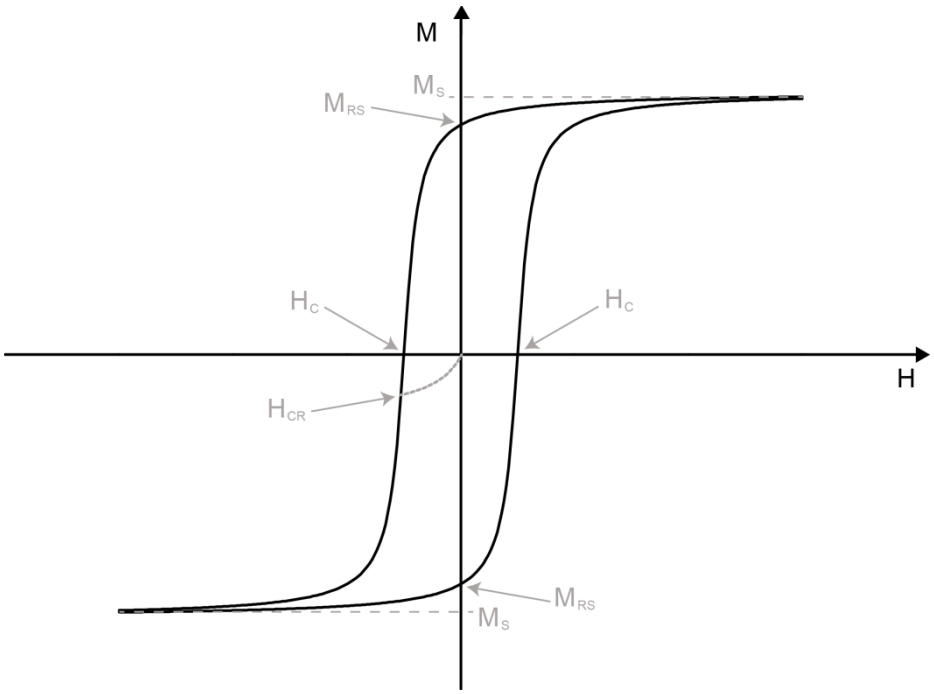

Figure 2.6: Hysteresis loop of a magnetic material with the parameters that are usually used to characterize the magnetic properties: saturation magnetization (M_S), saturation remanence (M_{RS}), coercivity (H_C) and coercivity of the remanence (H_{CR}).

2.4.2 Experimental

All magnetic measurements were performed by Monika Koumari and Ann M. Hirt (ETH Zürich, Switzerland) and this section was partly adapted from [47]. The magnetic measurements were performed on the samples that were dried on a filter paper at ambient temperature in the fume-hood. The sample powders were then immobilized by placing into a gently pressed gel caps. Important to note is, all the samples were subjected to the same sample preparation. The magnetic properties of the samples were characterized by room temperature hysteresis loops, acquisition of an isothermal remanent magnetization (IRM). All measurements are performed using a Princeton Measurements Corporation (PCM) vibrating sample magnetometer (VSM). Hysteresis loops were measured between ±1 T with 100 ms averaging time in order to characterize the saturation magnetization (M_s), saturation

remanent magnetization (M_{RS}) and coercivity (H_C) of the bulk sample. IRM acquired in a backfield is done by first inducing M_{RS} at 1 T, and then demagnetizing in a backfield until -1 T to obtain the coercivity of the remanence (H_{CR}).

3 Formation of Stable Single Domain Magnetite Nanoparticles at Low Temperature

The formation of stable single domain magnetite nanoparticles at low temperature is thoroughly described in the work by Baumgartner *et al.* [33].

3.1 Background

Magnetite nanoparticle growth via co-precipitation has previously been achieved by Faivre *et al.* [48] and Vayssières *et al.* [49] but typically yielded superparamagnetic particles smaller than 10 nm and in a size range of 1.5 to 12.5 nm, respectively. Due to the low solubility of iron under neutral and alkaline pH conditions, nucleation is the dominant process as long as addition rates of Fe^{II}/Fe^{III} mixture lead to high supersaturation in the reactor. It can be shown in this chapter that such conditions are met and the production of MNP beyond the superparamagnetic size could be achieved with a rate of 1 µL min^{-1} of a 1 M Fe^{II}/Fe^{III} solution at pH 9 and different temperatures. Both X-ray diffraction and transmission electron microscopy show that, under the aforementioned conditions and after eight hours, magnetite nanoparticles of 33 to 64 nm in diameter are obtained. This is beyond the SP/SSD threshold of 20 – 30 nm. The magnetic properties measured using hysteresis loops confirm the stable single domain state of the particles.

3.2 Results

Figure 3.1a shows highly aggregated nanoparticles and high-resolution transmission electron image confirms the crystalline structure; the Fourier transform shows magnetite (110) reflections (Figure 3.1b). The size distribution range is wide, aggregated nanoparticles of a few tens of nm in size and large octahedral single crystals of magnetite up to more than 100 nm in size (indicated by the red arrows) are obtained (Figure 3.1c and d). Poorly crystalline material is consistently found in the samples alongside the nanoparticles (e.g. Figure 3.1c upper left area).

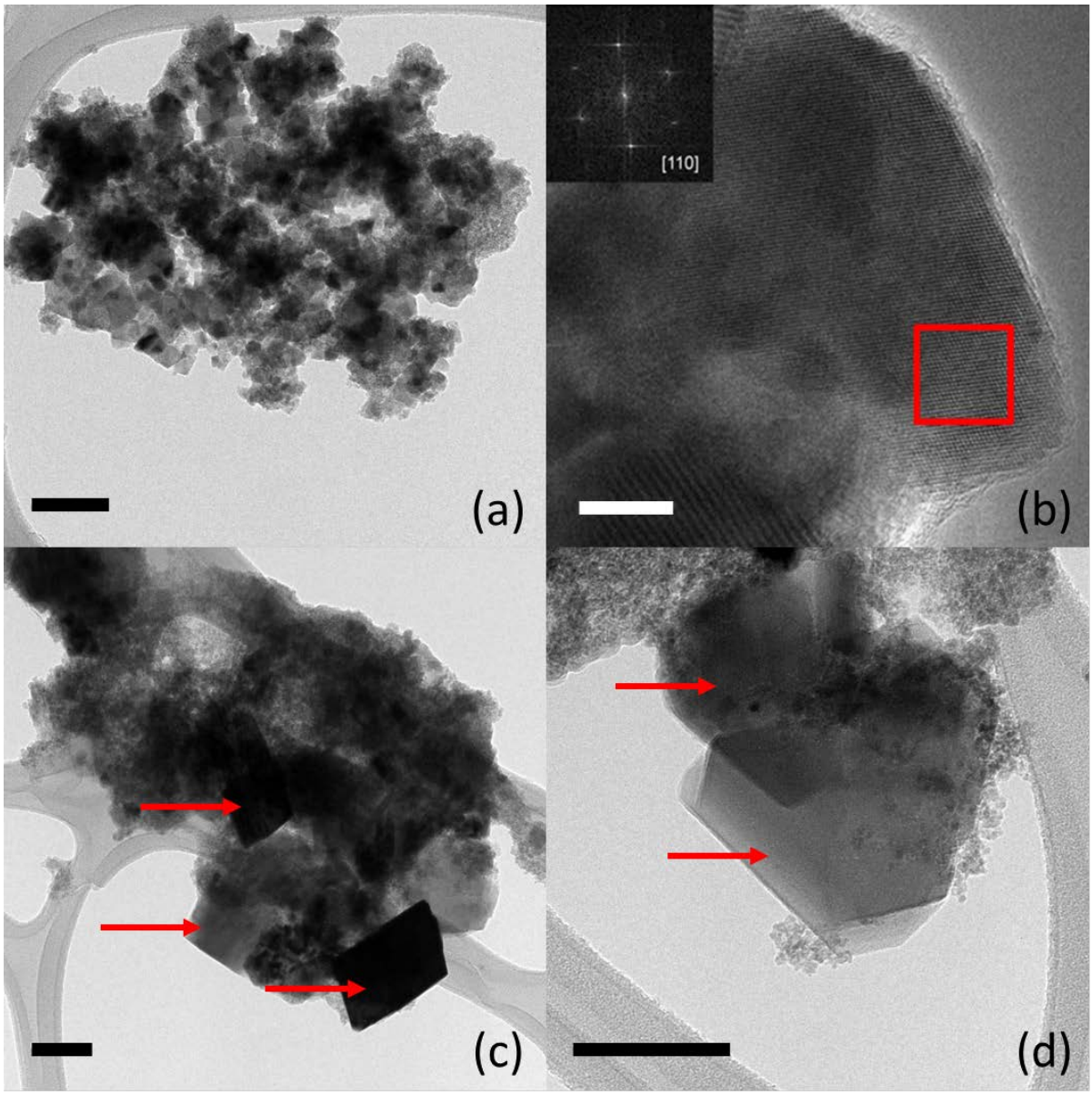

Figure 3.1: TEM images of magnetite nanoparticles (black scale bars: 100 nm and white scale bar: 10 nm). (a) Aggregated, crystalline particles. (b) HRTEM image of a particle, showing a perfectly crystalline structure, with the electron beam parallel to the [110] orientation, as indicated by the Fourier transform (in the upper left) of the boxed area. (c) and (d) show aggregates of small (10 – 50 nm) and large (>100 nm) particles. Image courtesy of Mihály Pósfai

The X-ray diffraction pattern of one representative sample confirms that the main phase is crystalline magnetite (Figure 3.2). NaCl as a side product of the synthesis is also present in the diffracation pattern. The size was determined with the help of the Scherrer equation from the full width at half maximum. Depending on the temperature during the synthesis particles from 33 to 63 nm were synthesized and their magnetic properties were analyzed.

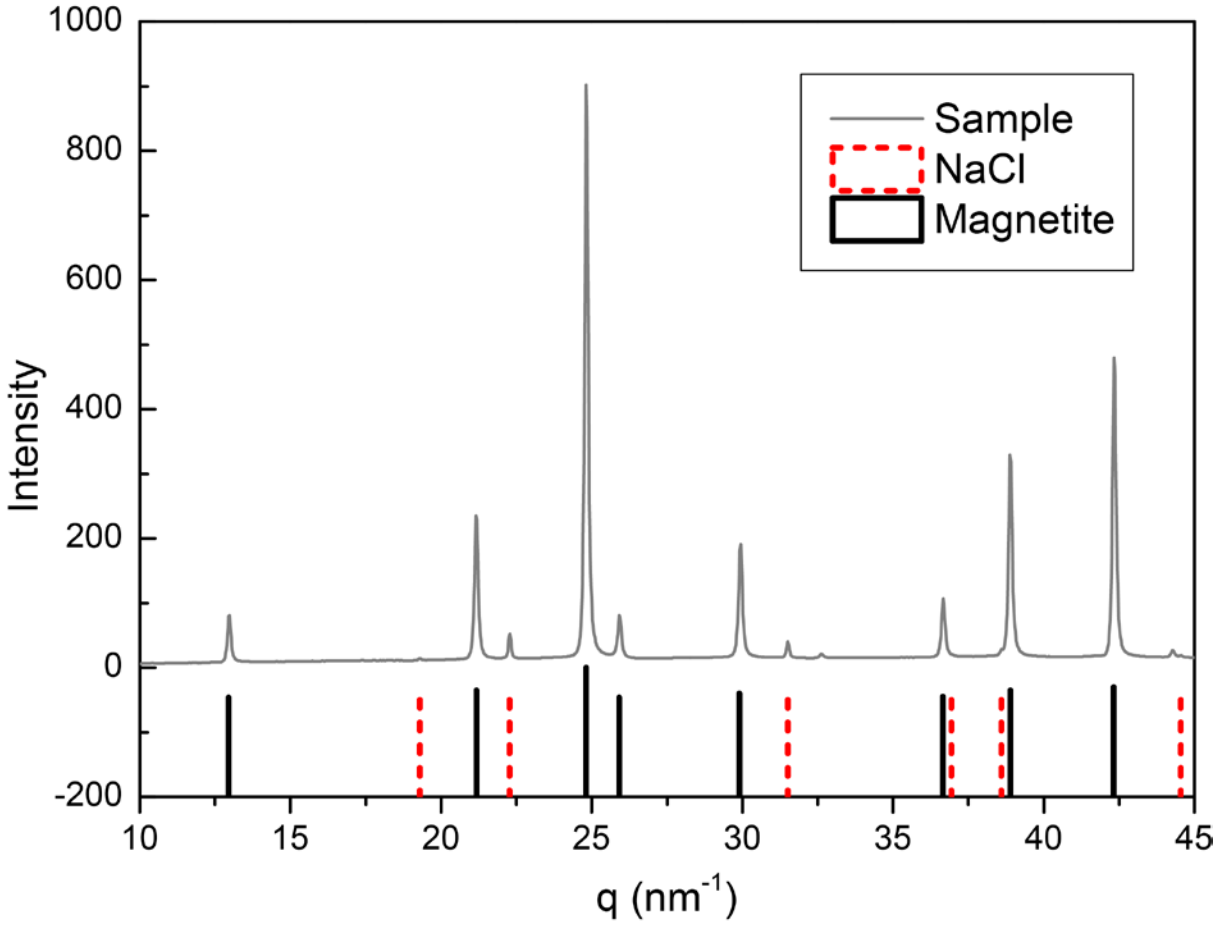

Figure 3.2: X-ray diffraction diagram showing a typical magnetite pattern (black lines) and the signature of NaCl (red dotted lines) as a side product of the synthesis.

The H-M curves show that the products of the syntheses presented in this chapter exhibit magnetic hysteresis (Figure 3.3a shows sample 121 as a representative) and IRM shows saturation of magnetization (Figure 3.3b). The values calculated for the saturation magnetization (M_S), the saturation remanence (M_{RS}) and the coercivity (H_C) of eight samples are shown in Table 3.1. Larger particles typically exhibit higher values for M_S, M_{RS} and H_C (Figure 3.4). $M_{S,sample\ 125}$ = 105.5 A m^2 kg^{-1} – a value larger than for bulk material may suggest the presence of another reduced iron species. Another tendency is that at lower temperatures, smaller particles are obtained. This is will be further discussed in the next chapter.

Table 3.1: Magnetic properties of a set of samples sorted by increasing mean particle diameter. M_S, M_{RS} and H_C indicate that particles of each and every sample are in the SSD state.

Sample	ϑ (°C)	MD (nm)	M_S (A m^2 kg^{-1})	M_{RS} (A m^2 kg^{-1})	H_C (mT)
124	5	33	75.29	8.81	6.2
166	5	39	55.1	6.6	6.2
137	10	44	51.7	6.8	7.2
99	15	45	59.5	11.9	10.7
125	15	50	105.5	17.61	9.9
123	20	52	83.81	15.22	10.4
121	25	63	87.2	13.4	8.6
103	25	64	71.1	14.6	9.9

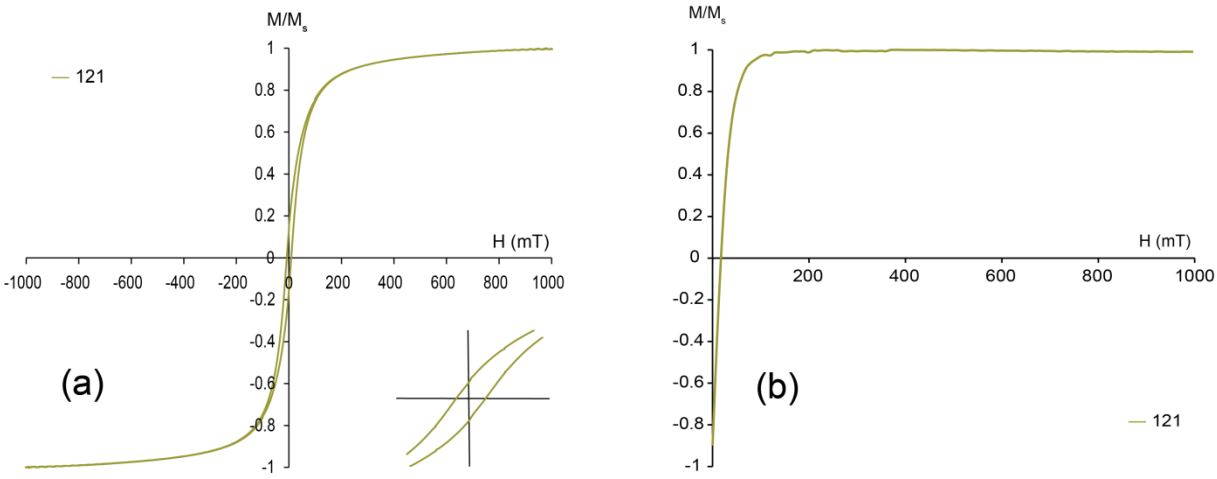

Figure 3.3: (a) Hysteresis loop of sample 121 with expanded view used to determine M_{RS} and H_C and (b) isothermal remanent magnetization curve (IRM) used to determine M_S.

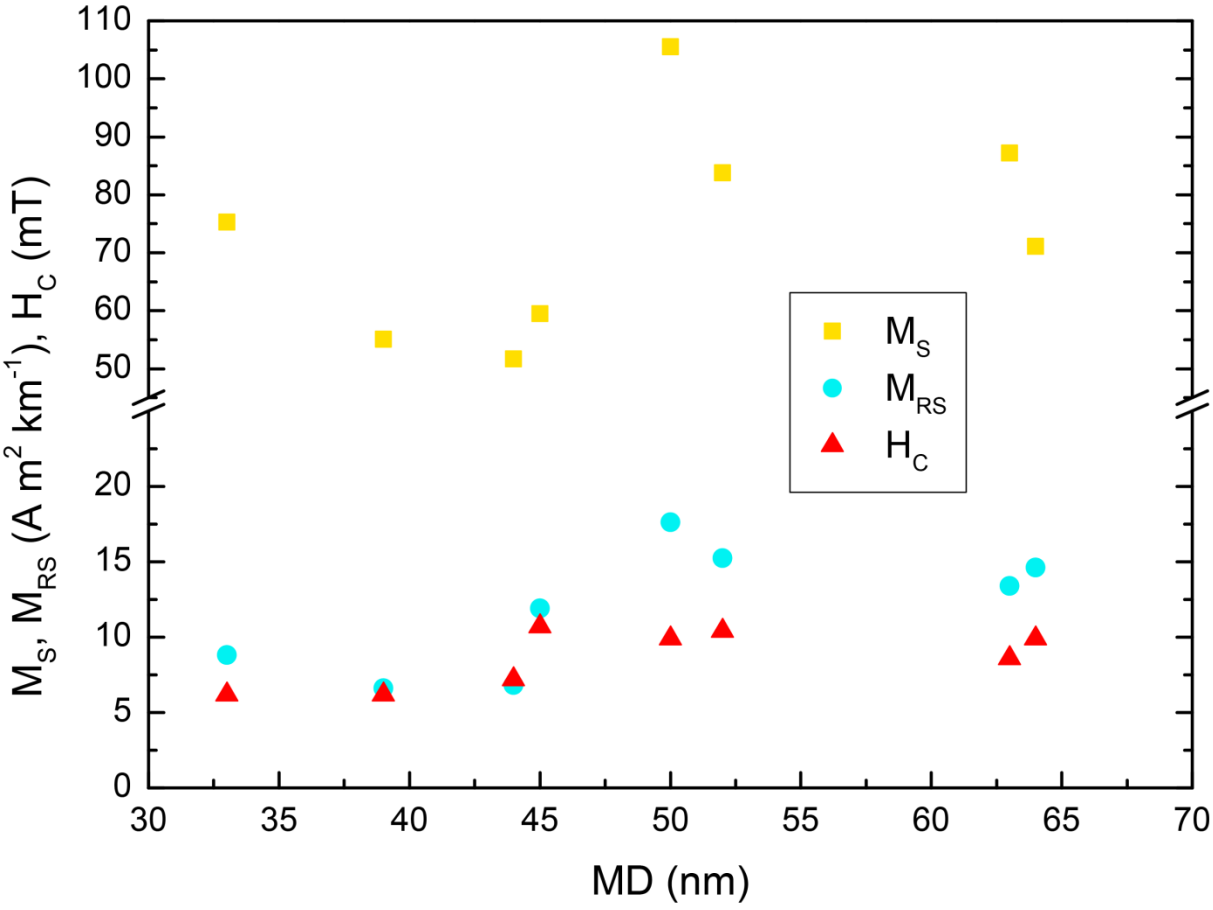

Figure 3.4: Plot of magnetic properties (M_S, M_{RS} and H_C) over MD. Ms Mrs and Hc increase with increasing particle size. The graphs confirm this behavior although a quantitative evaluation is not possible due to the limited number of data.

3.3 Discussion

A general drawback of the aqueous co-precipitation method is that particle growth usually results in broad size distributions [50], [51]. Consistent to this aspect, the particles obtained are ranging from a ferrihydrite-like precursor phase [20] (1 – 2 nm) over SP particles (MD < 20 nm) up to large particles of > 100 nm in size. The nanoparticles produced are highly aggregated. Therefore, the determination of a reliable estimation of their size distribution is not achievable using TEM images. X-ray diffraction analysis results in a mean particle diameter beyond the SP/SSD threshold (MD > 20 – 30 nm) and the SSD state could be confirmed by hysteresis measurements. Saturation magnetization values are consistent with former studies [52] and a continuous increase in H_C and M_{RS}/M_S with increasing particle size indicates “growing magnetic properties”. A plateau of H_C and M_{RS} seems to be reached for particles with MD > 50 nm. This might be the range where at least two magnetic domains a

present in the particles [33], [53]. Multi-domain regimes might be present in very large particles with MD > 100 nm (Figure 3.1).

As a summary, slow addition rates lead to a dominance of particle growth over nucleation and, at least within a broad size distribution, this method enables a size control by the synthesis duration. Another parameter to control the size development is the temperature (i.e.: lower temperatures typically results in the production of smaller particles). This will be discussed in the next chapter.

4 Activation Energy of Magnetite Nanoparticle Growth from Solution

4.1 Background

Crystal growth occurs in a supersaturated solution as soon as nuclei have formed and becomes dominant compared to nucleation when supersaturation drops down (LaMer diagram [54], Figure 4.1).

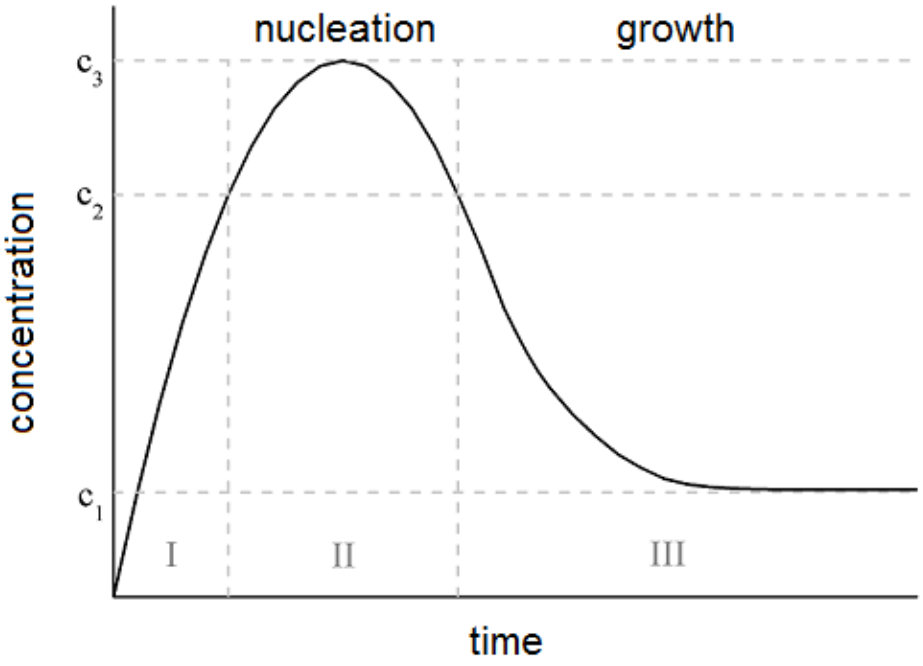

Figure 4.1: LaMer diagram of crystal nucleation and growth from solution with c_1 being the solubility, c_2 being the nucleation/growth border and c_3 being the critical limiting supersaturation. An increasing supersaturation leads to nucleation at the maximum of the peak and further formation of nuclei is active until the concentration drops below c_2. Growth occurs between c_1 and c_2 (III).

The growth of crystals from solution depends on numerous subprocesses:

a) Diffusion of ions or ion-like clusters to the surface of the crystal

b) Adsorption at and diffusion over the crystal surface

c) Dehydration of the ions/clusters at the surface

d) Counter diffusion of solvent released off the crystal

e) Integration of the ions/clusters into the crystal lattice.

The slowest step of the entire process controls the overall rate of growth. The mechanism of growth may either be diffusion-limited (a – d) or reaction-limited (e) and parameters that influence the mechanism are for example the supersaturation, the temperature, the crystal surface or the pH. Very general, particle growth can be described by:

$$\frac{\mathrm{d}R}{\mathrm{d}t} = kR^{1-n} \qquad (4.1)$$

with the particle radius *R*, the time *t*, the growth rate constant *k* and the exponent *n* of the growth law [22], [23]. The growth rate constant is usually a function of the temperature (*k* = f(T)). Integration of Equation (4.1) leads to the general solution:

$$R^n - R_0^n = k * t \qquad (4.2)$$

where R_0 is the radius at t = 0, which can be interpreted as the upper bound of a critical nucleation radius. The exponent *n* depends on the growth mechanism of the crystal growth (*n* = 1, 2, 3 for reaction-limited, diffusion-limited and Ostwald ripening, respectively). It must be mentioned that this classical growth law was developed for crystal growth mediated by ions.

In case of magnetite crystal growth from solution, Baumgartner *et al.* have shown by cryogenic transmission electron microscopy imaging (cryo-TEM) that magnetite can be formed from primary particles (*PP*) [20]. These *PP* are formed from ions or ion-like species (Figure 4.2a), which aggregate to subsequently nucleate (Figure 4.2b) [20]. Furthermore, it was also suggested that the crystal growth is *PP*-mediated (Figure 4.2c). *PP* being attached to the crystal surface were about 1 nm in size, unlike the *PP* in solution, which were 2 nm in size. This shrinkage can be caused by either dissolution and re-precipitation on the crystal surface or dehydration of *PP* followed by attachment to the crystal [20].

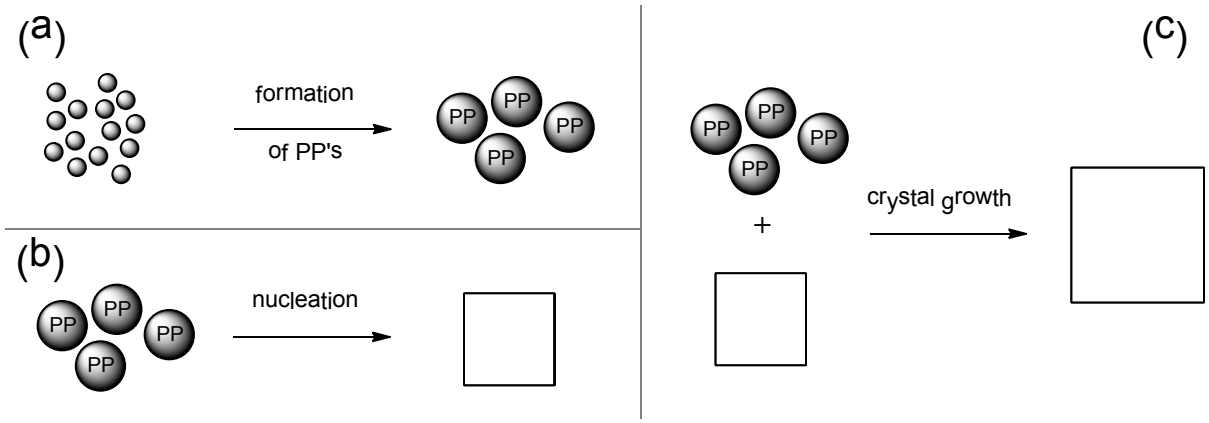

Figure 4.2: Scheme of magnetite nucleation and growth: (a) formation of PP's from ions or ion-like aggregates, (b) nucleation of magnetite from PP's and (c) crystal growth with PP's. At the beginning nucleation is realized via step (a) followed by step (b) and as soon crystals have formed by step (c). The growth reaction suppresses the nucleation quickly as it is energetically favorable and within the observed time range crystals grow exclusively with reactions (a) and (c) taking place simultaneously.

In the same study, it was shown that despite the involvement of primary particles, magnetite nanoparticle growth at room temperature follows the predictions of the kinetic model of the LSW theory. Duue to the observation of linear, self-similar growth it was proposed that the process is reaction-limited.

Activation Energy

Classical rate processes like crystal growth can be described by Boltzmann statistics for which the rate *k* of a process is given by an equation of the form [55]:

$$k = A * e^{\frac{-E_a}{k_B T}} \qquad (4.3)$$

The exponential term is known as the Boltzmann factor with the activation energy E_a (J) the Boltzmann constant k_B = 1.3806 × 10^{-23} J K^{-1} and the absolute temperature T (K). This Boltzmann factor describes the fraction of atoms/molecules/clusters in the system that – at temperature T – exhibits an energy greater than E_a. The pre-factor A (s^{-1}) describes the

frequency of the reaction and is dependent for instance on the geometric details of the path and on atom density. The logarithmic version of Equation (4.3) is:

$$\ln k = \ln A - \frac{E_a}{k_B T} \tag{4.4}$$

If the plot (Arrhenius plot) of ln *k* over T^{-1} results in a straight line it strongly suggests that the mechanism controlling the rate is the same over the whole process. Slope changes or a discontinuous curve would suggest that the mechanism controlling the process changes with changing the temperature. The activation energy in kJ mol^{-1} can be calculated from the slope of the Arrhenius plot:

$$E_a(kJ\ mol^{-1}) = slope * k_B * N_A \tag{4.5}$$

with the Avogadro constant N_A = 6.0221×10^{23} mol^{-1}. The magnitude of activation energies provides mechanistic insights to the process of crystal growth [17].

4.2 Results

Magnetite crystal growth was investigated at five different temperatures (5, 10, 15, 20 and 25 °C) and each synthesis was reproduced in quadruplicates. X-ray diffraction patterns show typical magnetite peaks at every time point (Figure 4.3a) and a closer view of the 311-peak reveals its continuous narrowing (Figure 4.3b). The mean particle diameter was calculated from the Scherrer equation and particle growth was observed over time as shown in Figure 4.3c. Transmission electron microscopy shows typical, highly aggregated magnetite nanoparticles (Figure 4.3d).

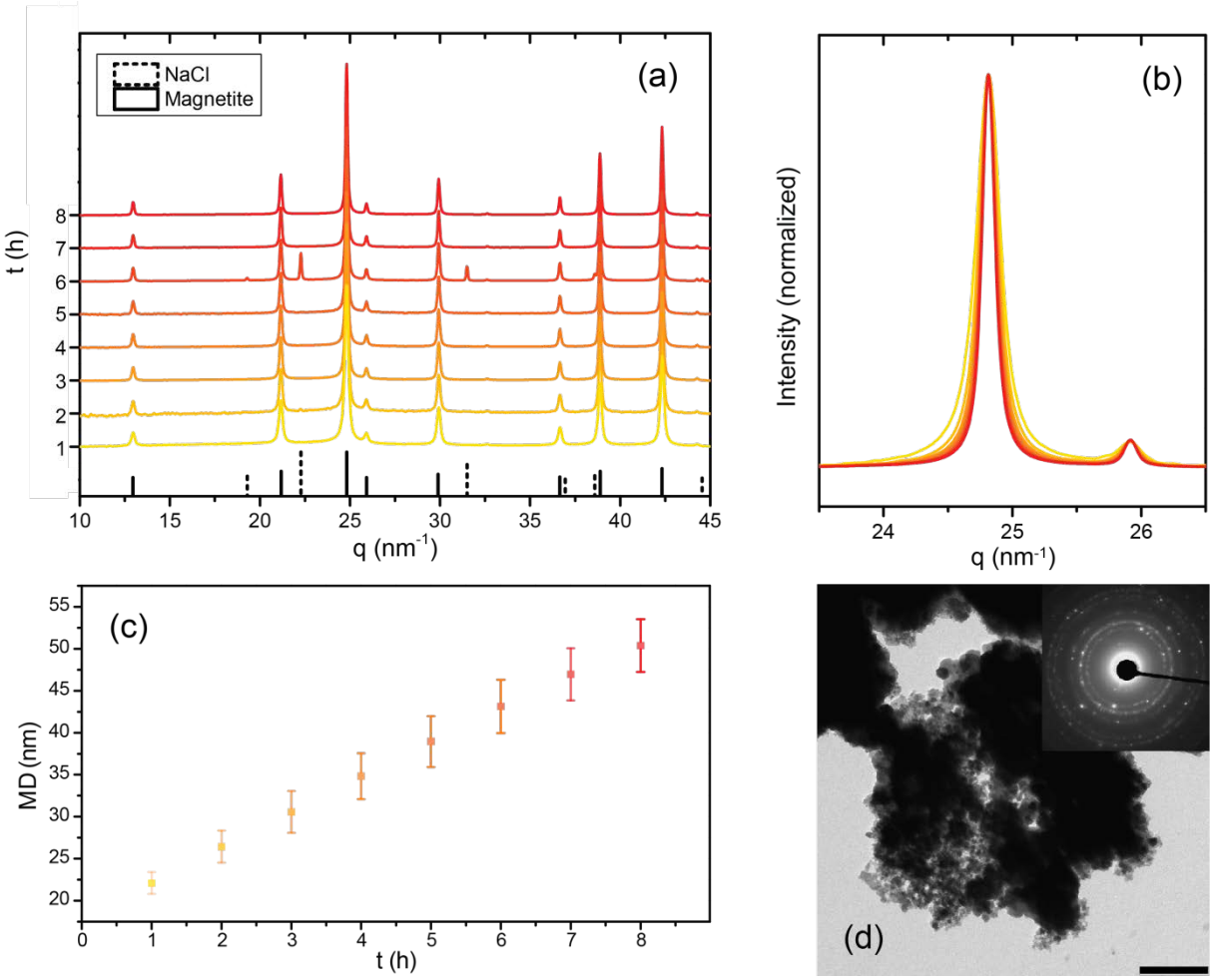

Figure 4.3: Summary of experimental results representative for all samples (a) The XRD diagram shows a typical magnetite pattern at every time point (black solid lines). NaCl (black dotted lines) is sometimes observed besides magnetite. The chronological evolution is indicated by a color scale from yellow (early state) to red (late state). (b) The insight into the 311-peak reveals the decrease of the full width at half maximum. (c) Mean particle diameter over time as an average of all syntheses with standard deviation at 15 °C showing continuous growth and (d) TEM image of one representative sample (scale bar: 200nm) showing highly aggregated nanoparticles of magnetite (inset: SAED pattern with magnetite rings).

Particle growth over time is observed for all temperatures (Figure 4.4, for corresponding values, see Appendix). After eight hours, larger particles are obtained at higher synthesis temperatures and all growth curves show a non-linear, decreasing growth rate over time. Growth curves of each temperature were fitted with Equation (4.2) to calculate the parameters k and MD_0. To determine which rate-limiting process is most consistent with the data, the growth kinetics function was fitted with different, fixed exponents n = 1, 2 and 3. Linear and quadratic exponents yield similar goodness of fit ($R^2 \geq 0.96$ and 0.99, respectively), while n = 3 appears less consistent with our data ($R^2 \geq 0.35$). All obtained values for k, MD_0 and the corresponding adjusted R^2 are presented in the appendix and the

fit curves are shown in Figure 4.4. Rescaling to mastercurves and plotted as MD^n - MD_0^n over *kt* (all five temperatures in one graph) confirms that the quadratic fit is the most consistent (R^2 = 0.99), the linear fit is less consistent (R^2 = 0.98) and the cubic fit is the worst (R^2 = 0.95). Therefore the cubic fit (Ostwald ripening) was excluded from further calculations.

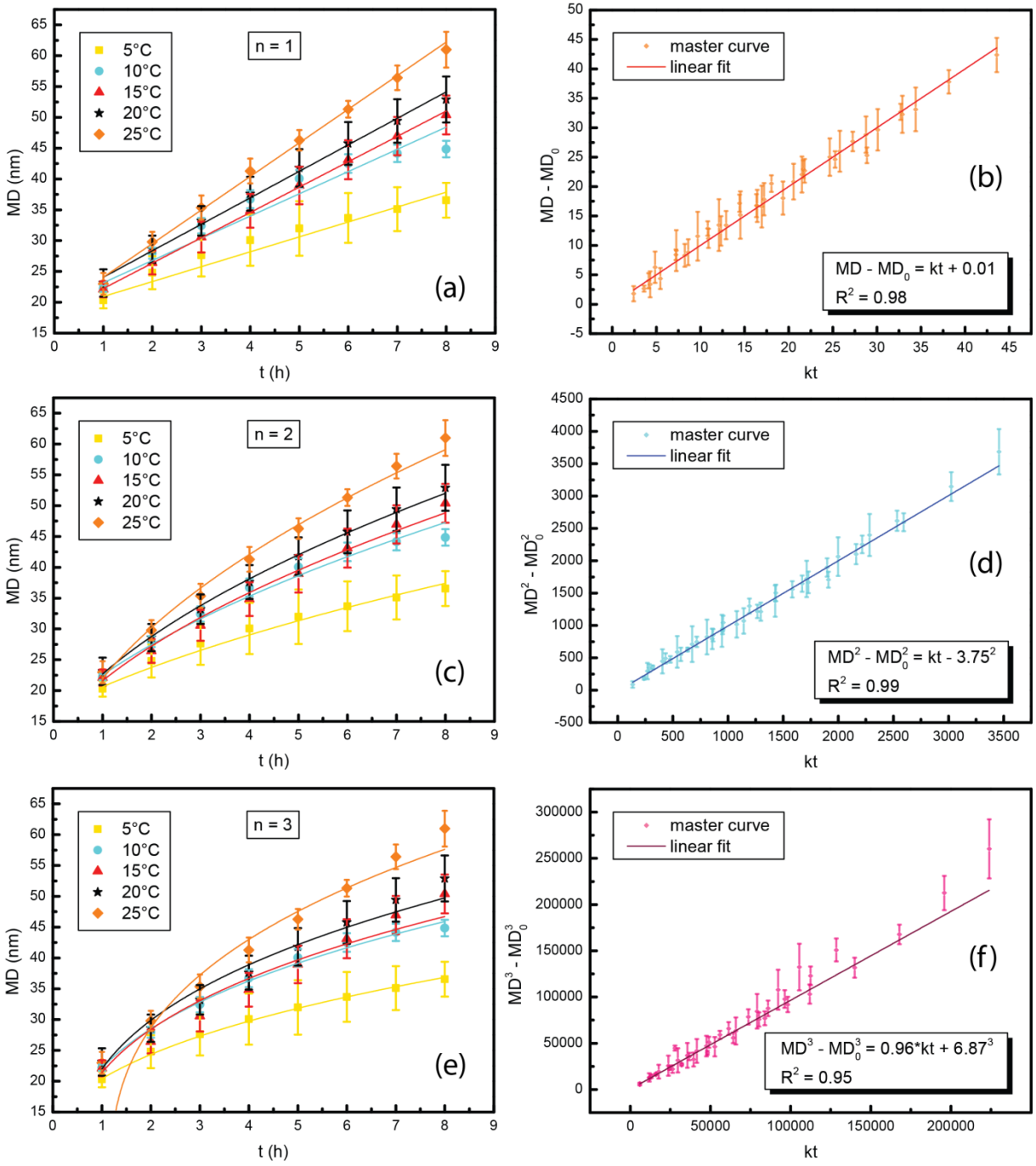

Figure 4.4: (left) The evolution of the mean particle diameter as a function of time for all temperatures (quadruplicates with standard deviation) fitted with $MD^n - MD_0^n = k * t$ and (a) *n* = 1, (c) *n* = 2, (e) *n* = 3. (right) The master curves of (b) *n* = 1, (d) *n* = 2, (f) *n* = 3. All corresponding data are found in the appendix.

The Arrhenius equation was used to investigate the relation between the growth rates k and the temperature. A plot of ln *k* over T^{-1} shows linear dependence for both, the linear and the quadratic fit (Figure 4.5). A linear fit of both graphs resulted in two activation energies, 24 ± 4.4 kJ mol^{-1} and 28.4 ± 5.1 kJ mol^{-1} and two pre-exponential factors, 8.5 x 10^4 h^{-1} and 1.3 x 10^7 h^{-1} for model *n* = 1 and *n* = 2, respectively.

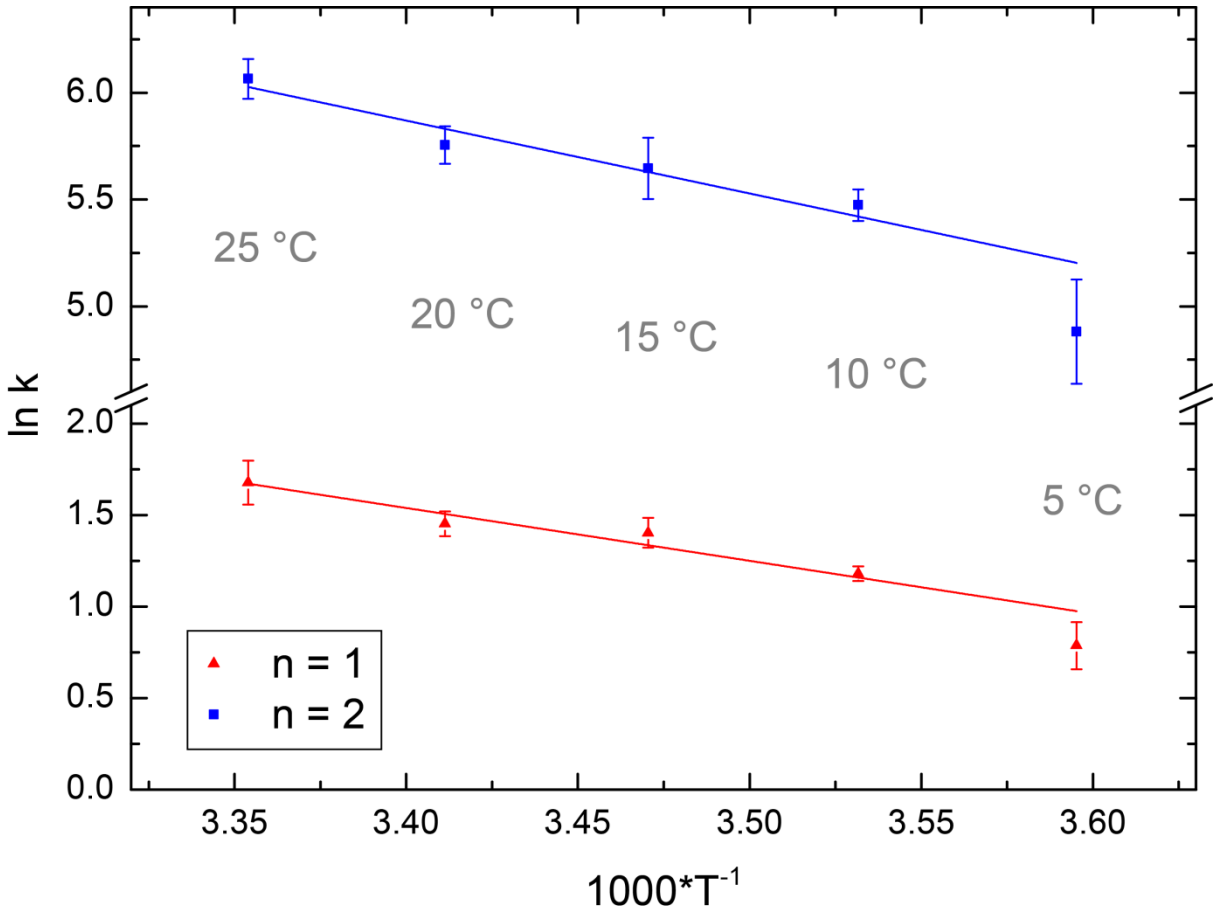

Figure 4.5: Arrhenius plot of *ln k* over *1000*T^{-1}* for the calculation of E_A (standard deviation as error bars) of the linear approach (red graph) and the quadratic approach (blue graph). The lines are the corresponding fits and E_a was calculated from their slope ($ln\ k = ln\ A + \frac{-E_A}{k_B N_A}\frac{1}{T}$).

4.3 Discussion

All possible sub-processes of magnetite growth in our system are taken into account to determine the rate-limiting step. The nucleation step is observed before 1h and is thus not reflected here. The growth process is composed of the formation of PP on the one hand and growth of the crystals at the expense of PP on the other hand. The formation of the PP was

observed quasi-instantaneously [20] and therefore it can be assumed that the energetic barrier of their formation should be low compared to thermal energies and also lower than that of crystal growth (Figure 4.6). Due to the excess of PP, the growth of the crystals is controlled either by diffusion of the PP to the surface or a reaction step, consisting either of PP dehydration and surface integration or a dissolution of PP and re-precipitation as magnetite. In general, reaction rates are more sensitive to temperature changes than diffusion rates.

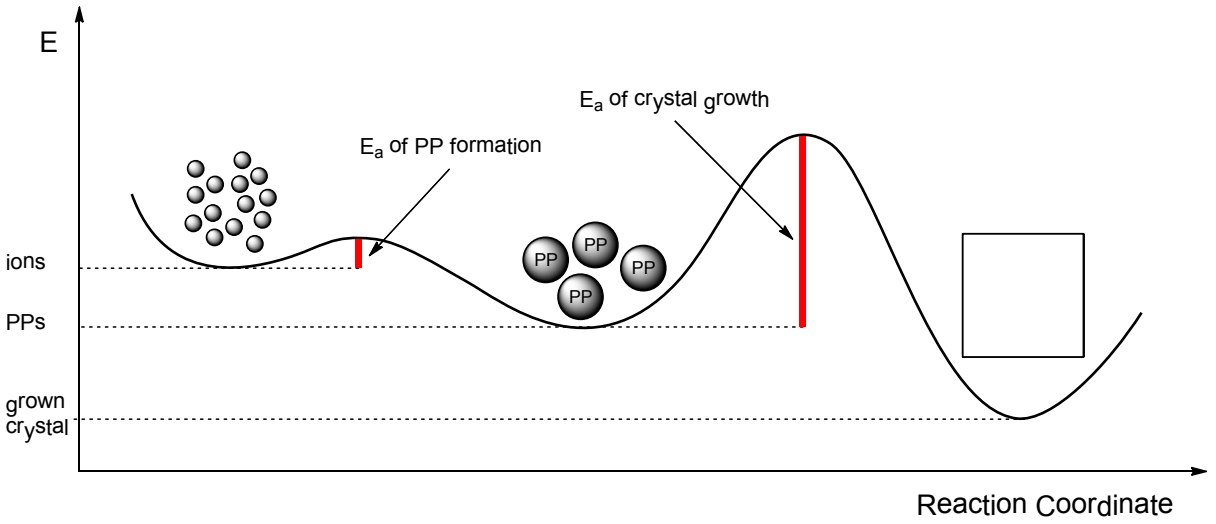

Figure 4.6: The reaction coordinate diagram of crystal growth via two concomitant steps. The formation of primary particles that has a low activation energy and the crystal growth with primary particles that has a comparably higher activation energy.

In consequence, diffusion-controlled processes have lower activation energies than reaction-controlled processes. In this respect, it becomes clear how the calculation of activation energies can help understanding the rate determining step. For diffusion-limited growth E_a < 21 kJ mol^{-1}, if only ionic species are involved in the accretion [17]. For reaction-limited crystal growth E_A is 40 – 80 kJ mol^{-1} if the process is based on the addition of ions [17]. If pre-nucleation clusters/primary particles are involved the activation energy usually increases. Diffusion becomes energetically more demanding due to a large number of atoms being involved in translational and rotational motion of nm-sized particles (E_a > 21 kJ mol^{-1}). Nanogoethite formation via oriented attachment resulted in activation energies of 23 kJ mol^{-1} (nitrate system) and 45.2 kJ mol^{-1} (sulfate system) [26]. In their work, Vu *et al.* suggest

a growth that is controlled by nanoparticle diffusion. In addition, they suggested that the difference between the nitrate and the sulfate system might originate from the different ionic charge of the counter ions. Mobility is lower in a solution with higher charged ions (NO_3^- compared to SO_4^{2-}). Surface reaction-limited processes become energetically more demanding, because of the large number of atoms being integrated into the crystal surface simultaneously. Oriented attachment of ZnS via nanoparticles lead to activation energies of 137 and 125 kJ mol^{-1}, with or without presence of mercaptoethanol, respectively [25].

The activation energy E_a is 24 kJ mol^{-1} for n = 1, which is clearly below the range of reaction-controlled growth. This is in contradiction with the initial assumption of a reaction-limited process [20]. Furthermore, we obtained the best fitting results for the quadratic fit quantified by the adjusted R^2-parameter, indicating that the quadratic approach is more accurate. The activation energy E_a is 28.4 kJ mol^{-1} for n = 2, which is above that of ionic diffusion-limited growth (E_a < 20 kJ mol^{-1}) but as mentioned before, nanoparticulate precursors increase the activation energy. This is in good agreement with former results, where the involvement of primary particles in the magnetite growth process was shown [20].

5 Alteration of Magnetite Nanoparticles

The alteration of magnetite nanoparticles was the subject of a study already published and from which this chapter is mainly inspired [47].

In chapter 3 “Formation of Stable Single Domain Magnetite Nanoparticles at Low Temperature” typical features of magnetite nanoparticles were already presented by using XRD, TEM and magnetic measurements. Here the development of these features was investigated to gain insights into possible alteration processes occurring during long term storage of MNP. A set of four samples was subjected to six analyses and four different storage conditions (-20°C, 4 °C, a.t. and a.t. + Ar) over a time range of 18 months.

5.1 Background

5.1.1 Crystal Structure and Magnetic Properties of Magnetite, Maghemite and Hematite

The crystal structure of iron oxides is governed by the arrangement of the anions, the oxygen ions due to their larger ion radius (ionic radii: $r(O^{2-}) = 0.14$ nm, $r(Fe^{II}) = 0.082$ nm, $r(Fe^{III}) = 0.065$ nm). As a consequence, topological interconversion often occurs between different iron oxides [3]. Oxidation of magnetite to maghemite is only one example; both have very similar crystal structures and thus exhibit similar magnetic properties [3].

Magnetite

Magnetite has a face-centered cubic unit cell, which contains 32 O^{2-} ions, which are cubic close packed along the (111)-direction. The O^{2-} ions are ABCABC stacked and the iron ions are positioned in the tetrahedral and octahedral sites between the oxygen ions. Magnetite crystallizes in the inverse spinel structure, 8 of the tetrahedral positions are filled with Fe^{3+}-ions. Half of the octahedral sites are filled with 8 Fe^{3+}-ions and the other half with 8 Fe^{2+}-ions. The unit cell of magnetite has a lattice parameter (which is equal to the unit cell length) of a = 0.83969 nm. Figure 5.1 shows a scheme of one unit cell of magnetite containing altogether 8 formula units of Fe_3O_4, the charge of 32 O^{2-} ions is compensated by totally 24 iron ions (8 Fe^{2+} ions and 16 Fe^{3+} ions).

Magnetite is ferrimagnetic at room temperature, with a Curie temperature at T = 850 K [3]. The tetrahedrally and octahedrally bound iron ions can be seen as two different sublattices with antiparallel arrangement of the magnetic moments. Ferrimagnetism is a consequence of different net values of the two antiparallel magnetic moments. This is the case for bulk phases; below a material-specific size the particles become superparamagnetic also below the Curie temperature. For sufficiently small enough particles thermal energies cause changes of the of magnetization directions. Magnetite nanoparticles are superparamagnetic at a size below 20 – 30 nm. Beyond this threshold, one single and stable magnetic domain is formed and the direction of magnetization remains stable [10]. Depending on the morphology, the particle reaches the multi-domain state at different size. Elongated particles show stable single domain behavior up to a length of 4 µm and isotropic particles up to a mean particle diameter of $MD \sim 100$ nm [10].

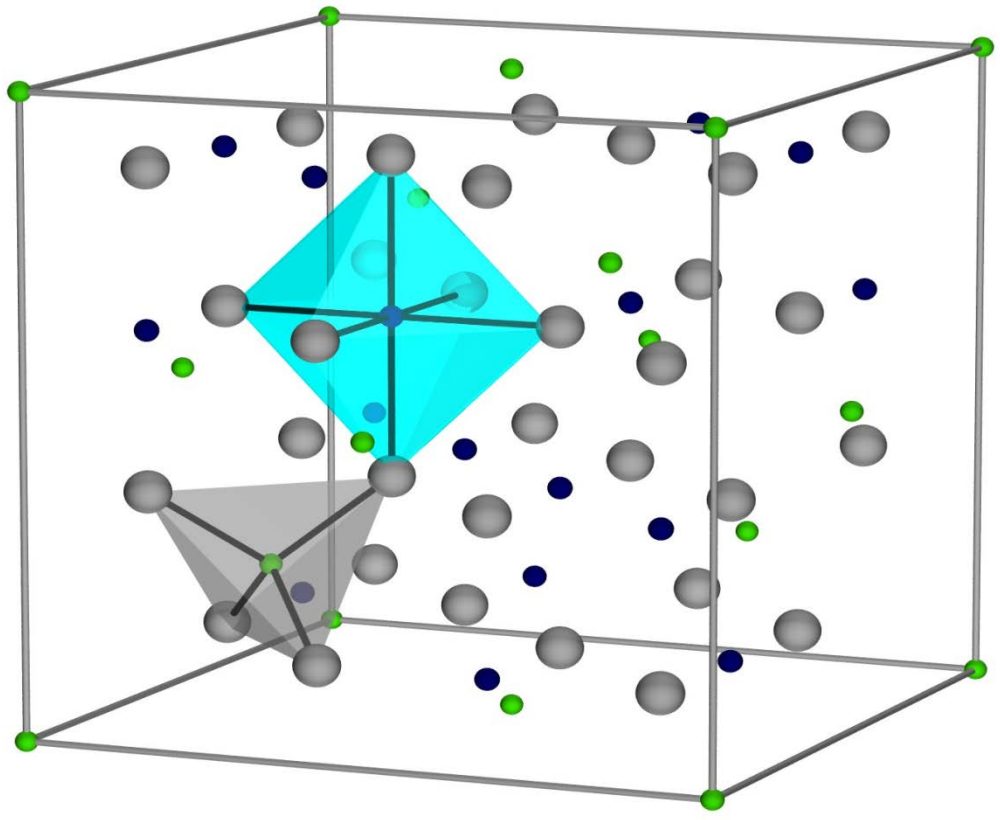

Figure 5.1: A unit cell of magnetite; the green spheres represent the iron in tetrahedral sites, the blue spheres are the octahedrally bound iron ions and the grey spheres are the oxygen ions (Copyright 2011 by David Schrupp).

Maghemite

Maghemite has a very similar crystal structure to magnetite. The oxygen is cubic closely packed along the (111)-direction and ABAB stacked. In contrast to magnetite, it contains 32 O^{2-} ions and $21\frac{1}{3}$ Fe^{III} ions. The higher net charge of the Fe cations in maghemite results in less Fe ions per unit cell but at the same time the same number of oxygen. This causes vacancies in the crystal lattice. Whereas the Fe ions are randomly distributed over the 8 tetrahedral and 16 octahedral sites, the $2\frac{2}{3}$ vacancies are confined to the octahedral sites. Due to these vacancies, maghemite crystallizes in a defect inverse spinel structure and has a lattice parameter *a* = 0.83419 nm, slightly smaller than magnetite.

Maghemite also has two antiparallel sublattices with a net magnetic moment unequal to zero and is, hence, also ferrimagnetic. The change in the crystal lattice causes a small decrease in the saturation magnetization compared to magnetite but it is often difficult to distinguish the two minerals based on their magnetic properties [3], [7].

Hematite

Another iron oxide that will be part of the alteration study is Hematite (α-Fe_2O_3), which is the most thermodynamically stable iron oxide phase under ambient conditions. Hematite has a hexagonal unit cell with two lattice parameters a = 0.5034 nm and c = 1.3752 nm. Oxygen is hexagonal close packed along the (001)-direction and ABAB stacked. Octahedral sites are regularly filled with Fe^{III} ions (two filled sites, one vacant site, etc.). One unit cell consists of six formula units. Although the Fe^{III} ions are antiferromagnetically arranged, hematite is weakly ferromagnetic at room temperature due to spin canting. Therefore it is magnetically distinguishable from magnetite and maghemite [3]. In particular, there will be an increase in H_C and H_{CR} due to the higher coercivity of hematite and a decrease in M_{RS} and M_S due to its lower saturation magnetization.

5.1.2 Transformational Processes

At room temperature, magnetite is topotactically oxidized to maghemite so that the crystal morphology is maintained [56]. A mixed phase of

$Fe(II)_{1-x}Fe(III)_{2+x}O_{4+0.5x}$ with growing x is formed and being further oxidized [57]. The oxidation to maghemite causes a reduction in the number of Fe ions per unit cell (24 $Fe^{II/III} \rightarrow 21\frac{1}{3}\,Fe^{III}$) and the reaction proceed via outward migration of Fe ions to the crystal surface, accompanied by vacancy formation. Fe ions are oxidized at the surface and a layer of maghemite forms around the magnetite.

Further transformation to hematite is accompanied by structural changes and usually requires temperatures above 300 °C. Although has been shown by Colombo *et al*. that lattice imperfections can lead to partial hematite formation [58] even at reduced temperatures. Stacking faults in the inverse spinel structures can behave like nuclei of hematite and this process favorably appears for larger particles due to higher lattice strain.

5.1.3 Oxidation Parameter z

Now an oxidation parameter *z* is introduced, which is calculated with the help of the lattice parameter and that reflects the ratio of material that was oxidized to maghemite and material that is still magnetite. At the beginning or for an ideal magnetite powder the lattice parameter $a = a_{magnetite}$, but as soon as the material is exposed to environmental conditions, in especially to oxygen, oxidation to maghemite occurs. Full oxidation would result in a lattice parameter $a = a_{maghemite}$. Assuming a mixture of magnetite and maghemite the lattice parameter will be somewhere between both. With $a_{maghemite} < a_{experimental} < a_{magnetite}$ the oxidation parameter *z* is defined by Equation (5.1), with $z_{magnetite} = 0$, $z_{maghemite} = 1$ and $1 > z_{experimental} > 0$. With Equation (5.2) oxidation can be calculated on a percentage basis.

$$z = \frac{a_{magnetite} - a_{experimental}}{a_{magnetite} - a_{maghemite}} \tag{5.1}$$

$$Oxidation\ (\%)\ =\ z * 100\% \tag{5.2}$$

This oxidation parameter can be used for introducing an idealized oxidation model that can be applied to the samples (Figure 5.2). This model is based on a core-shell-structure like it was described for example by Frison et al. for magnetite-maghemite nanoparticles in the 5 –

15 nm range [59]. Assuming a spherical, isotropical shape for the particles, oxidation starts at the surface so that a thin layer of maghemite is obtained around a core of magnetite. A transformation from magnetite to maghemite accompanies with the decrease of iron ions of one unit cell from 24 in magnetite (8 Fe^{II} and 16 Fe^{III} ions) to 21.33 Fe^{III} ions in maghemite. This is realized by outward migration of Fe ions – whereby cation vacancies are created in the crystal lattice – and their oxidation at the surface [3]. Due to the migration the maghemite layer is growing inwards and the magnetite core is simultaneously shrinking. In small particles complete oxidation can be achieved due to short diffusion distances but large crystals have too long diffusion distances so that oxidation usually stops before being completed. To completely oxidize large particles temperatures above 500 °C are necessary [3]. The conditions chosen are far below this and this is why complete oxidation is not reached for all samples. From the thermodynamic point of view hematite is the most stable iron oxide and after oxidation to maghemite the samples are not automatically stable. But to further transform maghemite to hematite temperatures above 300 °C are needed and this is far above the chosen conditions.

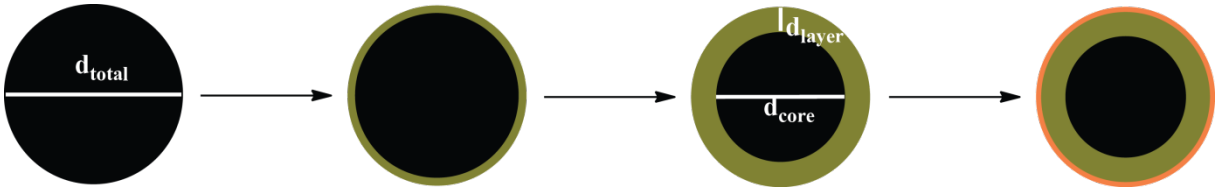

Figure 5.2: Oxidation model for the path from magnetite (black) to maghemite (dark yellow) and hematite (orange); a magnetite sphere is partially oxidized on the surface and the growth proceeds inwards at the expense of the magnetite core; a possible transformation of maghemite to hematite could take place on the surface.

The core diameter d_{core} and the layer thickness d_{layer} can be calculated from the oxidation parameter z and the mean particle diameter d_{total}, as shown in Equations (5.3) – (5.6). The mean particle diameter is assumed to be constant over the entire experiment and is set to the initial value.

$$V_{core} = (1-z)V_{total} \quad with \quad V = \frac{1}{6}\pi d^3 \tag{5.3}$$

$$d_{core} = \sqrt[3]{(1-z)d_{total}^3} \tag{5.4}$$

$$V_{layer} = V_{total} - V_{core} = zV_{total} \tag{5.5}$$

$$d_{layer} = \frac{1}{2}(d_{total} - d_{core}) = \frac{1}{2}(d_{total} - \sqrt[3]{(1-z)d_{total}^3}) \tag{5.6}$$

5.2 Results

5.2.1 The Initial Stage

Table 5.1 shows all important parameters that were taken into account at the initial stage. The mean particle diameter ($d_{initial}$ in this alteration chapter), M_S, M_{RS} and H_C were already presented and discussed in chapter 3. Both suggest particles in the magnetic stable single domain range for the four analyzed samples. But the size distribution is broad and particles of superparamagnetic and multi-domain size may be included. It was not possible to determine the size distribution more precisely due to high aggregation of particles in this size range (Figure 3.1). Based on earlier results it can be assumed that growth under given conditions results in self-similar particle size distributions [20]. Furthermore, the lattice parameter "*a*" was calculated from the (311) peak and initially all samples have a lattice parameter $a_{average}$ = 0.8395 ± 0.0005 nm, which is close to that of magnetite ($a_{magnetite}$ = 0.83969 nm)

Saturation magnetization is in the range of magnetite (92 A m^2 kg^{-1} [60]). The sample with the smallest mean particle diameter has the lowest saturation magnetization ($M_{S,sample\ 124}$ = 75.29 A m^2 kg^{-1}), which would be expected if some oxidation to maghemite or hematite has already occurred. $M_{S,sample\ 125}$ = 105.5 A m^2 kg^{-1}, which may suggest the presence of another reduced iron species since the measured lattice parameter is also larger than for pure stoichiometric magnetite. A variation in particle size distribution and also in aggregation may also cause differences in magnetic properties e.g. a stronger aggregation depresses M_{RS}. Here the remanent coercivity (H_{CR}) was taken into account to calculate the ratio of H_{CR}/H_C. Both, the coercivity and the remanent coercivity vary due to size variations but the ratio

(H_{CR}/H_C) is independent of size but a reliable factor to estimate possible oxidation. The isothermal remanent magnetization is saturated between 200 – 230 mT for all samples (Figure 3.3b).

Table 5.1: Particle size and magnetic properties of initial samples (saturation magnetization (M_s), saturation remanent magnetization (M_{RS}), coercivity (H_C) and coercivity of the remanence (H_{CR}).

Sample	**121**	**123**	**124**	**125**
Mean particle diameter ($d_{initial}$) (nm)	63	52	33	50
Size distribution (nm)	10 – 300	10 – 100	10 – 100	10 – 90
Lattice parameter (a) (nm)	0,83937	0,83993	0,83883	0,83972
M_S (A m^2 kg^{-1})	87.2	83.81	75.29	105.5
M_{RS} (A m^2 kg^{-1})	13.4	15.22	8.81	17.61
M_{RS}/M_S	0.15	0.18	0.12	0.17
H_C (mT)	8.6	10.4	6.2	9.9
H_{CR} (mT)	17.6	17.8	12.0	17.7
H_{CR}/H_C	2.0	1.7	1.9	1.8

5.2.2 Structural Evolution

We obtained typical magnetite/maghemite patterns over the entire range of time and there is no indication that other iron oxide structures were formed (Figure 5.3a). Apart from magnetite/maghemite, NaCl (side product of the synthesis) and a α-quartz (additive as part of the analysis method) are present. A closer look to the (311)-peak reveals a continuous shift towards higher q-values (Figure 5.3b).

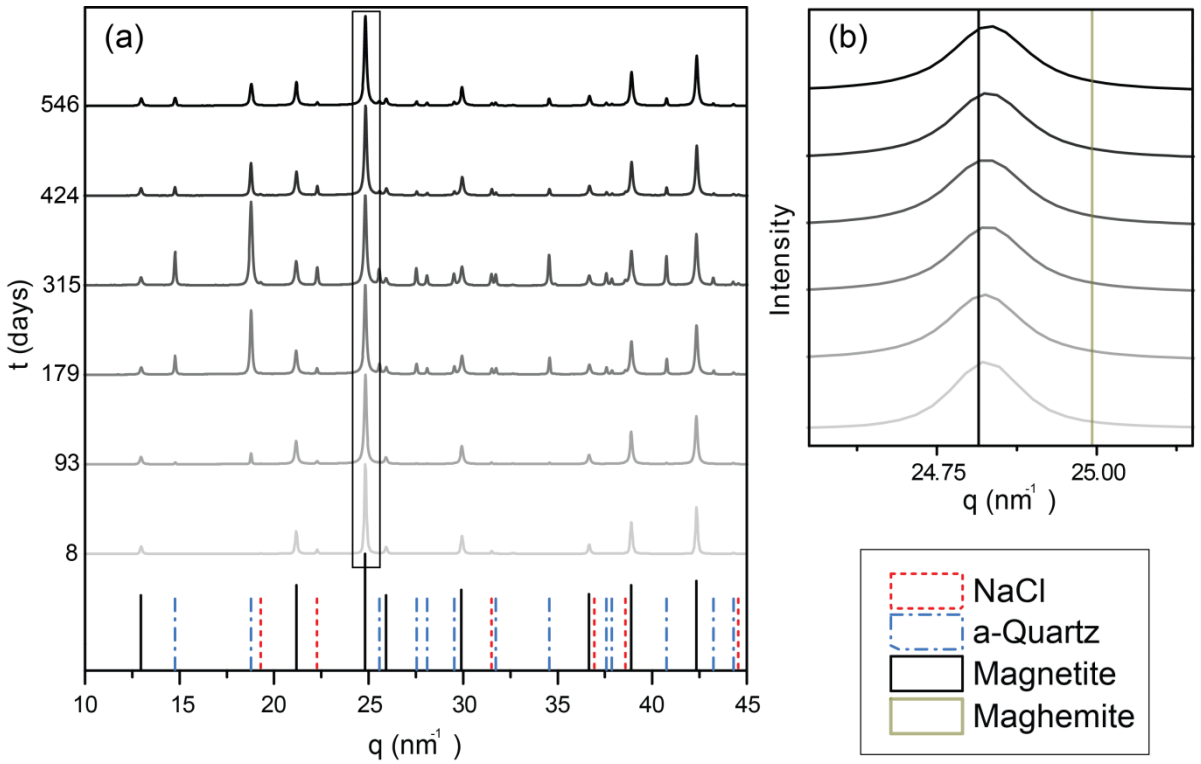

Figure 5.3: X-ray diffraction diagram for the sample 121 at the different stages of the alteration study with (b) expanded view on the (311) peak. With time there is a shift of the peak towards higher values (light grey to black ≙ initial state to final state).

TEM investigation shows highly aggregated nanoparticles of crystalline magnetite/maghemite (Figure 5.4a). Both, the particle size and the morphology appear to be the same as in the initial stage. Furthermore, sphere-like structures are present in all samples (Figure 5.4b). They are polycrystalline but do not contain other iron oxide phases.

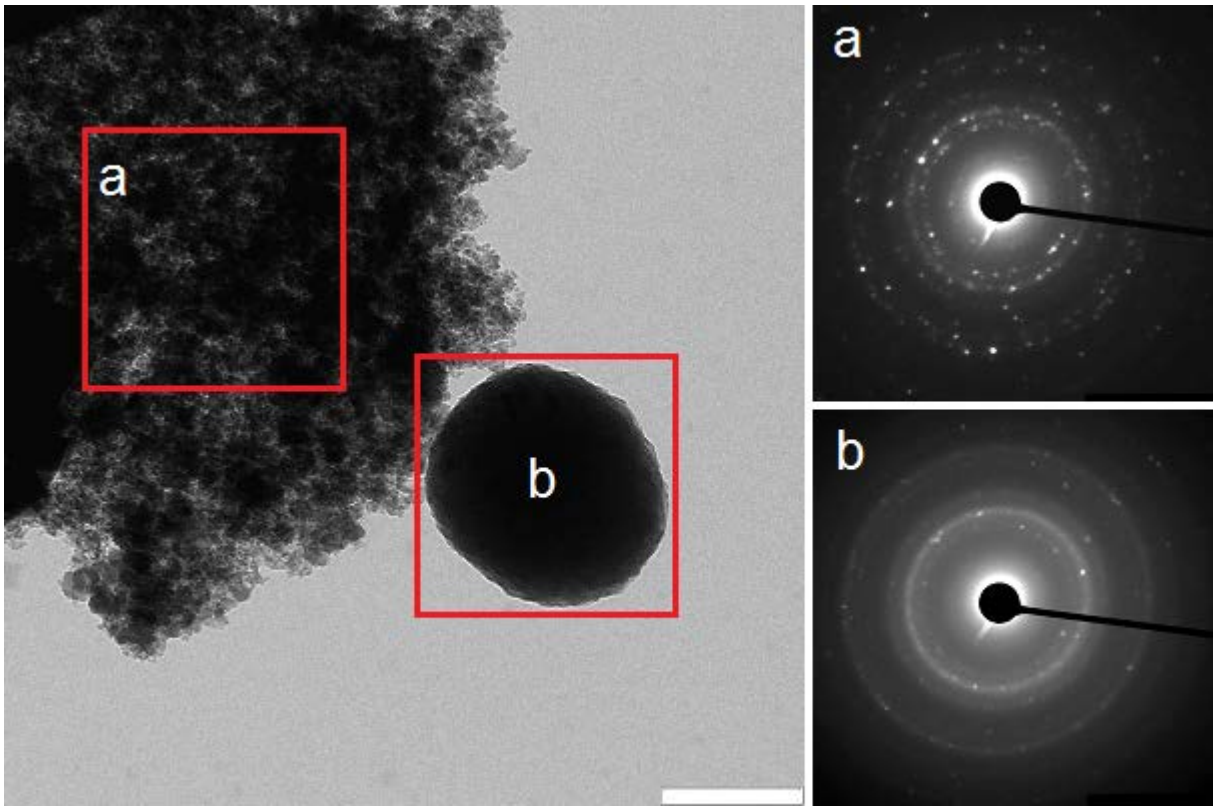

Figure 5.4: Transmission electron micrographs of the final state of sample 121 show aggregated nanoparticles of crystalline magnetite (a, b) similar to the initial stage. Additionally we see large sphere-like structures in every sample, which consist of polycrystalline magnetite (a).

High-resolution TEM revealed the presence of other iron oxide phases being located at the surface of the particles. Extra periodicity and the corresponding Fourier Transform indicates the presence of feroxyhyte (δ-FeOOH, Figure 5.5a) similar to a study of Rečnik et al. [61], where they investigated the effect of thermal treatment on magnetite and, except for the bulk oxidation to maghemite they identified the formation of a few-nm-thick layer of feroxyhyte (δ-FeOOH) covering the maghemite crystals. Furthermore, there are superperiodicity reflections (Figure 5.5b, encircled), which are halfway between the magnetite reflections indicating the presence of vacancy-ordered maghemite structures. A summary of TEM results for all samples at the initial and final stage is presented in the Appendix.

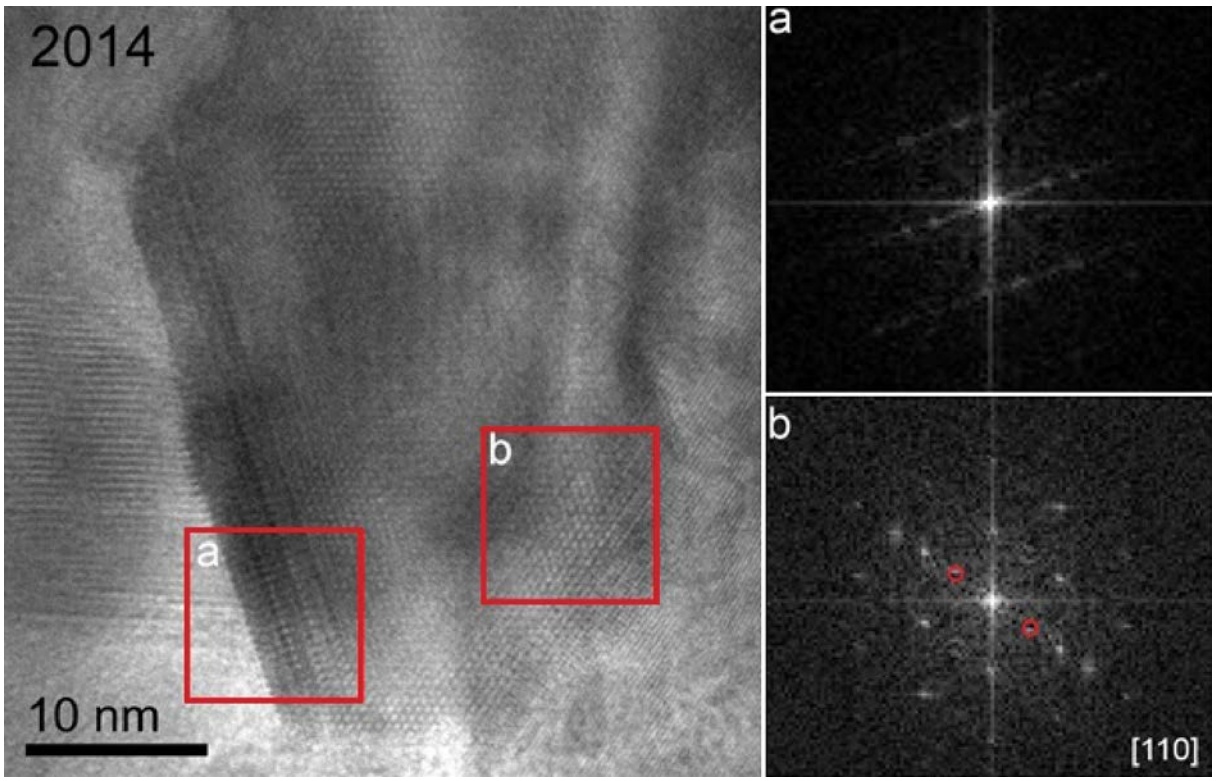

Figure 5.5: The High-resolution image of a particle in sample 121 confirms the crystalline structure of the magnetite nanoparticles. The marked area (a) shows extra periodicity and the corresponding Fourier-transform shows an almost continuous streak along the direction that is perpendicular to the surface of the crystal. In the marked area (b) superperiodicity is apparent and confirmed by reflections in the corresponding Fourier-transform (encircled) that are halfway between the magnetite reflections. Adapted with permission from Mihály Pósfai.

Initially the lattice parameter of all samples was $a_{average}$ = 0.8395 ± 0.0005 nm. A decrease over time was observed for all samples and all storage conditions (Figure 5.6). More specifically, the samples stored in the freezer have bigger lattice parameters (closer to magnetite) compared to those stored in the fridge and the samples stored at room temperature have the smallest lattice parameters. In addition, the samples flushed with argon and sealed with Parafilm did not show a different behavior than the sample stored in air.

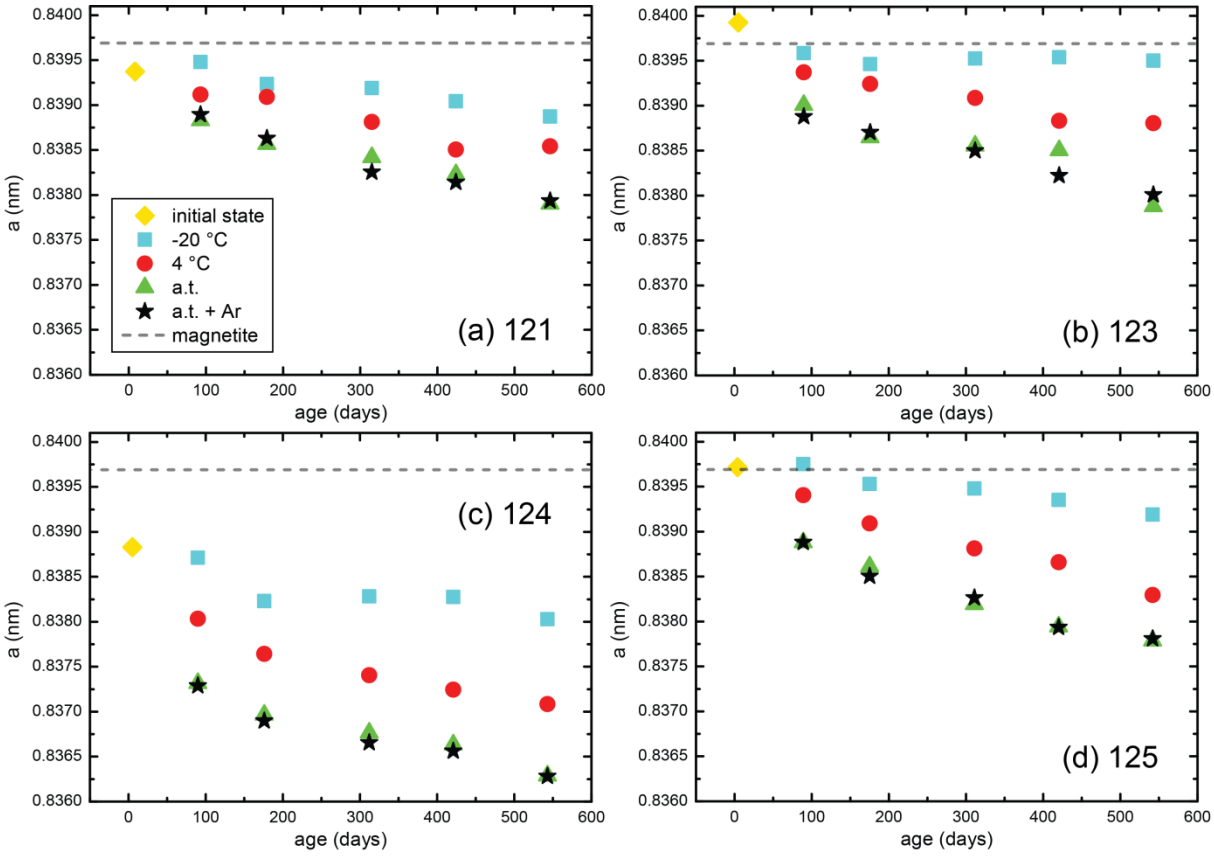

Figure 5.6: Plot of the lattice parameter *a* over time for all samples and all storage conditions (initial state by yellow diamond, -20 °C by blue squares, 4 °C by red circles, a.t. by green triangles and a.t. + Ar by black stars).

In Figure 5.7, the lattice parameter is again plotted over time but arranged in a way that the four samples for one storage condition are in one diagram. This is to show that the size of the sample also plays an important role in the alteration. Sample 124 with d_{total} = 33 nm oxidizes more readily indicated by smaller values for the lattice parameter compared to the other three samples, which have a diameter of 50 to 63 nm. Interestingly, these three samples with different sizes show very similar behavior in lattice parameter alteration. This indicates that there is a threshold for the particle size meaning that from a certain size on (between 33 and 50 nm) the size does not play a role anymore.

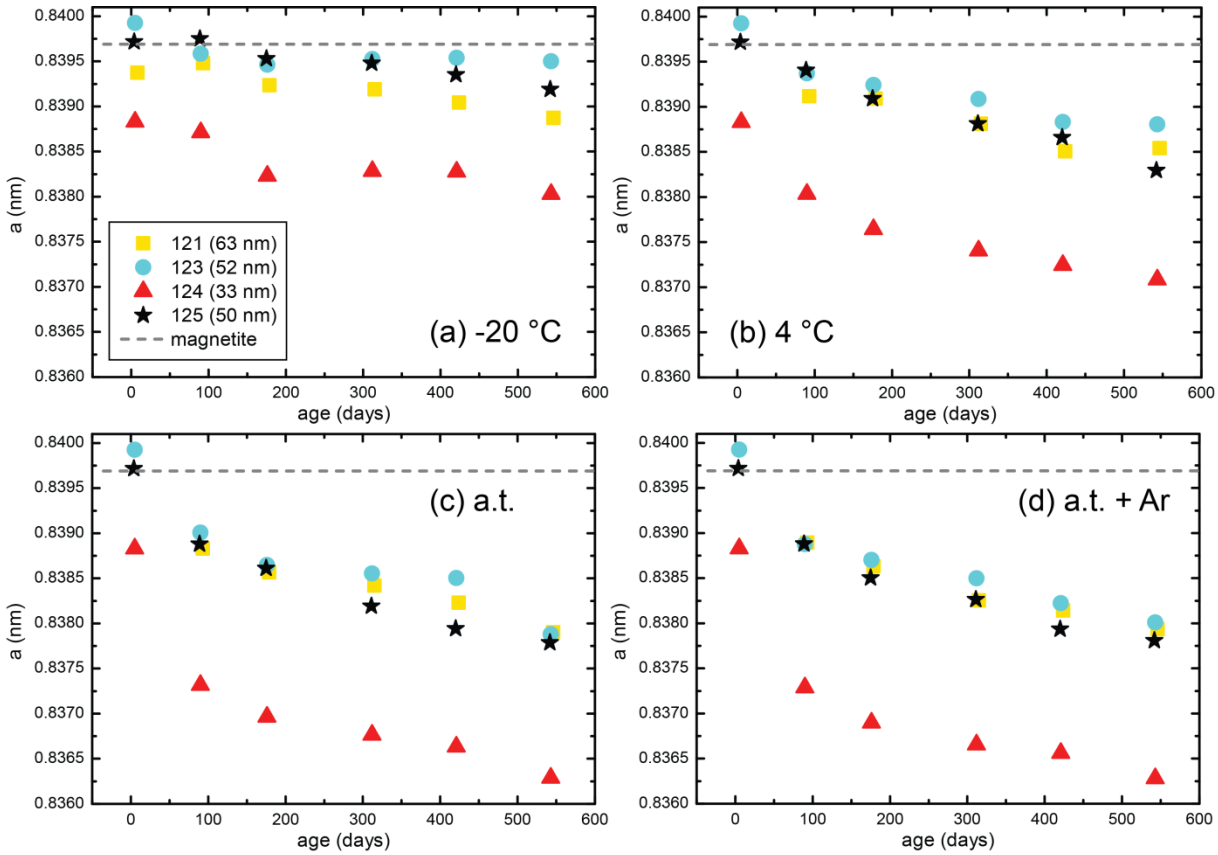

Figure 5.7: Plot of the lattice parameter *a* over time for all different storage conditions and all samples

The oxidation parameter *z* was calculated for all samples and given storage conditions. Sample 121 was taken as an example with an initial value of $z_{121,initial}$ = 0.0575, which is equal to an oxidation of 5.75%. After 18 months the degree of oxidation increases to 15 % in the freezer, 21 % in the fridge and 32 % for particles stored under ambient conditions. The complete data set for all samples can be found in the Appendix. According to the core-shell-model, the evolution of the maghemite layer is presented and for all storage conditions d_{layer} is plotted over time for all samples (Figure 5.8). For sample 121, we have an initial maghemite layer of 0.62 nm, which is about 2 % of the particle radius (r_{total} = 31.5 nm). After 18 months the maghemite layer increases to 1.64 nm when stored in the freezer, 2.37 nm in the fridge and 3.83 nm for particles stored under ambient conditions (for complete data set, see Appendix). Similar to the development of the lattice parameter, where small particles oxidize faster than large ones in any condition, thicker maghemite layers are observed for small particles and thinner layers for larger particles. Non-linear growth is observed for particles stored at 4 °C and under ambient conditions. In solid phases diffusion is significantly slower than in a gaseous or liquid phase, so that that the outward migration/diffusion of the

Fe^{II}-ions could be the rate limiting step. Oxidation is fastest in the first 100 – 200 days of storage independent of the particle size for samples stored at room temperature or in the fridge. The amount of oxidation in the samples subsequently increases more slowly. The particles stored at -20 °C show nearly linear growth of the oxidated layer. In general, smaller particles oxidize faster at the beginning but at some point they reach the same rate of oxidation as the larger particles.

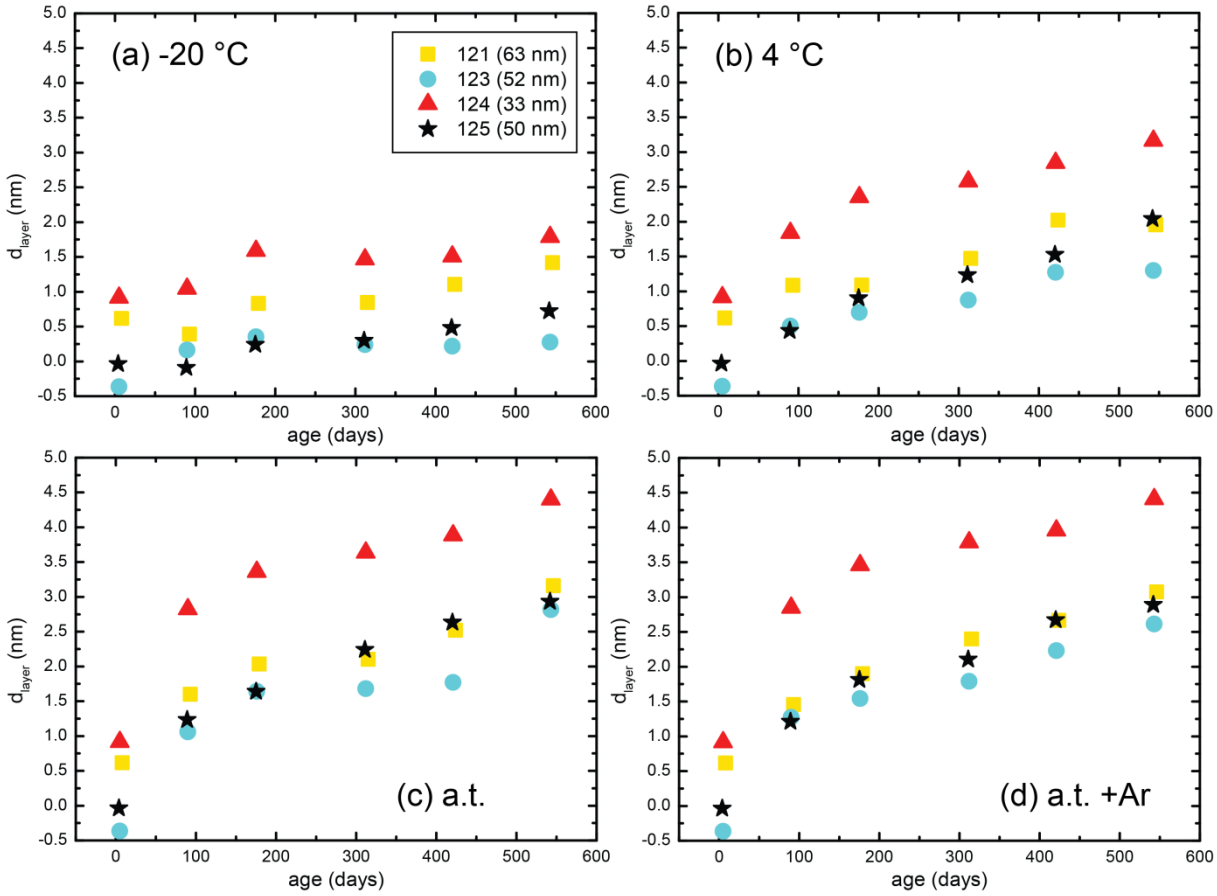

Figure 5.8: The evolution of the maghemite layer at -20 °C (a), 4 °C (b), a.t. (c) and a.t. + Ar (d) for the samples 121 (yellow squares, d_{total} = 63 nm), 123 (blue circles, d_{total} = 52 nm), 124 (red triangles, d_{total} = 33 nm) and 125 (black stars, d_{total} = 50 nm).

Furthermore, a peak broadening is observed (Figure 5.9). The peak width increased during the first three measurements for all four samples and storage conditions and stayed constant at the later three measurements. Particle shrinkage might be the reason but is not necessarily the case. More details will be shown in the discussion section.

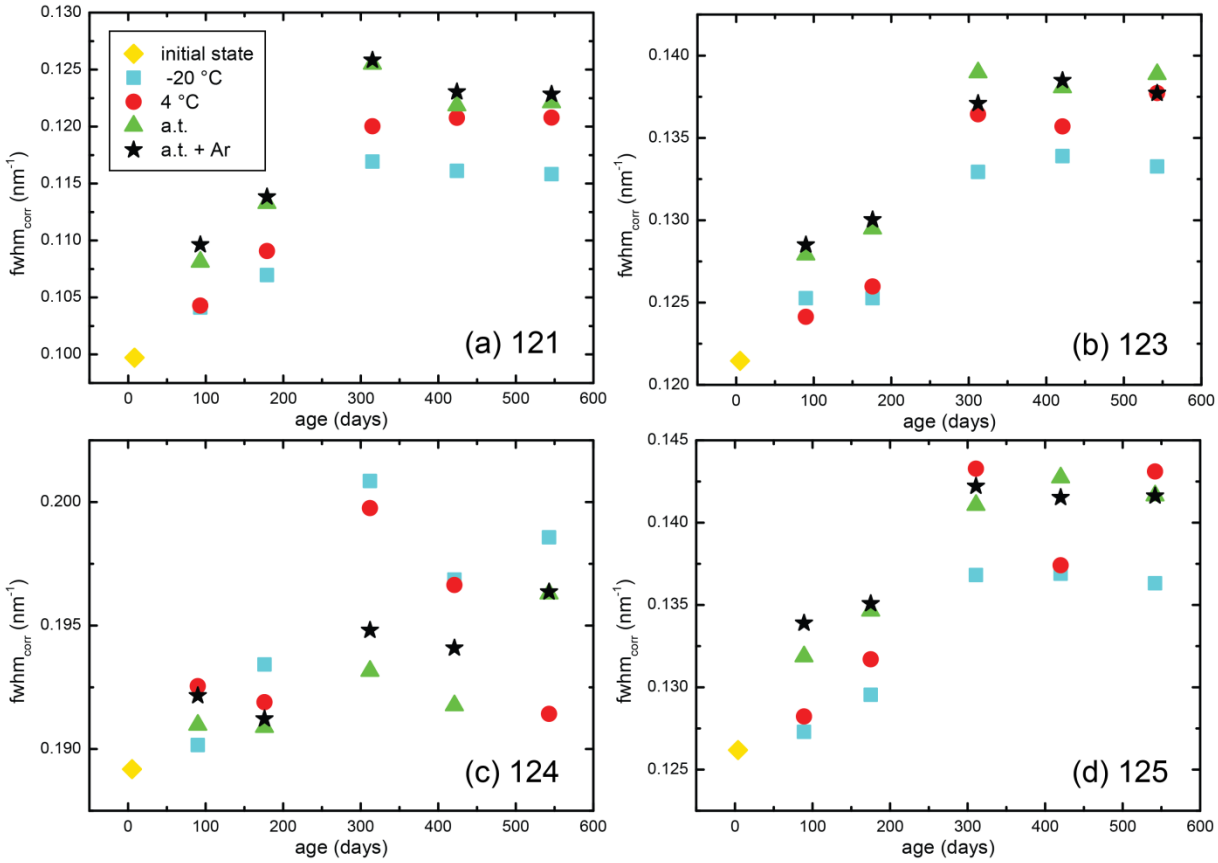

Figure 5.9: Plot of the instrumental-peakbroadening-corrected full width at half maximum ($fwhm_{corr}$) over time for all samples and all storage conditions (initial state by yellow diamond, -20 °C by blue squares, 4 °C by red circles, a.t. by green triangles and a.t. + Ar by black stars).

5.2.3 Evolution of Magnetic Properties

The hysteresis loops and the isothermal remanent magnetization are shown in Figure 5.10 for all samples at the initial stage and after 18 months and the magnetic parameters are listed Table 5.2. The ratios of magnetization (M_{rs}/M_s) and coercivity (H_{cr}/H_c) are sensitive in detecting surface oxidation as the magnetite is being oxidized to another magnetically less active iron oxide. In this case, decrease of M_{rs}/M_s and increase of H_{cr}/H_c indicate alteration of the surface. In terms of magnetic properties magnetite and maghemite are very similar and hence conversion of a small amount of magnetite to maghemite due to oxidation is difficult to identify. However, oxidation/transformation from magnetite/maghemite to hematite can easily be seen as hematite is paramagnetic at room temperature. Results show that the samples stored under ambient conditions or in the fridge are very similar in their magnetic properties. The largest alterations are observed for samples that were stored in the freezer. For the Samples 121 and 124 M_{rs}/M_s is smaller for particles stored in the freezer compared

to storage under ambient conditions. Furthermore sample 121 shows differences in H_{cr}/H_c – particles after storage in the freezer have a bigger ratio than the other storage conditions – and the IRM is not saturated in the maximum of the applied field (Figure 5.10b).

Table 5.2: Summary of magnetic parameters for all samples under different storage conditions initially and after 18 months.

Sample	M_{RS}/M_S	H_{CR}/H_C	Sample	M_{RS}/M_S	H_{CR}/H_C
121			**123**		
Initial	0.15	2	Initial	0.18	1.7
-20 °C	0.12	**3.2**	-20 °C	0.18	1.9
4 °C	0.2	1.8	4 °C	0.23	1.7
a.t.	0.16	1.9	a.t.	0.21	1.8
a.t. + Ar	0.19	1.9	a.t. + Ar	0.24	1.6
124			**125**		
Initial	0.12	1.9	Initial	0.17	1.8
-20 °C	0.13	1.9	-20 °C	0.18	1.9
4 °C	0.2	1.7	4 °C	0.18	1.9
a.t.	0.2	1.8	a.t.	0.2	1.8
a.t. + Ar	0.19	1.8	a.t. + Ar	0.23	1.7

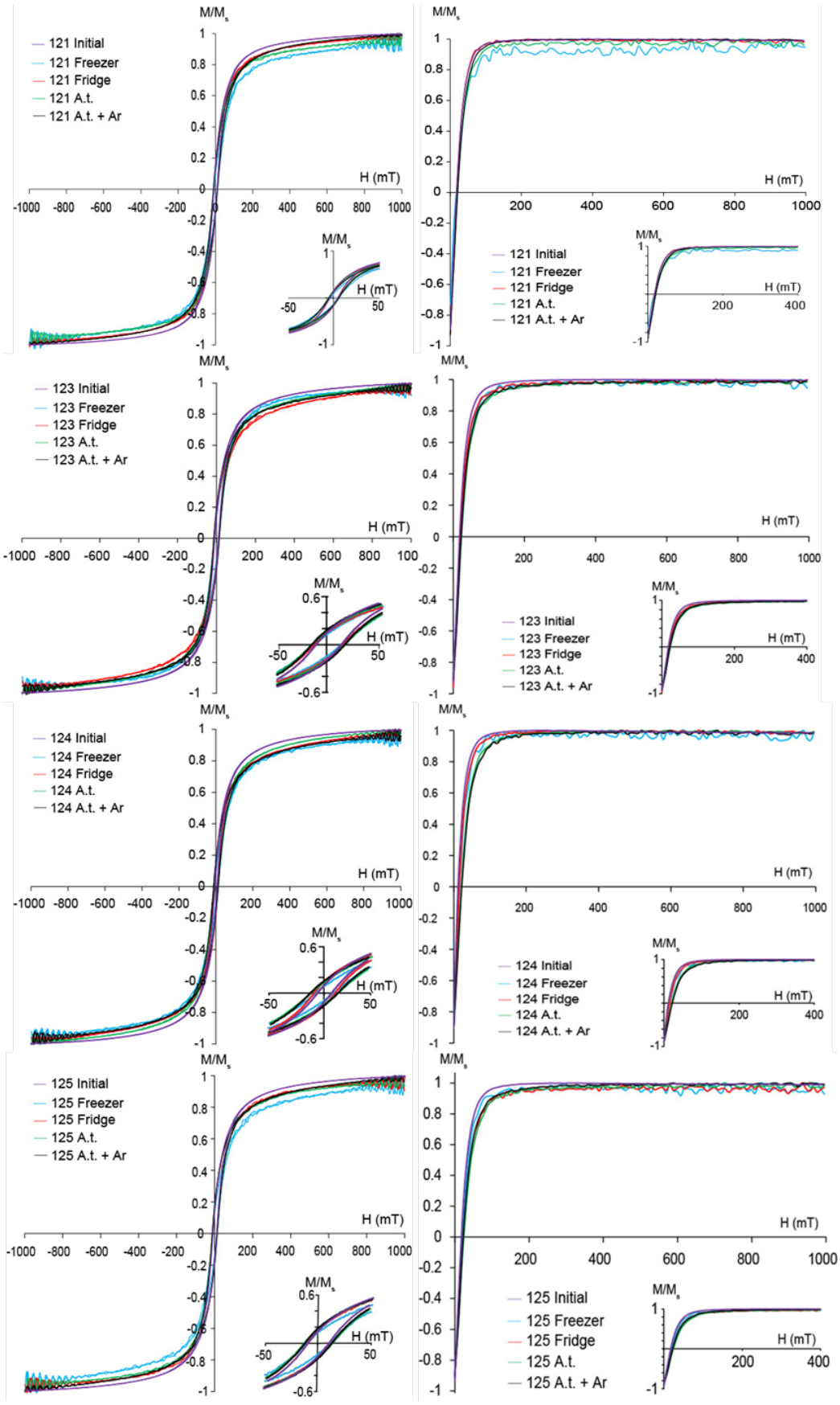

Figure 5.10: Initial and final states of the samples 121, 123, 124 and 125. (a) Hysteresis loops with expanded view to identify M_r and H_c. and (b) isothermal remanent magnetization curve (IRM).

5.3 Discussion

Concerning the storage conditions there are two major findings. First, the lower the temperature the slower the oxidation proceeds. This is no surprise as the oxidation might have an Activation barrier that is easier to overcome at higher temperatures. Second, the oxidation proceeded regardless to whether samples were flushed with argon or not. This suggests that the argon atmosphere was not stable over time and that oxygen penetrated the sample nearly as efficiently as in the case of the non-flushed samples.

The size has an important impact on the oxidation process; smaller particles oxidize more readily than larger particles. But there seems to be a threshold where a difference in size does not influence the oxidation rate too much anymore. For larger samples (50–63 nm) the development of the oxidized layer is similar at each temperature and compared to the sample with small particles (33 nm) the maghemite layer is significantly thinner.

A decrease in FWHM was determined for all samples and one interpretation is the decrease of the crystallite size (Scherrer equation) of the phase the peak belongs to. This would fit with the core-shell-model as the initial phase (magnetite) is shrinking at the expense of the growing outer shell (maghemite). Another effect is caused by the oxidation itself. The overall measured fwhm (e.g. 311-peak, q = 24.8-24.95 nm^{-1}) is an overlap of the initial magnetite peak and a growing maghemite peak. Due the proceeding oxidation a small, broad maghemite peak is formed on the edge of the comparably big magnetite peak, and the overlapping of both peaks results in a broader peak. The increase in peak width seems to be correlated to the absolute peak width. Sample 124 has the largest values and the smallest changes and vice-versa for sample 121. A peak that is already broad, like it is for sample 124, is less affected by a growing shoulder peak whereas a shoulder peak contributes more to the width of a narrow peak, like it is for the other samples.

The results of magnetic measurements showed only little change in properties, a decrease of M_{RS}/M_S and an increase of H_{CR}/H_C and would indicate oxidation to hematite. But this is only the case for one sample, in sample 121 stored in the freezer H_{CR}/H_C is increased. Here there might have been little transformation to hematite. XRD confirmed that in all samples magnetite/maghemite was the main phase at all times. With HR-TEM maghemite layers could be found on the edges of the particles and traces of feroxyhyte were present, similar to a former study [61]. Lattice parameter changes also indicate oxidation from magnetite to

maghemite but concerning the magnetic properties there are no significant changes after 18 months. To sum up, particles are more stable at lower temperatures and when having a larger mean particle diameter. Due to the similar structure of magnetite and maghemite this change does not have a measurable effect concerning the magnetic properties.

6 Biomimetic Magnetite Formation

6.1 Magnetochrome-Mediated Magnetite Formation

Magnetochrome-mediated magnetite formation was part of an article published by Siponen at al. [62]. Mutational analysis, enzyme kinetics and co-crystallization with Fe^{II} identified MamP as an iron oxidase that might contribute to the formation of ferrihydrite, which is a candidate for being a precursor in magnetite formation. This potential of oxidizing Fe^{II} followed by ferrihydrite formation was investigated in this section.

6.1.1 Background

Magnetotactic bacteria (MTB) have the ability to align with the lines of the Earth's magnetic field. This feature, which is called magnetotaxis, helps them finding their preferred environment more efficiently and is achieved by a chain-like arrangement of magnetic nanoparticles, which is in most cases magnetite [6].

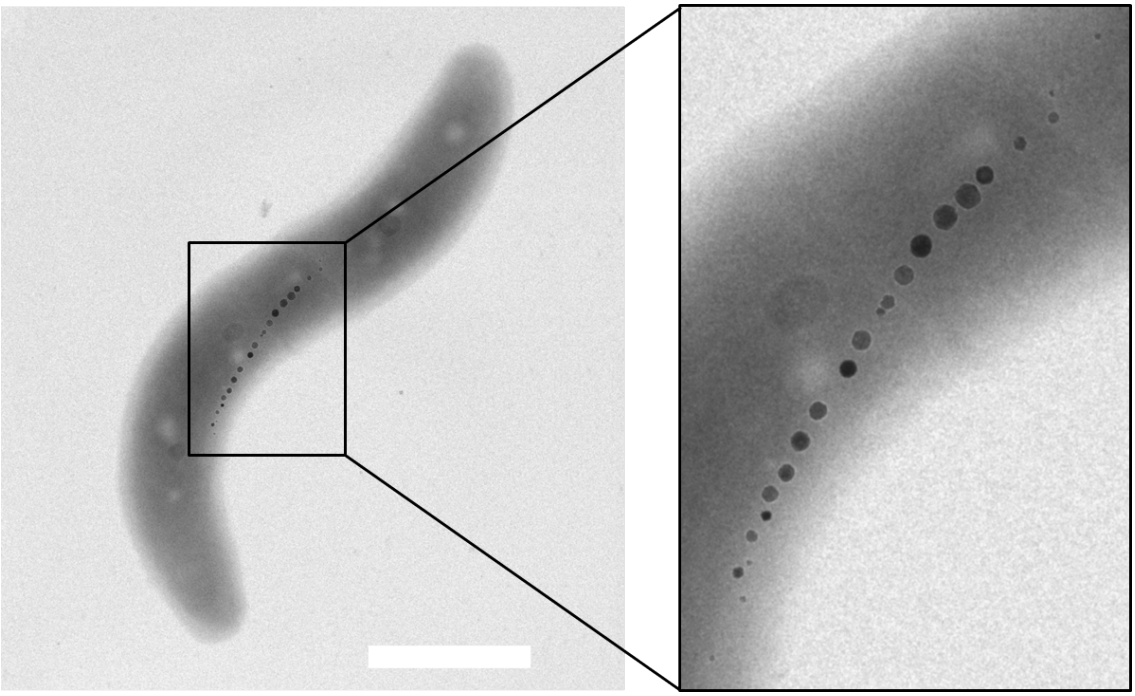

Figure 6.1: A TEM image of a magnetotactic bacterium of the species *Magnetospirillum gryphyswaldense* (MSR-1). MSR-1 has a spirillar shape and a single magnetosome chain; this example is ~4 µm long (scale bar: 1000 nm). The inset to the magnetosome chain reveals well-aligned magnetite nanoparticles with isotropic shape (the largest particles are ~50 nm).

These chain-like organized magnetite nanoparticles, encapsulated in a lipid vesicle are called magnetosomes and they serve as a compass needle. To align in the magnetic field, the particles must have a size beyond the SP/SSD threshold and a narrow the size distribution is helpful in terms of effectiveness. All processes that are involved in the development of the magnetosomes are driven by MTB-specific proteins, which are usually called *mam* or *mms* proteins (referring to "magnetosome membrane" and "magnetosome membrane specific", respectively). These proteins are responsible for the iron uptake, the formation of magnetite and the alignment in chains [6].

One crucial function is the control of the redox potential in the region of magnetite nucleation and growth. Proteins that are involved in redox control are called magnetochromes (referring to cytochromes and their redox function) [63]. One protein that is potentially being involved in redox reactions and which found in all MTB is called MamP [62]. It was shown that deletion mutants of this gene (*ΔmamP*) show defects in the biomineralization process [64]. One main focus of this work is to help understand the role of MamP during magnetite biomineralization. *In vitro* experiments lacking ferric ions revealed the oxidizing nature of the protein. Synthesis with MamP was performed at pH 9 and pH 10 with a concentration of 1.15 mg mL^{-1}. Due to limited amount of materials, it was not possible to perform triplets but only two different experiments and corresponding control experiments without MamP.

6.1.2 Results

The XRD results for magnetite formation with MamP at pH 9 are presented in Figure 6.2. Figure 6.2a shows that there is no crystalline iron rich phase during the first 60 minutes at pH 9. Later, the XRD pattern shows peaks that are very likely a mixture of magnetite and another Fe^{III}-phase. Peaks at q = 28.2 nm^{-1} and 32.4 nm^{-1} do not belong to magnetite and can be assigned to ferric oxyhydroxides, like ferrihydrite or feroxyhyte. A closer look to the peak at $q \approx 25$ nm^{-1} in Figure 6.2b reveals that one peak is growing with time and after a certain time a second, slightly shifted peak is overlapping and finally dominating the first peak. Exact positions were calculated from a cumulative peak fit (Figure 6.2e and Table 6.1). Figure 6.2c

reveals a similar behavior; at $q \approx 43$ nm^{-1} a peak is growing with time and at the last measurement, it is dominated by another, slightly shifted peak. Figure 6.2d shows the image of the corresponding cumulative peak fit (multiple fit with a pseudovoigt function with origin).

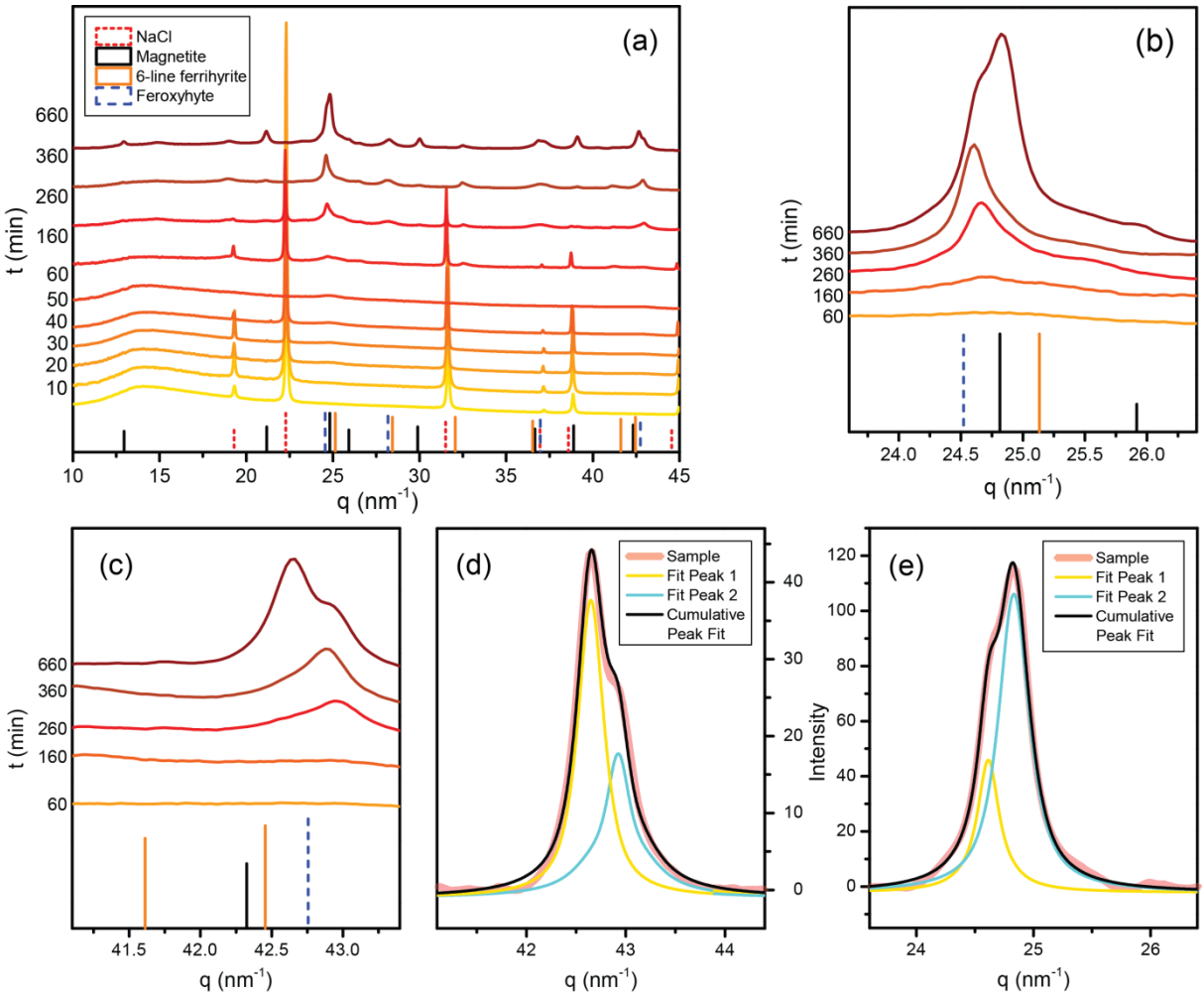

Figure 6.2: Synthesis of magnetite with MamP at pH 9. (a) The chronological evolution is indicated by a color scale from yellow (early state) to dark red (late state) and NaCl is visible as a side product. Development of the pattern indicates the formation of one or more crystalline phases. Insights into $q \approx 25$ nm^{-1} *and* $q \approx 43$ nm^{-1} ((b) and (c), respectively) reveal growth of a peak and after 660 minutes a second, shifted peak appears. Both peaks overlap and (d) and (e) are double peak fits of (b) and (c), respectively.

A synthesis with pH 10 shows similar results to the former. The entire pattern shows increasing crystallinity with time but crystallinity occurs earlier than at pH 9 (Figure 6.3a). The pattern can be assigned to a mixture of magnetite and another Fe^{III}-phase, either ferrihydrite or feroxyhyte. Insights into the regions at $q \approx 25$ nm^{-1} and 43 nm^{-1} show a

growing peak and a later growing shoulder aside (Figure 6.3b and c). Exact peak positions were calculated with cumulative peak fit (Figure 6.3d and e).

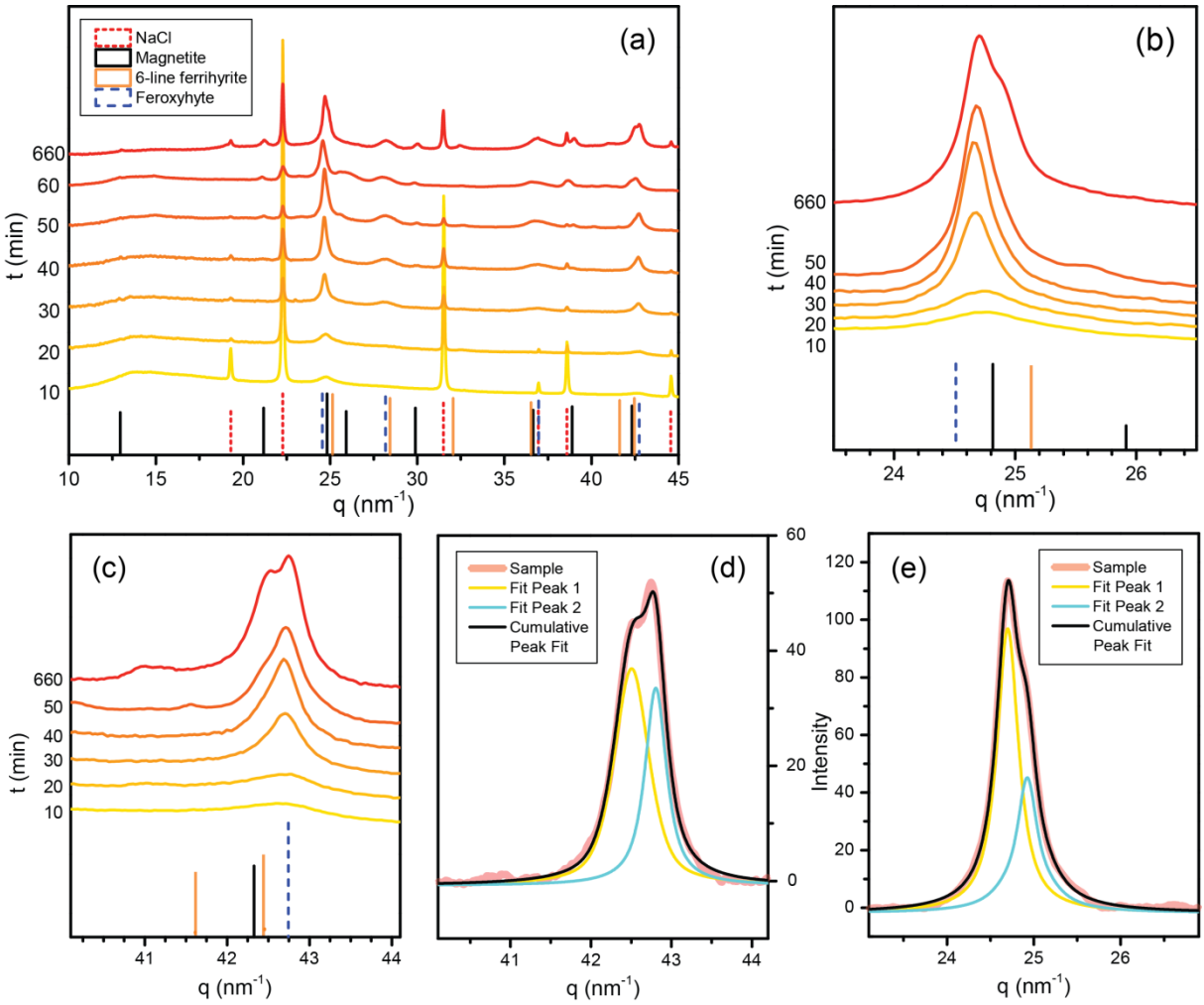

Figure 6.3: Synthesis of magnetite with MamP at pH 10. (a) The chronological evolution is indicated by a color scale from yellow (early state) to red (late state) and NaCl is visible as a side product. Development of the pattern indicates formation of a crystalline phase. Insights into $q \approx 25$ nm^{-1} *and* $q \approx 43$ nm^{-1} ((b) and (c), respectively) reveal growth of one peak and after 660 minutes a second shifted peak appears. Both peaks overlap (d) and (e) are double peak fits of (b) and (c), respectively.

Table 6.1: Summary of significant peaks of XRD patterns of magnetite formation from Fe^{II} and *mamP* synthesis at pH 9 and 10 and their accordance to magnetite, ferrihydrite and feroxyhyte.

Sample	q-spacing (nm^{-1})							
pH 9	~21.5	24.61	24.83	~28.2	~32.4	~38.5	42.65	42.92
pH 10	~21.5	24.7	24.92	~28.2	~32.5	~38.5	42.51	42.81
Accordance to								
magnetite (24.82nm^{-1}, 42.33 nm^{-1})	x		x			x	x	x
ferrihydrite (25.13 nm^{-1}, 28.43 nm^{-1}, 32.06 nm^{-1}, 42.45 nm^{-1})			x	x	x			x
feroxyhyte (24.54 nm^{-1}, 28.18 nm^{-1}, 42.74 nm^{-1})		x		x				x

Control experiments, in which ferrous ions were added to a medium lacking MamP were also done at pH 9 and 10. The reactor solution remained greenish-blue, typical for ferrous solutions, as long as nitrogen atmosphere was ensured (Figure 6.4a) and color changed to yellow, brownish shortly after being exposed to oxygen (Figure 6.4b). Transmission electron microscopy showed poorly crystalline material with an electron diffraction pattern similar to ferrihydrite (Figure 6.4c) and some needle-like structures indicating the presence of goethite (Figure 6.4d). The diffraction pattern showed a paradigmatic magnetite pattern (Figure 6.4e).

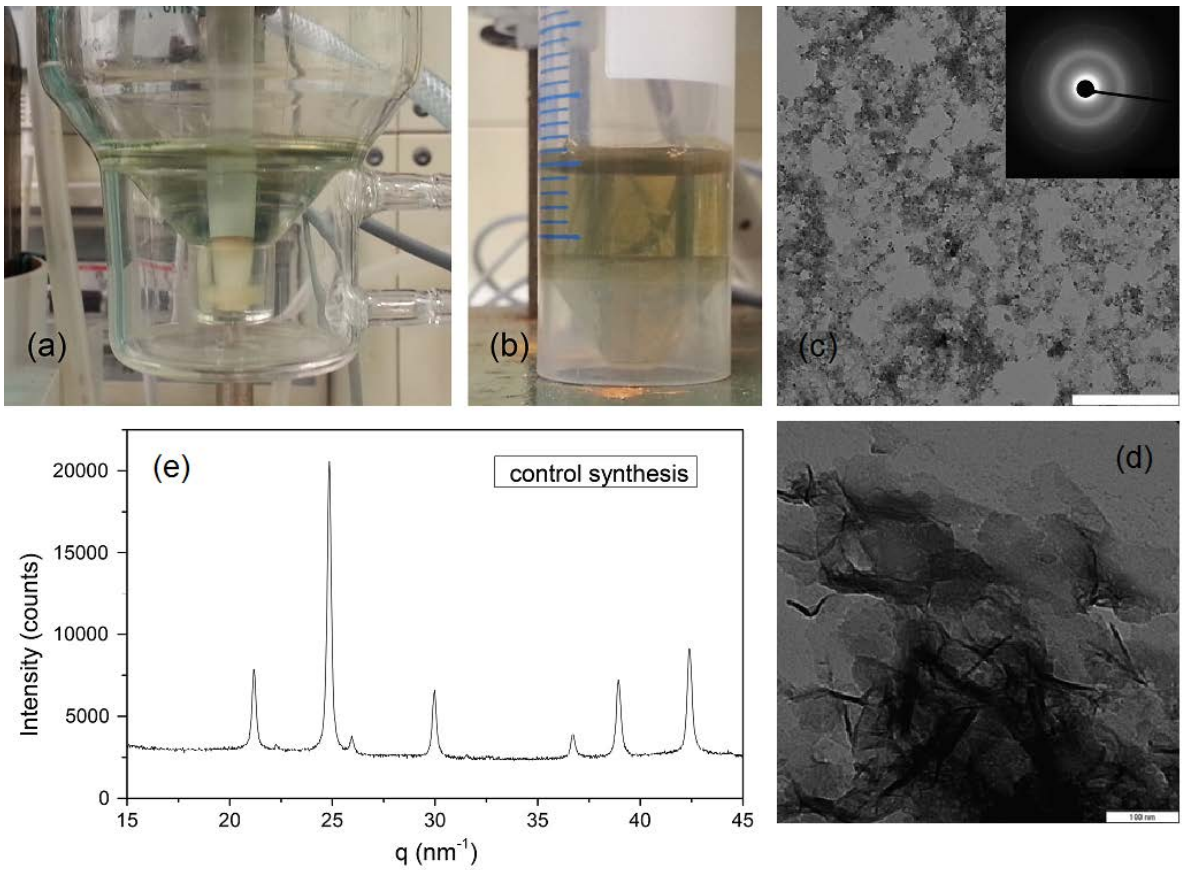

Figure 6.4: Control synthesis without mamP shows (a) typical greenish blue color of dissolved ferrous ions during the synthesis and without oxygen presence and (b) as soon as the product is being removed from nitrogen atmosphere, the solution changes color to yellow/brownish. TEM image of pH 9 shows (c) a poorly crystalline material with an electron diffraction pattern similar to 2-line ferrihydrite (scale bar: 1000 nm) and (d) a closer look reveals needle like structures that are typical for goethite (scale bar: 100 nm). (e) A diffraction pattern of a very long (10h) synthesis resulted in a paradigmatic XRD magnetite pattern.

6.1.3 Discussion

The control experiment has shown that subsequent oxidation of Fe^{II} to Fe^{III} may play a crucial role. The color change indicates oxidation of ferrous iron in the reactor. In consequence, it is possible that the oxygen atmosphere causes subsequent oxidation and hence magnetite formation. Reliable results of processes in the reactor are only obtained when subsequent oxidation can be excluded, either with in situ XRD measurements or a proper sealing of the samples after synthesis and during the XRD measurements.

However, there are clear differences in the results depending on the presence or absence of MamP. Addition of Fe^{II} ions to an alkaline solution containing MamP leads to the presence of ferric oxyhydroxides as indicated by XRD, most likely ferrihydrite or feroxyhyte. The following scenario is conceivable; added ferrous ions are oxidized by MamP and ferrihydrite

or feroxyhyte is immediately formed. This process is active as long as the entire oxidizing potential of MamP is not yet consumed. The exact peak positions at $q \approx 25$ nm^{-1} *and* $q \approx 43$ nm^{-1} in Table 6.1 indicate that feroxyhyte peaks are formed at early states and at the final state magnetite peaks are present (peaks that can only be assigned to magnetite at $q \approx 21.5$ nm^{-1} *and* $q \approx 38.5$ nm^{-1}). Ferrihydrite is present at every time point (the peak at $q \approx 32.5$ nm^{-1} can only be assigned to 6-line ferrihydrite). The transformational processes in between those phases are not detectable here, however, Baumgartner et al. suggested that ferrihydrite is the most likely precursor of magnetite [20]. After the oxidizing potential is exhausted, magnetite starts being formed from the oxyhydroxides present and further added Fe^{II}. If the synthesis is lacking MamP, there is no oxidation to oxyhydroxides during the synthesis however, subsequent oxidation leads to magnetite formation. Subsequent oxidation plays an important role and it is not possible to make final conclusions about the potential of forming magnetite, but it does oxidize Fe^{II} and after this oxidation magnetite was formed. Further experiments are necessary to investigate the potential of MamP.

6.2 Phage Display

6.2.1 Background

Phage display is a selection technique in which a library of peptide variants is expressed on the outside of a phage virion [65]. A large library of phages with peptides bound on the outer surface is run through a selection process. The selection process consists of several rounds of surface panning in which, due to the peptide's binding affinity to a given target, phages are either discarded or kept in the pool. The presence of a surfactant helps impede the non-specific binding and the step-wise increase of its concentration leads to a final pool of specifically binding peptides. The aim of the phage display experiments in this work was to determine a set of peptides that specifically binds to a (111)-magnetite surface. By doing so a peptide could hinder the (111)-face to grow and may provoke an octahedral crystal morphology. Epitaxially grown thin films of magnetite [66] were exposed to the phage library and after three consecutive rounds of exposure, washing and elution, 30 different phages where separately amplified and their isolated DNA was sent to Eurofins MWG Operon (Ebersberg, Germany) to determine the sequence of amino acids.

6.2.2 Experimental

The phages, which were used in this work, are equipped with peptides of 12 amino acids in length. The initial concentration of phages was 1×10^{13} pfu mL^{-1} and consisted of 1.2×10^{9} different sequences, which results in a 100-fold appearance of one sequence in 10 µL of phage library solution. The target was a (111)-face of thin magnetite film, produced by epitaxial growth on a $SrTiO_3$ substrate [66]. One phage display experiment consisted of:

- surface panning – the magnetite face was exposed to 2 mL of TBS, pH 7.5 with according surfactant concentration and number of phages (Table6.2) for one hour,
- a washing step to remove non-specifically bound phages (10x with 2 mL of TBS plus surfactant with according concentration (Table6.2),
- detaching the bound phages from the magnetite thin film (40 µL of 0.2 M glycine-HCl, pH 2.2 for 10 min),
- buffering the detached phages (6 µL of 1 M Tris-HCl, pH 9.1),

- a phage tittering step to determine of the number of phages that were specifically bound to the magnetite thin film
- and a phage amplification step to produce a sufficient number for the following experiment.

During three consecutive experiments of surface panning, the starting phage number was kept nearly constant whereas the concentration of the surfactant was gradually increased (Table6.2). Commercially available tenside Tween20 served as the surfactant. After the third experiment, 30 phages where randomly chosen, isolated and separately amplified for sequencing. The DNA of the chosen phages was isolated with a commercially available DNA kit (QIAprep Spin Miniprep Kit (50), QIAGEN, Hilden, Germany) and afterwards sent to Eurofins MWG Operon (Ebersberg, Germany) for sequence determination.

Table6.2: In three rounds of surface panning with similar initial number of plague forming units and increasing surfactant concentration. The resulting number of plague forming units decreased with increasing surfactant concentration.

Rounds	$n_{initial}$ (pfu)	$c_{Tween20}$ (Vol-%)	n_{final} (pfu)
1	1×10^{11}	0.1	1.2×10^{5}
2	1×10^{11}	0.2	3×10^{4}
3	7×10^{10}	0.5	9×10^{2}

6.2.3 Results

Seven sequences were not detectable due to incorrect DNA isolation, however, sequences could be assigned to the remaining 23 phage batches and results are presented in Table 6.3. Seven different sequences occur once, three sequences occur twice and two different sequences occur four times and six times, respectively.

Table 6.3: The results of phage display after three rounds of surface panning. 23 sequences were obtained from isolated DNA.

Occurrence	Sequence
6x	S G V Y K V A Y D W Q H
4x	G Q S E H H M R V A S F
2x	H M K S T V G G P D G W
	G L H T S A T N L Y L H
	Y S S D Q E P A R D H N
1x	W L N P G I V P A S Q H
	M H P N A G H G S L M R
	S Q D I R T W N G T R S
	V H W D F R Q W W Q P S
	E L V D V K T T A D P F
	G Y R A G D T K S V F V
	V S I H E R T W A T K R

In order to classify the result, the initial distribution was separated into polar uncharged, charged and nonpolar groups. The amino acid distribution was calculated from the sum of all 12 × 23 amino acids and the results are presented in comparison to the initial distribution and a former study on hematite (Table 6.4). The distribution of the magnetite study is very close to that of the initial phage library. Lower et al. observed a clear increase of polar uncharged amino acids, in particular Serine and Threonine appeared often [67].

Table 6.4: Distribution of amino acids suggested by Lower et al. [67], divided into groups with polar uncharged, polar charged, nonpolar hydrophobic/aromatic side groups and proline and serine, threonine.

Amino Acids	Ph.D.-library	Hematite	Magnetite
Polar uncharged (C, H, N, Q, S, T)	32.1	53	33.3
Polar charged (D, E, K, R)	15.7	7	17.8
Nonpolar hydrophobic, aromatic (A, F, I, L, M, V, W, Y)	35.5	28	37
Proline	8.1	11	3.3
S, T	19.0	32	15.2
positively charged (R, H, K)	12.6	9.2	18.5
negatively charged (D, E)	7.7	2.9	9.1

6.2.4 Discussion

The isoelectric point of hematite is at pI = 8.4 – 8.5, which results in a positively charged surface during the surface panning (pH = 7.5). Surprisingly, the percentage of both, negatively and positively charged amino acids is decreased in comparison to the initial library. One would expect that negatively charged side groups have an increased affinity to the positively charged hematite surface. In fact, amino acids with polar uncharged side groups occur to a higher percentage and hence have specific binding affinity to hematite. In contrast to hematite, magnetite has its isoelectric point at pI = 6.3 – 6.8, which results in a negatively charged surface during surface panning. A clear increase of positively charged amino acids and a constant percentage of negatively charged amino acids indicate specific binding to the negatively charged surface. The number of polar amino acids like serine and threonine is increased in the hematite study and the hypothesis is that hydroxyl groups are able to bind to the hematite surface via hydrogen bonds. There is no indication that there is an increased affinity to form hydrogen bonds with magnetite.

Lower et al. have furthermore suggested a binding motif for hematite, which was based on 20 sequences of 12-amino-acid-petides [67]. They found that in 60% of the peptides, there is a sequence that is: polar uncharged – S/T – polar uncharged – polar uncharged – S/T – nonpolar – S/T– P – S/T. Based on this separation of polar uncharged, polar charged and hydrophobic side groups there was no apparent binding motif observable for magnetite.

In summary, concerning the composition of amino acids the results confirm the negative charge of magnetite under the given conditions although the percentage of the nonpolar, hydrophobic amino acids is surprisingly similar to the initial distribution. The isoelectric point and the actual pH during the surface panning are similar and this might cause a comparably neutral surface and hence might allow the binding of amino acids with nonpolar side groups. A preferred binding, which is stronger to the (111)-magnetite face compared to other faces can only be demonstrated by using these other faces in similar phage display experiments. Nevertheless magnetite formation with peptides in the reactor was performed and the results are presented in the following section.

6.3 Synthesis of Magnetite with Peptides from Phage Display

6.3.1 Background

Initially all peptides with multiple occurrences were chosen for the magnetite formation experiments. Peptides were dissolved in water and they concentration was determined based on the absorbance at 280 nm [68]. This requires the presence of amino acids with aromatic side groups in the sequence [69], which is the case for tyrosine (Y) or tryptophan (W). One peptide – G Q S E H H M R V A S F – had to be excluded for lack of Y or W. Four peptides contained at least one active side group and their sequence, molar weight and isoelectric point are presented in (Table 6.5). It is remarkable that the last peptide has a pI at 4.3, which means that it is negatively charged at neutral pH whereas the other three peptides are nearly neutral. All peptides are subsequently abbreviated with their first three letters of the sequence.

Table 6.5: The peptides chosen for experiments of magnetite formation. Sequence, consisting of 12 amino acids, the molar weight and the isoelectric point are shown.

Sequence	M (g mol^{-1})	pI
S G V Y K V A Y D W Q H (SGV)	1452.59	7.336
H M K S T V G G P D G W (HMK)	1271.41	7.37
G L H T S A T N L Y L H (GLH)	1326.47	7.523
Y S S D Q E P A R D H N (YSS)	1418.40	4.371

Two sets of experiments were performed, both with a peptide concentration of 0.01 mg mL^{-1}. In one experiment the peptide was added after two hours of formation to study their influence on particle growth at pH 9, 10 and 11. In another experiment the peptides was added before starting the synthesis to study the influence of formation at pH 9.

6.3.2 Results

XRD patterns of all 16 samples confirm magnetite formation except for two samples (Figure 6.5 and Figure 6.6). At pH 9 there is no crystalline phase with addition of SGV after two hours (Figure 6.5a) and addition of YSS leads to the presence of other phases next to magnetite (Figure 6.5d). The size was determined with XRD, but due to the low level of crystallinity and

hence overlapping of the (311)- and the (222)-peak, the MD was calculated from the (440)-peak. The results are shown in Table 6.6. In general, particles are smaller after 4 hours if a peptide is present, no matter if initially added or after two hours. An increase in pH leads to smaller particles. This was already shown for syntheses without additives [70].

Table 6.6: The mean particle diameter in nm was calculated from the (440)-peak at q ≈ 42.32 nm^{-1}. Syntheses of four hours with addition of peptides after two hours result in smaller particles compared to the control synthesis and with increasing pH particles grow less. Initial addition of peptides also leads to smaller particles compared to control experiments (*size was taken from activation energy experiments).

Peptide	**MD (nm)**			
	addition after two hours			initial addition
	pH 9	pH 10	pH 11	pH 9
SGV	-	21	16	26
HMK	31	25	14	32
GLH	36	20	11	32
YSS	27	22	15	22
Control	40*	29	18	40*

TEM images show aggregated magnetite nanoparticles of different size (Figure 6.7). A closer look reveals octahedral magnetite crystals in samples at pH 10 and 11 (Figure 6.8a and b) besides spherical ones. This was not observed at pH 9, where particles appear to be isotropic. Furthermore, organic layers around magnetite nanoparticles could be observed in all samples (Figure 6.8c and d). Contaminations of other iron oxides are also observed, in particular in samples at pH 9. There are needle-like structures (Figure 6.9a) or sheets of iron dense material (Figure 6.9b) and flake-like structures, which are poorly crystalline (Figure 6.9c and d).

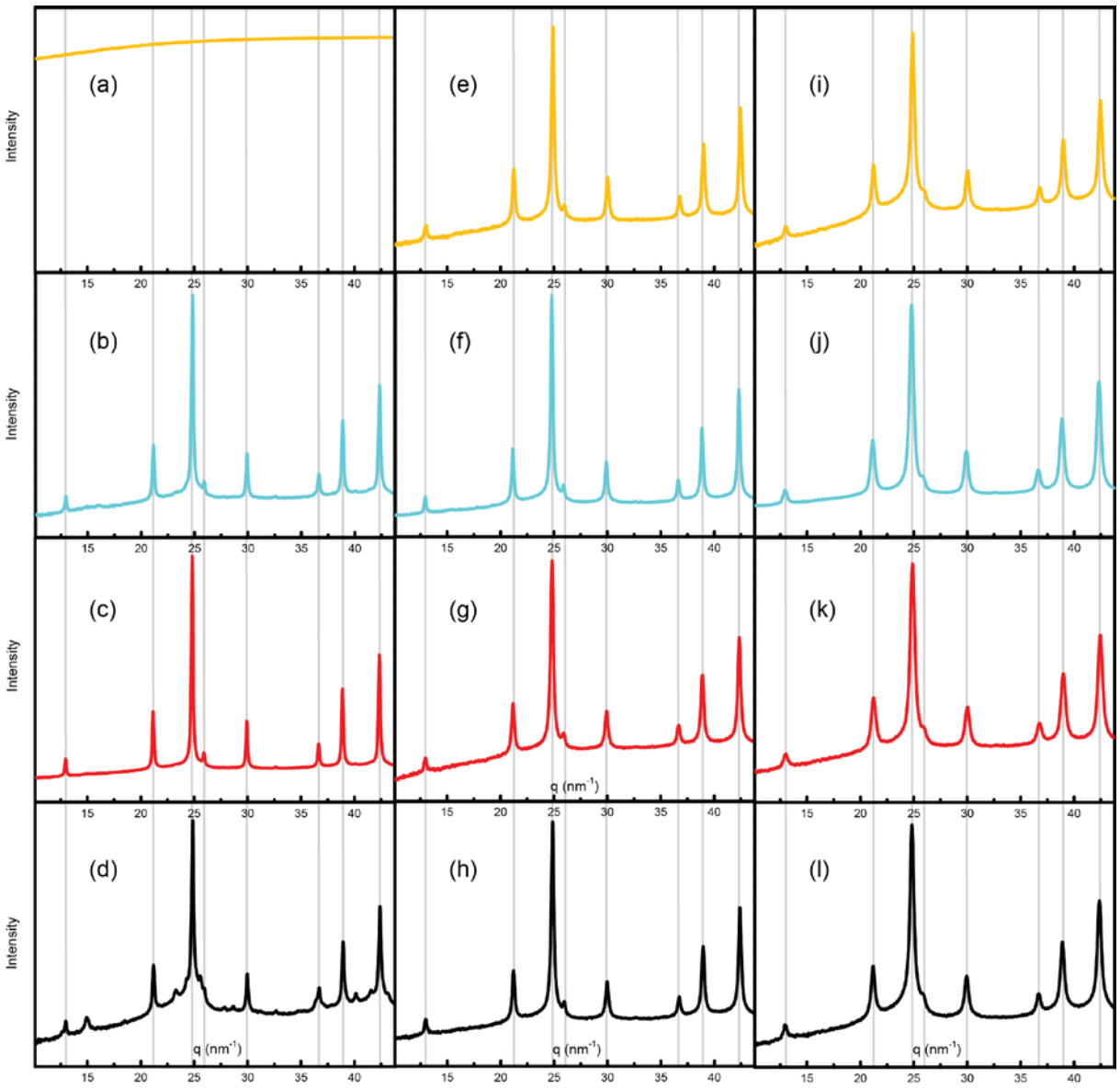

Figure 6.5: XRD patterns of magnetite formation with peptide addition after two hours at pH 9 (left side; a – d), pH 10 (center; e – h) and pH 11 (right side; i – l). Added peptides are SGV (yellow), HMK (blue), GLH (red) and YSS (black). The vertical gray lines indicate the magnetite peak positions. There is no crystalline material in (a) and the pattern of (d) has small additional peaks with the peak at q = 15 nm^{-1} being typical for goethite. The other patterns (b, c and e – l) show typical magnetite peaks.

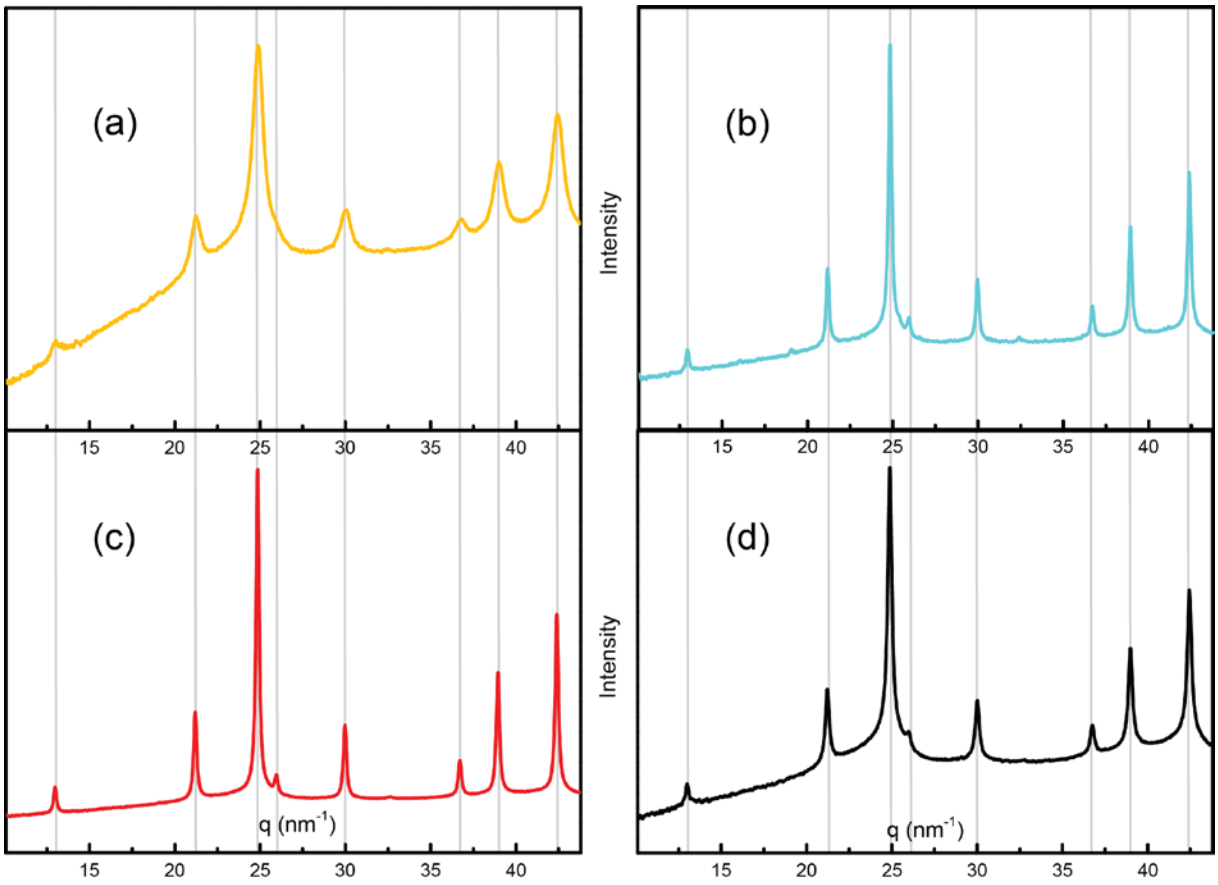

Figure 6.6: XRD patterns of magnetite formation with initial peptide addition at pH 9. Added peptides are SGV (yellow), HMK (blue), GLH (red) and YSS (black). The vertical gray lines indicate the magnetite peak positions. All four patterns show typical magnetite peaks.

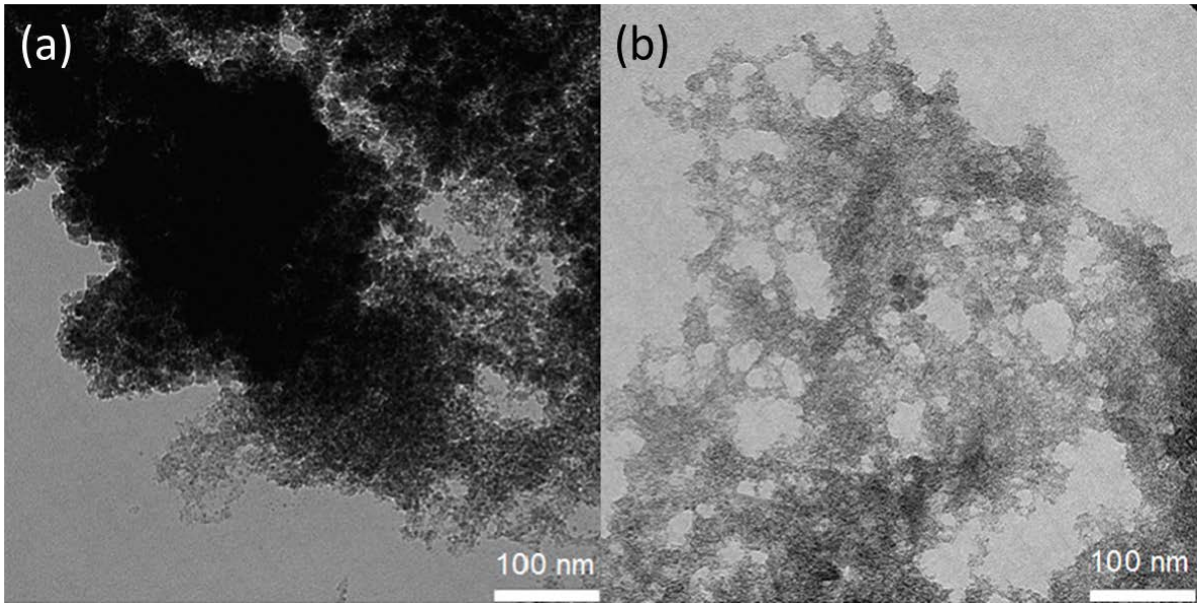

Figure 6.7: TEM images of the samples (a) YSS, pH = 9, initial addition and (b) GLH, pH = 9, addition after two hours. Both images are representative for all samples. Highly aggregated nanoparticles and poorly crystalline material is present.

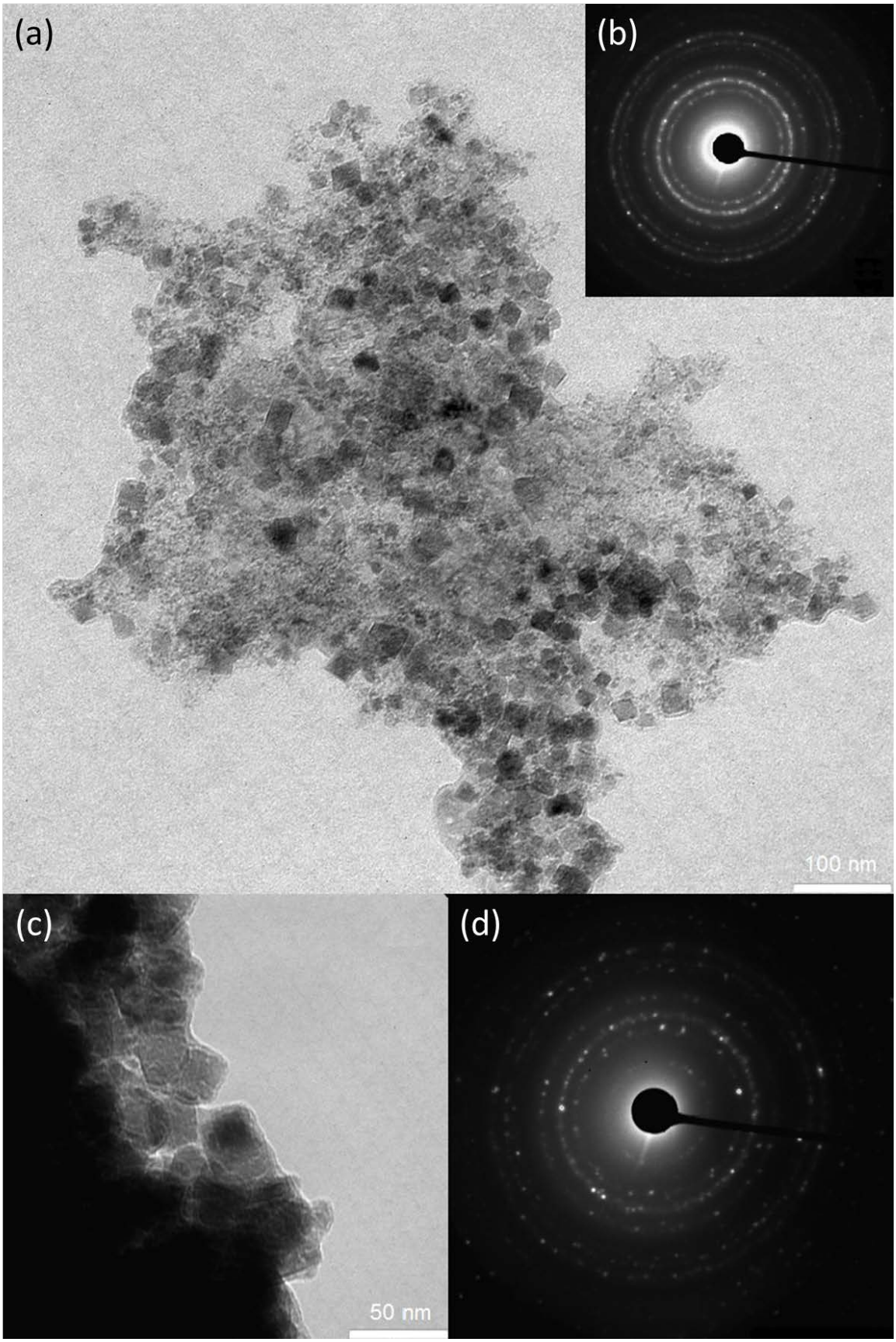

Figure 6.8: (a) TEM image of YSS, pH = 11, addition after two hours. Octahedral crystals are – besides isotropic ones and poorly crystalline material – visible in the agglomerates of nanoparticles. (c) TEM image of YSS, pH = 9, initial addition reveals an organic layer around the particles due to the addition of peptides. The corresponding electron diffraction patterns (b) and (d) confirm the presence of magnetite.

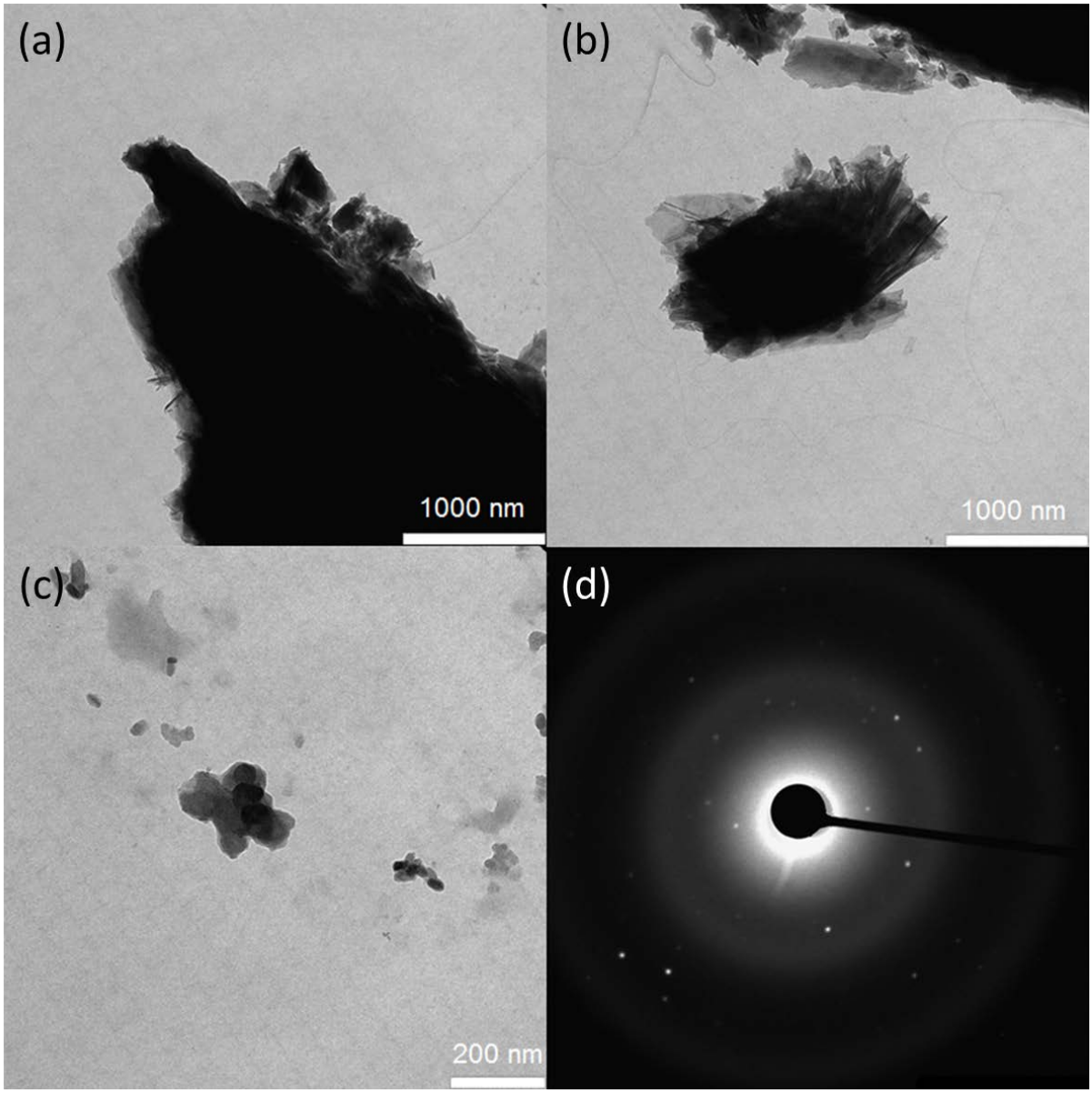

Figure 6.9: (a) and (b) TEM image of HMK, pH = 9, addition after two hours. Needles and sheet-like structures indicate the presence of goethite and lepidocrocite, respectively. (c) GLH, pH = 9, addition after two hours. Flake-like structures may indicate the presence of hematite. (d) The electron diffraction pattern shows poorly crystalline magnetite phase and some single reflections.

6.3.3 Discussion

In general, it is possible to synthesize magnetite nanoparticles in the presence of the chosen peptides and crystal formation is more stable at higher pH-values. Only one sample was lacking crystalline magnetite after four hours and another sample showed bulk goethite contamination. In every sample traces of contamination are visible with TEM and goethite is the favored alternative phase. Perhaps the peptide addition leads to a destabilization of the

magnetite formation. Whether the peptide is added initially or after two hours did not result in noticeable differences.

It is not possible to make a clear statement concerning the potential of these peptides of particular binding to the (111)-face of magnetite, however, the presence of octahedral magnetite crystals indicates an increased affinity to it. Faces that are not bound will grow faster and therefore disappear. In other words, binding of the peptides to the (111)-face hinders its growth and leads to octahedral crystal habits. To change the morphology towards elongated particles, it would be necessary to change the conditions and start a different approach. As long as a potential binding agent can bind to all sides of a crystal it will always bind equally to the chemically equal faces (Figure 6.10).

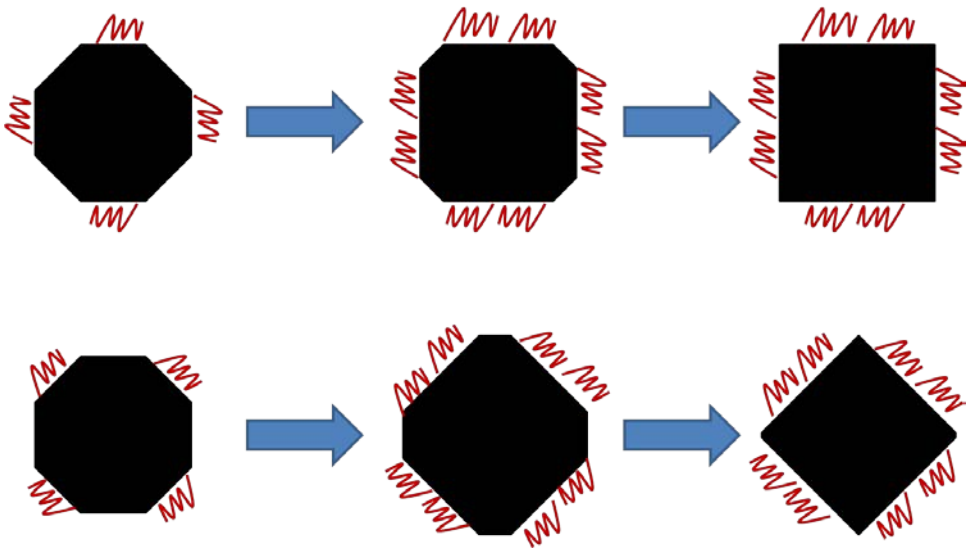

Figure 6.10: The peptide (red line) binds to a growing magnetite nanoparticle (black object). Top: preferred binding to the set of cubic faces leads to disappearance of the octahedral faces. The crystal habit is supposed to be cubic. Bottom: Vise-versa does preferred binding to the set of octahedral faces lead to disappearance of the cubic faces. The crystal habit is supposed to be octahedral.

One potential approach to realize elongation is to bind the peptide to a carrier surface. A formed nanoparticle could bind to the peptide surface and thus one out of four (in 2D) faces is hindered in growing. This could result in elongated particles (Figure 6.11).

Figure 6.11: A substrate (gray box) that binds the peptides (red line) and a growing magnetite nanoparticle. This setup causes attachment of the peptide on only one of the four octahedral faces (2D). The growth of one face is hindered and this leads to the growth of elongated particles.

7 Conclusions and Outlook

One aim of this work was the establishment of a co-precipitation set up that allows synthesizing magnetite particles beyond the SP/SSD threshold at ambient temperatures. Change of temperatures in the range of 5 to 25 °C leaded to particles of sizes between 33 and 63 nm. Temperature can indeed be used as parameter to help obtaining particles of desired size and thereby magnetic properties, as confirmed by the magnetic measurements. Lower temperatures resulted in smaller nanoparticles and hence lower M_S, M_{RS} and H_C after eight hours.

Magnetite formation at different temperatures was also used to gain mechanistic insight into the process of magnetite nanoparticle growth. In particular, the activation energy of magnetite crystal growth was calculated. Nonlinear growth was observed at all temperatures and an activation energy of 28 kJ mol^{-1} was calculated. Based on these results, it was proposed that the rate-determining step is the diffusion of primary particles to the magnetite nanoparticles already formed The prior formation of primary particles entails an increase of the energetic barrier of crystal growth as the diffusion of large clusters is energetically more demanding than the diffusion of ions. An expansion of the temperature range can help to increase the knowledge about the process. The Arrhenius plot of a wider range of temperature could be useful to get a better understanding of the processes playing a role in magnetite formation. However, to realize an expanded temperature range it would be necessary to further develop the experimental setup. Higher temperatures above 25 °C lead to substantial evaporation of water, which significantly influences the synthesis conditions and hence the magnetite formation mechanism.

The development of structural and magnetic properties of magnetite nanoparticles stored under different conditions was investigated to gain insight into their stability and alteration as a function of aging. High-resolution X-ray diffraction was used to distinguish between magnetite and maghemite, and thereby, to estimate the oxidation process by observing the evolution of the lattice parameter under different storage conditions over 18 months. We confirmed experimentally that smaller particles oxidize faster than larger particles due to the

higher surface-to-volume ratio. The lower the temperature the less oxidation is observed. An oxidation parameter was introduced to describe the growth of a maghemite layer around a magnetite core. In addition the magnetic properties of the same set of samples were analyzed. The magnetic properties of the samples do not vary greatly with aging and increasing degree of oxidation, probably because the magnetic properties of magnetite and maghemite are similar. Similar to observations from XRD, the least changes in magnetic properties are observed for particles stored at -20 °C, followed by 4 °C and ambient temperature and the smallest particles exhibit the biggest changes. The study has shown that an oxidation layer is formed on the surface of magnetite nanoparticles, however, this layer does not impact the magnetic properties of the samples dramatically. Consequently, if magnetic properties are necessary, for example, in biomedical applications such as drug targeting, the particles are not altered dramatically over a period of more than a year. Due to experimental restrictions it was not possible to observe short-term changes as the first XRD data were gained from particles being at least one week old. Here it would be very helpful to be able to investigate changes of structure and magnetic properties within the first hours or even minutes to observe the particles already at the first oxidation steps.

The influence of MamP was established in precipitation experiments where addition of ferrous chloride in alkaline medium – in the absence of any ferric iron – resulted in mixtures of magnetite and ferric oxyhydroxides. MamP acts as a redox agent that is able to oxidize ferrous ions that are added to the reactor. Thus, a ferric oxyhydroxy-phase is first formed and later, due to the exhaust of the oxidizing agent, further addition of Fe^{II} results in magnetite formation. Phage display experiments were performed to find peptide sequences that preferably bind to a (111)-magnetite face. The different detected sequences were used to perform a first set of co-precipitation experiments to study the influence of these peptides on magnetite formation. It could be confirmed that formation is possible and that peptides have an influence on morphology, the presence of (111)-face affine peptides leads to octahedral crystals. The next step would be the formation of elongated nanoparticles. This requires further development of the experimental setup. A peptide that is evenly distributed in the solution will equally bind to all sides of the crystal and thus lead to isotropic particles. A synthesis with a protein fixed on a surface and nanoparticle growth on top of it could lead to elongated particles.

References

[1] S. Laurent, D. Forge, M. Port, A. Roch, C. Robic, L. Vander Elst, and R. N. Muller, "Magnetic iron oxide nanoparticles: synthesis, stabilization, vectorization, physicochemical characterizations, and biological applications.," *Chem. Rev.*, vol. 108, no. 6, pp. 2064–110, Jun. 2008.

[2] R. a Frimpong and J. Z. Hilt, "Magnetic nanoparticles in biomedicine: synthesis, functionalization and applications.," *Nanomedicine (Lond).*, vol. 5, no. 9, pp. 1401–14, Nov. 2010.

[3] U. Schwertmann and R. M. Cornell, "The Iron Oxides." 2003.

[4] R. F. Butler, *PALEOMAGNETISM : Magnetic Domains to Geologic Terranes*, no. May. 1998.

[5] L. Tauxe, S. K. Banerjee, R. F. Butler, and R. van der Voo, *Essentials of Paleomagnetism*. 2009.

[6] D. Faivre and D. Schüler, "Magnetotactic bacteria and magnetosomes.," *Chem. Rev.*, vol. 108, no. 11, pp. 4875–98, Nov. 2008.

[7] D. J. Dunlop and Ö. Özdemir, *Rock Magnetism: Fundamentials and Frontiers*. 1997.

[8] R. F. Butler and S. K. Banerjee, "Theoretical single-domain grain size range in magnetite and titanomagnetite," *J. Geophys. Res.*, vol. 80, no. 29, pp. 4049–4058, Oct. 1975.

[9] W. Williams, A. R. Muxworthy, and G. a. Paterson, "Configurational anisotropy in single-domain and pseudosingle-domain grains of magnetite," *J. Geophys. Res.*, vol. 111, no. B12, p. B12S13, Nov. 2006.

[10] A. R. Muxworthy and W. Williams, "Critical single-domain/multidomain grain sizes in noninteracting and interacting elongated magnetite particles: Implications for magnetosomes," *J. Geophys. Res.*, vol. 111, no. B12, p. B12S12, Nov. 2006.

[11] D. D. Eberl, V. A. Drits, and J. Srodon, "Deducing growth mechanisms for minerals from the shapos of crystal size distributions." 1998.

[12] D. E. Kile and D. D. Eberl, "On the origin of size-dependent and size-independent crystal growth : Influence of advection and diffusion," *Am. Mineral.*, vol. 88, no. 1, pp. 1514–1521, 2003.

[13] D. Gebauer, M. Kellermeier, J. D. Gale, L. Bergström, and H. Cölfen, "Pre-nucleation clusters as solute precursors in crystallisation.," *Chem. Soc. Rev.*, vol. 43, no. 7, pp. 2348–71, Apr. 2014.

[14] J. W. Cahn, “Theory of crystal growth and interface motion in crystalline materials,” *Acta Metall.*, vol. 8, pp. 554–562, 1960.

[15] K. Binder, “Theory of first-order phase transitions,” *Reports Prog. Phys.*, vol. 50, no. 7, pp. 783–859, Jul. 1987.

[16] P. Fratzl, J. L. Lebowitz, O. Penrose, and J. Amar, “Scaling functions, self-similarity and the morphology of phase-seperating systems,” *Phys. Rev. B*, vol. 44, no. 10, 1991.

[17] J. W. Mullin, *Crystallization*. 2001.

[18] W. J. E. M. Habraken, J. Tao, L. J. Brylka, H. Friedrich, L. Bertinetti, A. S. Schenk, A. Verch, V. Dmitrovic, P. H. H. Bomans, P. M. Frederik, J. Laven, P. van der Schoot, B. Aichmayer, G. de With, J. J. DeYoreo, and N. a J. M. Sommerdijk, “Ion-association complexes unite classical and non-classical theories for the biomimetic nucleation of calcium phosphate.,” *Nat. Commun.*, vol. 4, p. 1507, Jan. 2013.

[19] D. Gebauer, A. Völkel, and H. Cölfen, “Stable prenucleation calcium carbonate clusters.,” *Science*, vol. 322, no. 5909, pp. 1819–22, Dec. 2008.

[20] J. Baumgartner, A. Dey, P. H. H. Bomans, C. Le Coadou, P. Fratzl, N. a J. M. Sommerdijk, and D. Faivre, “Nucleation and growth of magnetite from solution.,” *Nat. Mater.*, vol. 12, no. 4, pp. 310–4, Apr. 2013.

[21] E. R. Leite and C. Robeiro, *Crystallization and Growth of Colloidal Nanocrystals*. 2012.

[22] I. M. Lifshitz and V. V. Slyozov, “The Kinetics of Precipitation from Supersaturated Solid Solutions,” vol. 19, no. 1, pp. 35–50, 1961.

[23] C. Wagner, “Theorie der Alterung von Niederschlägen durch Umlösen (Ostwald-Reifung),” vol. 65, no. 7, pp. 581–591, 1961.

[24] E. J. H. Lee, C. Ribeiro, E. Longo, and E. R. Leite, “Growth kinetics of tin oxide nanocrystals in colloidal suspensions under hydrothermal conditions,” *Chem. Phys.*, vol. 328, no. 1–3, pp. 229–235, Sep. 2006.

[25] F. Huang, H. Zhang, and J. F. Banfield, “Two-Stage Crystal-Growth Kinetics Observed during Hydrothermal Coarsening of Nanocrystalline ZnS,” *Nano Lett.*, vol. 3, no. 3, pp. 373–378, Mar. 2003.

[26] T. A. Vu, M. M. Reagan, D. Li, B. Legg, J. J. De Yoreo, J. F. Banfield, and H. Zhang, “Kinetics of crystal growth of nanogoethite in aqueous solutions containing nitrate and sulfate anions,” *CrystEngComm*, vol. 16, no. 8, p. 1466, 2014.

[27] P. A. van Aken, V. J. Styrsa, and B. Liebscher, “Quantitative determination of iron oxidation states in minerals using Fe L 2 , 3 -edge electron energy-loss near-edge structure spectroscopy,” vol. 4, pp. 323–327, 1998.

[28] G. a. Waychunas, M. J. Apted, and G. E. Brown, “X-ray K-edge absorption spectra of Fe minerals and model compounds: Near-edge structure,” *Phys. Chem. Miner.*, vol. 10, no. 1, pp. 1–9, Jan. 1983.

[29] J. P. Crocombette, M. Pollak, F. Jollet, N. Thromat, and M. Gautier-Soyer, “X-ray-absorption spectroscopy at the Fe L2,3 threshold in iron oxides,” vol. 52, no. 5, pp. 3143–3150, 1995.

[30] C. a. Gorski and M. M. Scherer, “Determination of nanoparticulate magnetite stoichiometry by Mossbauer spectroscopy, acidic dissolution, and powder X-ray diffraction: A critical review,” *Am. Mineral.*, vol. 95, no. 7, pp. 1017–1026, Jun. 2010.

[31] S. Staniland, B. Ward, A. Harrison, G. van der Laan, and N. Telling, “Rapid magnetosome formation shown by real-time x-ray magnetic circular dichroism.,” *Proc. Natl. Acad. Sci. U. S. A.*, vol. 104, no. 49, pp. 19524–8, Dec. 2007.

[32] M. I. Siponen, G. Adryanczyk, N. Ginet, P. Arnoux, and D. Pignol, “Magnetochrome: a c-type cytochrome domain specific to magnetotatic bacteria.,” *Biochem. Soc. Trans.*, vol. 40, no. 6, pp. 1319–23, Dec. 2012.

[33] J. Baumgartner, L. Bertinetti, M. Widdrat, A. M. Hirt, and D. Faivre, “Formation of magnetite nanoparticles at low temperature: from superparamagnetic to stable single domain particles,” *PLoS One*, vol. 8, no. 3, p. e57070, Jan. 2013.

[34] LeFort, “No Title,” *C.R. Acad. Sci. Paris*, vol. 34, p. 480, 1852.

[35] R. Massart, “Preparation of Aqueous Magnetic Liquids in Alkaline and Acidic Media,” *IEEE Trans. Magn.*, vol. Mag-17, no. 2, pp. 1247–1248, 1981.

[36] E. Zolotoyabko, *Basic Concepts of X-Ray Diffraction*. 2014.

[37] P. w. Atkins, *The Elements of Physical Chemistry*. 1992.

[38] B. D. Cullity and S. R. Stock, *Elements of X-Ray Diffraction*, Third. 2001.

[39] A. Fischer, M. Schmitz, B. Aichmayer, P. Fratzl, and D. Faivre, “Structural purity of magnetite nanoparticles in magnetotactic bacteria.,” *J. R. Soc. Interface*, vol. 8, no. 60, pp. 1011–8, Jul. 2011.

[40] A. L. Patterson, “The Scherrer Formula for X-Ray Particle Size Determination,” *Phys. Rev.*, vol. 56, pp. 978–982, 1939.

[41] J. I. Langford, “Scherrer after Sixty Years: A Survey and Some New Results in the Determination of Crystallite Size,” *J. Appl. Crystallogr.*, vol. 11, pp. 102–113, 1978.

[42] M. Schmitz, “High-Resolution Synchrotron X-ray Scattering reveals the Difference in the Ultrastructure of biogenic and Abiotic Magnetite Nanoparticles,” 2010.

[43] A. Hammersley, “Fit2D.” .

[44] C. Lee, “AutoFit.”

[45] “Standard Reference Material 1878a,” *Natl. Inst. Stand. Technol.*, no. September, pp. 1–4, 2005.

[46] E. Jäger and R. Perthel, *Magnetische Eigenschaften von Festkörpern*. 1996, p. 195.

[47] M. Widdrat, M. Kumari, É. Tompa, M. Pósfai, A. M. Hirt, and D. Faivre, “Keeping Nanoparticles Fully Functional: Long-Term Storage and Alteration of Magnetite,” *Chempluschem*, vol. 79, no. 8, pp. 1225–1233, Aug. 2014.

[48] D. Faivre, P. Agrinier, N. Menguy, P. Zuddas, K. Pachana, A. Gloter, J.-Y. Laval, and F. Guyot, “Mineralogical and isotopic properties of inorganic nanocrystalline magnetites,” *Geochim. Cosmochim. Acta*, vol. 68, no. 21, pp. 4395–4403, Nov. 2004.

[49] L. Vayssières, C. Chanéac, E. Tronc, and J. Jolivet, “Size Tailoring of Magnetite Particles Formed by Aqueous Precipitation: An Example of Thermodynamic Stability of Nanometric Oxide Particles.,” *J. Colloid Interface Sci.*, vol. 205, no. 2, pp. 205–212, Sep. 1998.

[50] I. Nyirő-Kósa, D. Csákberé Nyinagy, and M. Pósfai, “Size and shape control of precipitated magnetite nanoparticles,” *Eur. J. Mineral.*, vol. 21, no. 2, pp. 293–302, Mar. 2009.

[51] A.-H. Lu, E. L. Salabas, and F. Schüth, “Magnetic nanoparticles: synthesis, protection, functionalization, and application.,” *Angew. Chem. Int. Ed. Engl.*, vol. 46, no. 8, pp. 1222–44, Jan. 2007.

[52] Ö. Özdemir and D. J. Dunlop, “The Effect od Oxidation on the Verwey Transition in Magnetite,” *Geophys. Res. Lett.*, vol. 20, no. 16, pp. 1671–1674, 1993.

[53] A. P. Roberts, Y. Cui, and K. L. Verosub, “Wasp-waisted hysteresis loops: Mineral magnetic characteristics and discrimination of components in mixed magnetic systems,” *J. Geophys. Res.*, vol. 100, no. B9, pp. 17909–17924, 1995.

[54] V. K. Lamer, “Nucleation in Phase Transitions,” *Ind. Eng. Chem.*, vol. 44, no. 6, pp. 1270–1277, 1952.

[55] K. A. Jackson, *Kinetic Processes*. 2004, p. 409.

[56] K. J. Gallagher, W. Feitknecht, and U. Mannweiler, “Mechanism of Oxidation of Magnetite to γ-Fe2O3,” *Nature*, vol. 217, pp. 1118–1121, 1968.

[57] K. J. Gallagher and W. Feitknecht, “Mechanism for the Oxidation of Fe3O4,” *Nature*, vol. 228, pp. 548–549, 1970.

[58] U. Colombo, G. Fagherazzi, F. Gazzarrini, G. Lanzavecchia, and G. Sironi, “Mechanism of Low Temperature Oxidation of Magnetides,” *Nature*, pp. 1036–1037, 1968.

[59] R. Frison, G. Cernuto, A. Cervellino, O. Zaharko, G. M. Colonna, A. Guagliardi, and N. Masciocchi, “Magnetite–Maghemite Nanoparticles in the 5–15 nm Range: Correlating the Core–Shell Composition and the Surface Structure to the Magnetic Properties. A Total Scattering Study.,” *Chem. Mater.*, vol. 25, no. 23, pp. 4820–4827, Dec. 2013.

[60] B. D. Cullity and C. . D. Graham, *Introduction into Magnetic Materials*. 2008, p. 568.

[61] A. Rečnik, I. Nyirő-Kósa, I. Dódony, and M. Pósfai, “Growth defects and epitaxy in Fe3O4 and γ-Fe2O3 nanocrystals,” *CrystEngComm*, vol. 15, no. 37, pp. 7539–7549, 2013.

[62] M. I. Siponen, P. Legrand, M. Widdrat, S. R. Jones, W.-J. Zhang, M. C. Y. Chang, D. Faivre, P. Arnoux, and D. Pignol, “Structural insight into magnetochrome-mediated magnetite biomineralization.,” *Nature*, vol. 502, no. 7473, pp. 681–4, Oct. 2013.

[63] P. Arnoux, M. I. Siponen, C. T. Lefèvre, N. Ginet, and D. Pignol, “Structure and evolution of the magnetochrome domains: no longer alone,” *Front. Microbiol.*, vol. 5, no. March, pp. 1–7, Jan. 2014.

[64] D. Murat, A. Quinlan, H. Vali, and A. Komeili, “Comprehensive genetic dissection of the magnetosome gene island reveals the step-wise assembly of a prokaryotic organelle.,” *Proc. Natl. Acad. Sci. U. S. A.*, vol. 107, no. 12, pp. 5593–8, Mar. 2010.

[65] “Ph . D . ^{TM} Phage Display Libraries.”

[66] M. Alexe, M. Ziese, D. Hesse, P. Esquinazi, K. Yamauchi, T. Fukushima, S. Picozzi, and U. GÃ¶sele, “Ferroelectric Switching in Multiferroic Magnetite (Fe 3 O 4) Thin Films,” *Adv. Mater.*, vol. 21, no. 44, pp. 4452–4455, Nov. 2009.

[67] B. H. Lower, R. D. Lins, Z. Oestreicher, T. P. Straatsma, M. F. Hochella, L. Shi, and S. K. Lower, “In vitro evolution of a peptide with a hematite binding motif that may constitute a natural metal-oxide binding archetype.,” *Environ. Sci. Technol.*, vol. 42, no. 10, pp. 3821–7, May 2008.

[68] “Measuring Peptide Concentration.” [Online]. Available: http://www.thinkpeptides.com/peptidemeasuring.html.

[69] S. C. Gill and P. H. von Hippel, “Calculation of Protein Extinction Coefficients from Amino Acid Sequence Data,” *Anal. Biochem.*, 1989.

[70] J. Baumgartner, “Nucleation and Growth of Magnetite Nanoparticles under Biomimetic Conditions,” 2011.

Appendix

Activation Energy: Complete Dataset

Table A1: Qadruplicated measurements at 5 °C plus averaged size development and standard deviation.

5°C	M124	M166	M168	M169	Average		Standard deviation
Time (h)	**Mean particle diameter (nm)**						**(nm)**
1	18.4	21.0	21.0	20.8	20.3	±	1.3
2	20.9	26.6	26.5	25.1	24.8	±	2.7
3	23.0	29.9	30.6	27.0	27.6	±	3.5
4	24.9	33.0	33.8	28.6	30.1	±	4.1
5	26.6	35.6	35.6	30.2	32.0	±	4.4
6	28.9	37.2	36.8	31.8	33.7	±	4.0
7	30.9	38.4	37.7	33.5	35.1	±	3.6
8	33.2	39.4	38.3	35.3	36.6	±	2.8
n = 1							
MD_0	16.58	21.27	21.98	20.49	20.08	±	2.41
k	2.06	2.53	2.35	1.90	2.42	±	0.28
ln (k)	0.72	0.93	0.85	0.64	0.79	±	0.13
n = 2							
MD_0	14.94	18.58	19.50	19.13	18.04	±	2.1
k	103.87	167.83	157.52	110.12	134.84	±	32.52
ln (k)	4.64	5.12	5.05	4.70	4.88	±	0.24

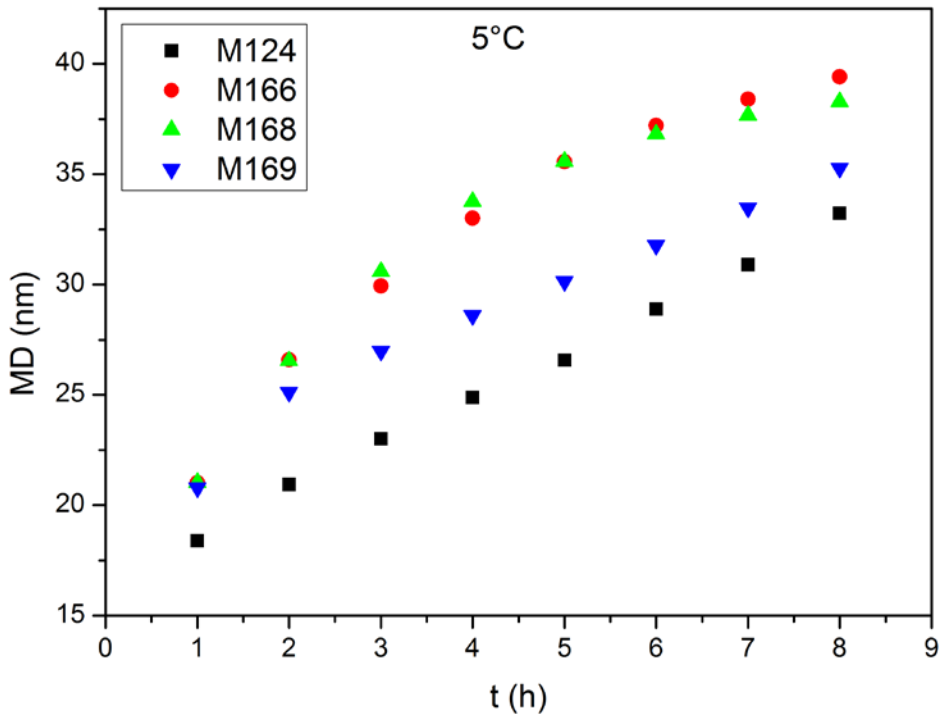

Figure A1: The evolution of mean particle dimension as a function of time at 5 °C.

Table A2: Qadruplicated measurements at 10 °C plus averaged size development and standard deviation.

10°C	M137	M141	M151	M153	Average	Standard deviation
Time (h)	**Mean particle diameter (nm)**					**(nm)**
1	22.3	21.8	21.8	22.9	22.2 ±	0.5
2	28.3	26.8	27.9	28.9	28.0 ±	0.9
3	32.3	31.0	32.4	34.0	32.4 ±	1.2
4	36.2	35.0	37.2	38.5	36.7 ±	1.5
5	39.4	38.7	40.2	41.9	40.1 ±	1.4
6	41.9	41.2	42.4	44.6	42.5 ±	1.5
7	43.6	43.0	43.9	46.2	44.2 ±	1.4
8	44.4	43.7	44.5	46.8	44.9 ±	1.3
n = 1						
MD_0	21.97	20.75	21.7	22.49	21.73 ±	0.73
k	3.13	3.2	3.24	3.44	3.25 ±	0.13
ln (k)	1.14	1.16	1.18	1.23	1.18 ±	0.04
n = 2						
MD_0	18.12	16.67	17.32	17.83	17.49 ±	0.64
k	227.51	224.88	238.92	264.26	238.89 ±	17.98
ln (k)	5.43	5.42	5.48	5.58	5.47 ±	0.07

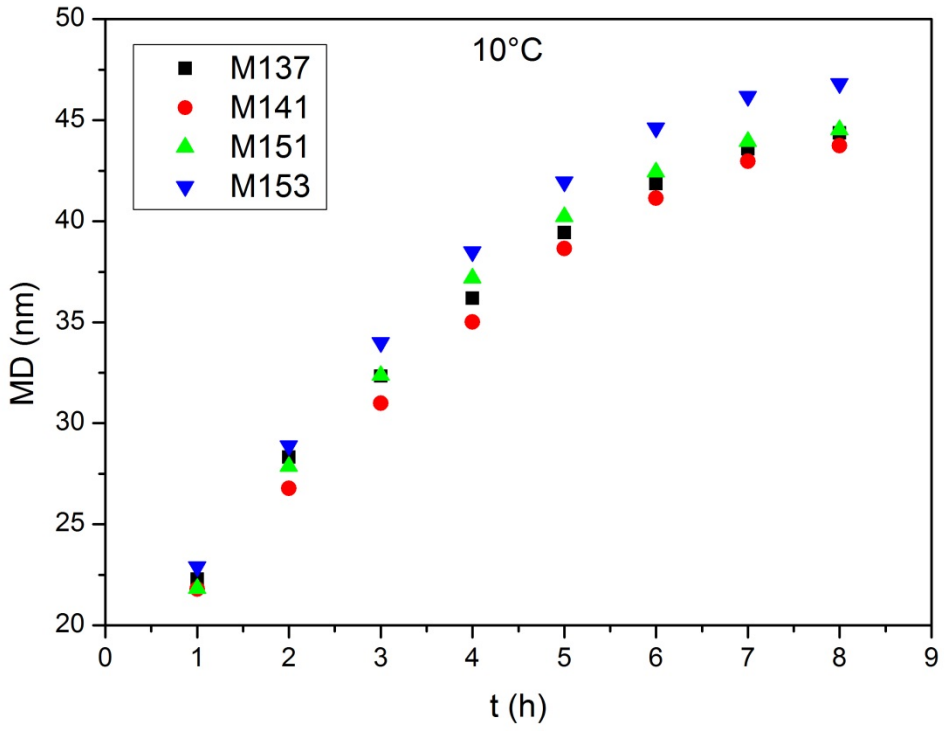

Figure A2: The evolution of mean particle dimension as a function of time at 10 °C.

Table A3: Qadruplicated measurements at 15 °C plus averaged size development and standard deviation.

15°C	M99	M125	M130	M131	Average	Standard deviation
Time (h)	**Mean particle diameter (nm)**					**(nm)**
1	21.5	20.7	22.6	23.7	22.1 ±	1.3
2	25.6	24.5	26.7	29.0	26.4 ±	1.9
3	28.9	28.7	30.6	34.1	30.6 ±	2.5
4	32.8	33.0	34.9	38.7	34.8 ±	2.7
5	36.3	37.3	39.1	43.2	39.0 ±	3.0
6	40.5	41.6	42.8	47.7	43.1 ±	3.2
7	44.2	46.2	46.0	51.4	47.0 ±	3.1
8	48.0	49.8	48.8	55.0	50.4 ±	3.1
n = 1						
MD_0	17.71	16.19	19.24	20.16	18.33 ±	1.75
k	3.78	4.23	3.82	4.48	4.08 ±	0.34
ln (k)	1.33	1.44	1.34	1.50	1.40 ±	0.08
n = 2						
MD_0	12.62	8.78	14.08	13.03	12.13 ±	2.31
k	248.57	278.94	267.68	347.08	285.57 ±	42.88
ln (k)	5.52	5.63	5.59	5.85	5.65 ±	0.14

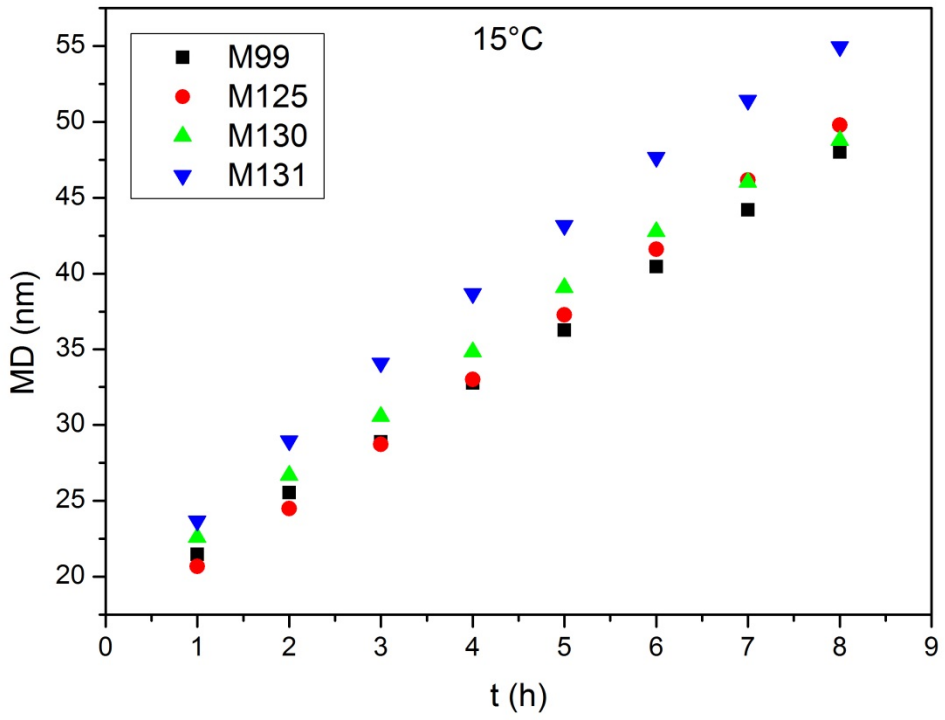

Figure A3: The evolution of mean particle dimension as a function of time at 15 °C.

Table A4: Qadruplicated measurements at 20 °C plus averaged size development and standard deviation.

20°C	M123	M133	M149	M163	Average		Standard deviation
Time (h)	**Mean particle diameter (nm)**						**(nm)**
1	22.9	21.9	21.7	22.8	23.1	±	2.2
2	28.5	27.4	28.1	27.5	28.6	±	2.2
3	32.3	32.7	33.2	31.6	33.2	±	2.4
4	36.4	37.6	38.4	35.2	37.6	±	2.8
5	41.1	42.8	42.0	39.2	41.8	±	3.1
6	44.9	46.9	45.7	43.2	45.8	±	3.5
7	49.0	50.9	48.4	47.6	49.4	±	3.5
8	51.8	54.5	52.8	51.2	52.9	±	3.7
n = 1							
MD_0	19.76	18.23	19.44	19.2	19.16	±	0.66
k	4.13	4.69	4.29	4.02	4.28	±	0.29
ln (k)	1.42	1.55	1.46	1.39	1.45	±	0.07
n = 2							
MD_0	13.74	8.96	11.97	13.7	12.09	±	2.25
k	304.86	351.55	323.99	285.9	316.58	±	28.03
ln (k)	5.72	5.86	5.78	5.66	5.75	±	0.09

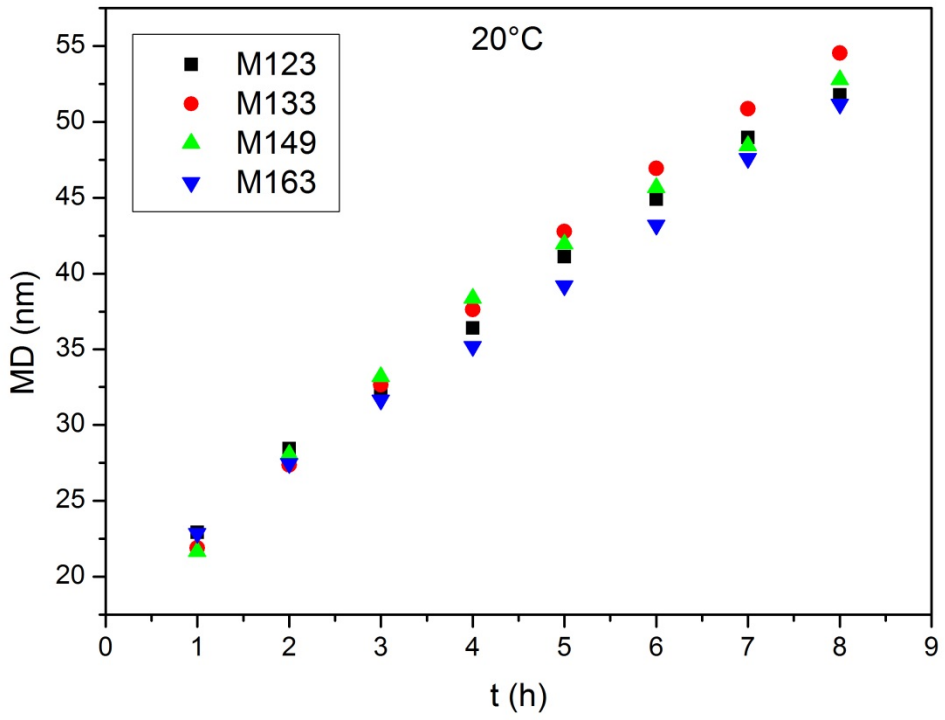

Figure A4: The evolution of mean particle dimension as a function of time at 20 °C.

Table A5: Qadruplicated measurements at 25 °C plus averaged size development and standard deviation.

25°C	M103	M121	M147	M148	Average	Standard deviation
Time (h)	**Mean particle diameter (nm)**					**(nm)**
1	23.0	20.5	24.0	24.5	23.0 ±	1.8
2	29.4	27.7	31.4	30.7	29.8 ±	1.6
3	33.9	33.9	38.0	35.8	35.4 ±	2.0
4	38.9	41.9	43.7	40.7	41.3 ±	2.0
5	45.0	46.5	48.5	45.1	46.3 ±	1.7
6	51.4	51.9	52.6	49.4	51.3 ±	1.4
7	57.5	57.8	56.9	53.5	56.4 ±	2.0
8	63.5	63.1	60.0	57.3	61.0 ±	2.9
n = 1						
MD_0	16.93	15.72	21.45	21.27	18.84 ±	2.95
k	5.75	6.04	5.1	4.63	5.38 ±	0.64
ln (k)	1.75	1.80	1.63	1.53	1.68 ±	0.12
n = 2						
MD_0	0	0	11.41	13.92	6.33 ±	7.38
k	447.87	464.85	439.72	376.27	432.18 ±	38.71
ln (k)	6.10	6.14	6.09	5.93	6.07 ±	0.09

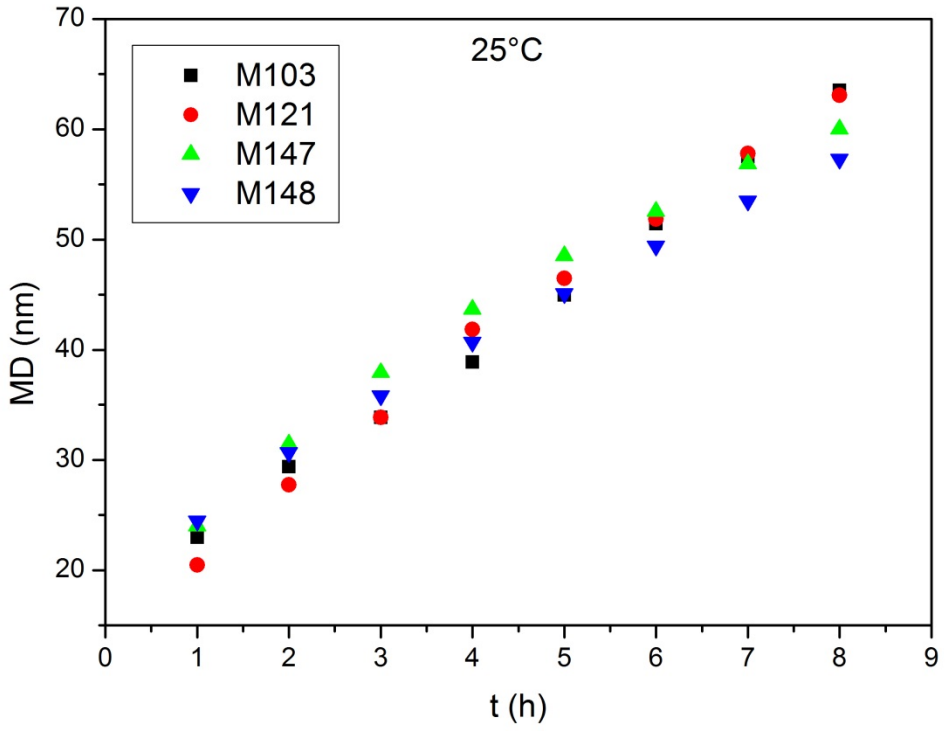

Figure A5: The evolution of mean particle dimension as a function of time at 25 °C.

Table A6: (left) The results of the linear, quadratic and cubic fit of $MD^n - MD_0^n = k * t$ for k and MD_0 for all temperatures. The adjusted R^2 confirm the best accordance for the quadratic fit. (right) the fit of the master curves with the adjusted R^2, which confirms the best accordance for the quadratic fit.

ϑ (°C)	n	k ($nm^n\ h^{-n}$)	MD_0 (nm)	R^2	fit of the master curve	R^2 (mastercurve)
5		2.42	18.51	0.97		
10		3.61	19.55	0.96		
15	1	4.11	18.11	1	$MD - MD_0 = kt + 0.01$	0.98
20		4.3	19.76	0.99		
25		5.45	18.61	1		
5		134.84	18.04	0.99		
10		238.89	17.49	0.99		
15	2	285.57	12.13	0.99	$MD^2 - MD_0^2 = kt - 3.75^2$	0.99
20		316.58	12.09	1		
25		432.18	6.33	0.99		
5		5938.54	13.65	1		
10		12280.84	-11.33	1		
15	3	13176.86	-15.05	0.96	$MD^3 - MD_0^3 = kt + 6.87^3$	0.95
20		16058	-17.56	0.97		
25		27985.13	-31.89	0.39		

Table A7: Initial values and results of fitting ln (k) over $1000*T^{-1}$ for the linear and the quadratic fit.

ϑ (°C)	$1000*T^{-1}$ (K^{-1})	n	ln (k)	A (h^{-1})	E_a (kJ mol^{-1})	R^2
5	3.5952		0.79 ± 0.13			
10	3.5317		1.18 ± 0.04			
15	3.4704	1	1.40 ± 0.08	$8{,}5 \times 10^4$	24 ± 4	0.88
20	3.4112		1.45 ± 0.07			
25	3.3540		1.68 ± 0.12			
5	3.5952		4.88 ± 0.24			
10	3.5317		5.47 ± 0.07			
15	3.4704	2	5.65 ± 0.14	1.3×10^7	28.4 ± 5	0.88
20	3.4112		5.75 ± 0.09			
25	3.3540		6.07 ± 0.09			

Alteration: Complete Dataset

Table A8: A summary of all TEM results (initial and final state) shows that all samples contain mainly magnetite/maghemite and that there is no indication of other phases in the bulk phase. Oxidation is indicated by superstructure reflections (maghmite) and feroxyhyte surface layers occur at the final state.

Sample	Age (days)	TEM type	Results
121	57	Jeol 2000FX	two types of particles, all aggregated: (a) few nm-sized magnetite, (b) euhedral, octahedral magnetite with sizes ranging from a few tens to several hundred nm
123	54	Jeol 2000FX	very thick aggregates of magnetite particles, individual crystal sizes difficult to see, probably between 10 and 100 nm
124	54	Jeol 2000FX	uniformly distributed aggregates of magnetite, few tens of nm particles that seem to be aggregates of nm-sized crystals
125	38	Philips CM20	compact aggregates of pure magnetite as in 124A, particle sizes not determinable because of thickness
121 123 124 125	724 727 727 728	Zeiss 912 Omega	two types of magnetite/maghemite structures (a) highly aggregated small particles in the range of a few nm and (b) big sphere-like structures of sizes between 100 and 300 nm, sometimes also aggregates of spheres
121 123 124 125	756 759 759 760	JEOL 3010	particle sizes and shapes appear to be the same as in the fresh samples but magnetite (at least in some observed grains) oxidized to maghemite, as evidenced by superstructure reflections in SAED patterns and superstructure periodicities in HRTEM images

Table A9: Collection of all data calculated from the XRD data for the samples 121 and 123. Evolution of the lattice parameter *a* and the corrected full width of half maximum $fwhm_{corr}$.

Sample	Age (days)	a (nm)	$fwhm_{corr}$ (nm^{-1})	Sample	Age (days)	a (nm)	$fwhm_{corr}$ (nm^{-1})
121	8	0.8394	0.0997	**123**	5	0.8399	0.1215
-20 °C	93	0.8395	0.1041	-20 °C	90	0.8396	0.1253
	179	0.8392	0.1070		176	0.8395	0.1253
	315	0.8392	0.1169		312	0.8395	0.1329
	424	0.8390	0.1161		421	0.8395	0.1339
	546	0.8389	0.1158		543	0.8395	0.1333
4 °C	93	0.8391	0.1043	4 °C	90	0.8394	0.1241
	179	0.8391	0.1091		176	0.8392	0.1260
	315	0.8388	0.1200		312	0.8391	0.1364
	424	0.8385	0.1208		421	0.8388	0.1357
	546	0.8385	0.1208		543	0.8388	0.1377
a.t.	93	0.8388	0.1081	a.t.	90	0.839	0.1279
	179	0.8386	0.1133		176	0.8386	0.1295
	315	0.8384	0.1255		312	0.8386	0.1390
	424	0.8382	0.1219		421	0.8385	0.1381
	546	0.8379	0.1221		543	0.8379	0.1389
a.t. + Ar	93	0.8389	0.1096	a.t. + Ar	90	0.8389	0.1285
	179	0.8386	0.1138		176	0.8387	0.1300
	315	0.8383	0.1258		312	0.8385	0.1371
	424	0.8381	0.1230		421	0.8382	0.1385
	546	0.8379	0.1228		543	0.8380	0.1377

Table A10: Collection of all data calculated from the XRD data for the samples 124 and 125. Evolution of the lattice parameter *a* and the corrected full width of half maximum $fwhm_{corr}$.

Sample	Age (days)	a (nm)	$fwhm_{corr}$ (nm^{-1})	Sample	Age (days)	a (nm)	$fwhm_{corr}$ (nm^{-1})
124	5	0.8388	0.1892	**125**	4	0.8397	0.1262
-20 °C	90	0.8387	0.1902	-20 °C	89	0.8398	0.1273
	176	0.8382	0.1934		175	0.8395	0.1295
	312	0.8383	0.2009		311	0.8395	0.1368
	421	0.8383	0.1969		420	0.8394	0.1369
	543	0.8380	0.1986		542	0.8392	0.1363
4 °C	90	0.8380	0.1925	4 °C	89	0.8394	0.1282
	176	0.8376	0.1919		175	0.8391	0.1317
	312	0.8374	0.1998		311	0.8388	0.1433
	421	0.8372	0.1966		420	0.8387	0.1374
	543	0.8371	0.1914		542	0.8383	0.1431
a.t.	90	0.8373	0.1910	a.t.	89	0.8389	0.1319
	176	0.8370	0.1909		175	0.8386	0.1346
	312	0.8368	0.1932		311	0.8382	0.1411
	421	0.8366	0.1918		420	0.8379	0.1427
	543	0.8363	0.1963		542	0.8378	0.1416
a.t. + Ar	90	0.8373	0.1922	a.t. + Ar	89	0.8389	0.1339
	176	0.8369	0.1912		175	0.8385	0.1351
	312	0.8367	0.1948		311	0.8383	0.1422
	421	0.8366	0.1941		420	0.8379	0.1415
	543	0.8363	0.1964		542	0.8378	0.1416

Table A11: Change in the lattice parameter *a*, oxidation state *z*, and particle core d_{core} and shell thickness d_{layer} for different storage conditions as a function of alteration time for sample 121.

Sample	age (days)	a (nm)	z	d_{total} (nm)	d_{core} (nm)	d_{layer} (nm)
121	8	0.8394	0.0575	63.00	61.77	0.62
-20 °C	93	0.8395	0.0384		62.19	0.41
	179	0.8392	0.0827		61.22	0.89
	315	0.8392	0.0913		61.03	0.99
	424	0.8390	0.1177		60.43	1.29
	546	0.8389	0.1485		59.72	1.64
4 °C	93	0.8391	0.1042		60.74	1.13
	179	0.8391	0.1091		60.62	1.19
	315	0.8388	0.1594		59.46	1.77
	424	0.8385	0.2155		58.11	2.45
	546	0.8385	0.2089		58.27	2.37
a.t.	93	0.8388	0.1564		59.53	1.74
	179	0.8386	0.2042		58.38	2.31
	315	0.8384	0.2312		57.72	2.64
	424	0.8382	0.2656		56.84	3.08
	546	0.8379	0.3250		55.27	3.87
a.t. + Ar	93	0.8389	0.1447		59.81	1.60
	179	0.8386	0.1926		58.67	2.17
	315	0.8383	0.2613		56.96	3.02
	424	0.8381	0.2817		56.43	3.29
	546	0.8379	0.3189		55.43	3.79

Table A12: Changes in the lattice parameter *a*, oxidation state *z*, and particle core d_{core} and shell thickness d_{layer} for different storage conditions and times for Sample 123. At the age of 5 days the oxidation parameter is negative. This is an artificial effect due to the way z is calculated and does not mean that the material was reduced.

Sample	Age (days)	a (nm)	z	d_{total} (nm)	d_{core} (nm)	d_{layer} (nm)
123	5	0.8399	-0.0428	51.73	52.46	-0.36
-20 °C	90	0.8396	0.0193		51.40	0.17
	176	0.8395	0.0415		51.01	0.36
	312	0.8395	0.0301		51.21	0.26
	421	0.8395	0.0275		51.25	0.24
	543	0.8395	0.0346		51.13	0.30
4 °C	90	0.8394	0.0581		50.71	0.51
	176	0.8392	0.0814		50.29	0.72
	312	0.8391	0.1097		49.77	0.98
	421	0.8388	0.1560		48.89	1.42
	543	0.8388	0.1610		48.79	1.47
a.t.	90	0.8390	0.1240		49.50	1.12
	176	0.8386	0.1895		48.23	1.75
	312	0.8386	0.2067		47.89	1.92
	421	0.8385	0.2159		47.70	2.01
	543	0.8379	0.3290		45.29	3.22
a.t. + Ar	90	0.8389	0.1480		49.04	1.34
	176	0.8387	0.1797		48.43	1.65
	312	0.8385	0.2165		47.69	2.02
	421	0.8382	0.2668		46.65	2.54
	543	0.8380	0.3058		45.81	2.96

Table A13: Changes in the lattice parameter *a*, oxidation state *z*, and particle core d_{core} and shell thickness d_{layer} for different storage conditions and times for Sample 124.

Sample	Age (days)	a (nm)	z	d_{total} (nm)	d_{core} (nm)	d_{layer} (nm)
124	5	0.8388	0.1564	33.21	31.38	0.92
-20 °C	90	0.8387	0.1779		31.11	1.05
	176	0.8382	0.2656		29.96	1.62
	312	0.8383	0.2558		30.10	1.56
	421	0.8383	0.2572		30.08	1.57
	543	0.8380	0.3022		29.46	1.88
4 °C	90	0.8380	0.3011		29.47	1.87
	176	0.8376	0.3722		28.44	2.39
	312	0.8374	0.4156		27.77	2.72
	421	0.8372	0.4446		27.30	2.96
	543	0.8371	0.4738		26.81	3.20
a.t.	90	0.8373	0.4315		27.51	2.85
	176	0.8370	0.4957		26.43	3.39
	312	0.8368	0.5318		25.79	3.71
	421	0.8366	0.5558		25.34	3.94
	543	0.8363	0.6187		24.08	4.56
a.t. + Ar	90	0.8373	0.4368		27.43	2.89
	176	0.8369	0.5080		26.22	3.50
	312	0.8367	0.5519		25.41	3.90
	421	0.8366	0.5688		25.09	4.06
	543	0.8363	0.6197		24.06	4.57

Table A14: Changes in the lattice parameter *a*, oxidation state *z*, and particle core d_{core} and shell thickness d_{layer} for different storage conditions and times for Sample 125. At the age of 4 days the oxidation parameter is negative. This is an artificial effect due to the way z is calculated and does not mean that the material was reduced.

Sample	Age (days)	a (nm)	z	d_{total} (nm)	d_{core} (nm)	d_{layer} (nm)
125	4	0.8397	-0.0046	49.79	49.87	-0.04
-20 °C	89	0.8398	-0.0110		49.97	-0.09
	175	0.8395	0.0292		49.30	0.24
	311	0.8395	0.0384		49.15	0.32
	420	0.8394	0.0616		48.75	0.52
	542	0.8392	0.0913		48.23	0.78
4 °C	89	0.8394	0.0519		48.91	0.44
	175	0.8391	0.1091		47.91	0.94
	311	0.8388	0.1594		46.99	1.40
	420	0.8387	0.1873		46.47	1.66
	542	0.8383	0.2538		45.16	2.31
a.t.	89	0.8389	0.1474		47.21	1.29
	175	0.8386	0.1963		46.29	1.75
	311	0.8382	0.2723		44.79	2.50
	420	0.8379	0.3177		43.84	2.98
	542	0.8378	0.3463		43.21	3.29
a.t. + Ar	89	0.8389	0.1472		47.22	1.29
	175	0.8385	0.2159		45.91	1.94
	311	0.8383	0.2594		45.05	2.37
	420	0.8379	0.3193		43.80	3.00
	542	0.8378	0.3422		43.30	3.24

List of Abbreviations

A	Pre-factor
	Ampere
A, Ala	Alanine
a, c	Lattice parameter of a unit cell
a.t.	Ambient temperature
Ar	Argon
BESSY	Berliner Elektronenspeicherring-Gesellschaft für Synchrotronstrahlung
c	concentration
C, Cys	Cysteine
Cl	Clorine
cryo-TEM	Cryogenic transmission electron microscopy
d	Diameter
D, Asp	Aspartic acid
d_{hkl}	distance between the single layers of the lattice plane hkl
ΔmamP	Deletion mutant of gene *mamP*
e	Euler's number
E, Glu	Glutamic acid
E_a	Activation energy or activation barrier
exp	experimental
F, Phe	Phenylalanine
Fe	Iron
fwhm	Full width at half maximum
g	Gramm
glycine-HCl	Glycine hydrochloride
H	Magnetic field
	Hydrogen
h	Hours
H, His	Histidine
H_C	Coercivity
H_{CR}	Coercivity of the remanence

hkl	Miller indices of the lattice plane or designation of the lattice plane itself
HRTEM	High-resolution transmission electron microscopy
I	Intensity
I, Ile	Isoleucine
instr	instrumental
IRM	Isothermal remanent magnetization
k	Growth rate constant
K	Shape factor, Scherrer equation
k_B	Boltzmann constant
$\boldsymbol{k_f}$, $\boldsymbol{k_i}$	wave vector of the incoming and the scattered beam, respectively
kg	Kilogram
kJ	Kilojoule
L	Liter
L, Leu	Leucine
L, Lys	Lysine
LSW	Lifshitz, Slyozov, Wagner
λ	wavelength
m	Meter
M	Molar concentration, Molar mass
	Magnetization
M, Met	Methionine
Mam	Class of proteins referring to magnetosome membrane
mbar	millibar
MD	Multidomain
min	Minute
mL	Milliliter
MRI	Magnetic resonance imaging
M_{RS}	Magnetization remanence
M_S	Saturation magnetization
mT	Millitesla
MTB	Magnetotactic bacteria

µL	Microliter
n	Number
N, Asn	Asparagine
N_2	Nitrogen
N_A	Avogadro constant
Na	Sodium
nm	Nanometer
O	Oxygen
P, Pro	Proline
pfu	Plague forming units (unit for the concentration of phages)
pI	Isoelectric point
PP	Primary particles
q	Scattering vector
Q, Gln	Glutamine
R	Gas constant
	Radius of a spherical particle
r	Radius
R, Arg	Arginine
R_0	Radius of a spherical particle at t = 0
R^2	Adjusted R-square
S, Ser	Serine
SAD	Selectred area diffraction
SP	Superparamagnetic
Sr	Strontium
SSD	Stable single domain
T	Temperature in Kelvin
t	Time
T, Thr	Threonine
TBS	Tris buffered saline
TEM	Transmission electron microscopy
Ti	Titanium
Tris-HCl	Tris(hydroxymethol)aminoethane hydrochloride

ϑ	Temperature in degree Celcius
V, Val	Valine
W, Trp	Tryptophan
Xm	Magnetic susceptibility
XMCD	X-ray magnetic circular dichroism
XRD	X-ray diffraction
Y, Tyr	Tyrosine
z	oxidation parameter

List of Publications

Papers as first author

M. Widdrat et al., “Activation Energy of Magnetite Crystal Growth from Primary Particles.” *manuscript in preparation*

M. Widdrat et al., “Keeping Nanoparticles Fully Functional: Long-Term Storage and Alteration of Magnetite,” *Chempluschem*, vol. 79, no. 8, pp. 1225–1233, Aug. 2014.

Papers as co-author

A. Kraupner et al., “What works best: Biological vs. synthetic magnetite and small vs. large nanoparticels as contrast agent for MRI.” *manuscript in preparation*

M. Kumari et al., “Distinguishing magnetic particle size of iron oxide nanoparticles with first-order reversal curves,” *J. Appl. Phys.*, vol. 116, no. 12, Sep. 2014.

A. Körnig et al., “Probing the mechanical properties of magnetosome chains in living magnetotactic bacteria.,” *Nano Lett.*, vol. 14, no. 8, pp. 4653–4659, Aug. 2014.

P. J. Vach et al., “Selecting for function: solution synthesis of magnetic nanopropellers.,” *Nano Lett.*, vol. 13, no. 11, pp. 5373–5378, Nov. 2013.

M. I. Siponen et al., “Structural insight into magnetochrome-mediated magnetite biomineralization,” *Nature*, vol. 502, no. 7473, pp. 681–684, Oct. 2013.

J. Baumgartner et al., “Magnetotactic bacteria form magnetite from a phosphate-rich ferric hydroxide via nanometric ferric (oxyhydr)oxide intermediates.,” *Proc. Natl. Acad. Sci. U.S.A.*, vol. 110, no. 37, pp. 14883–14888, Sep. 2013.

J. Baumgartner et al.Faivre, “Formation of magnetite nanoparticles at low temperature: from superparamagnetic to stable single domain particles,” *PLoS One*, vol. 8, no. 3, p. e57070, Jan. 2013.

J. Baumgartner et al., “From magnetotactic bacteria to hollow spirilla-shaped silica containing a magnetic chain,” *RSC Adv.*, vol. 2, no. 21, pp. 8007–8009, 2012.

Eigenständigkeitserklärung

Hiermit versichere ich, Marc Widdrat, dass ich die vorliegende Arbeit zu dem Thema "Formation and Alteration of Magnetite Nanoparticles" selbständig und unter ausschließlicher Verwendung der angegebenen Literatur und Hilfsmittel erstellt habe.

Die Arbeit wurde bisher in gleicher oder ähnlicher Form keiner anderen Prüfungsbehörde vorgelegt und auch nicht veröffentlicht.

Potsdam, den 30.09.2014

Marc Widdrat